Analysis of particles produced in $Au + Au$ collisions at $\sqrt{s_{NN}} = 200$ GeV

David Sandberg
Niels Bohr Institute
University of Copenhagen

February 27, 2003

Thesis presented for the Cand. Scient. degree (Master of Science).
Supervisor: Jens Jørgen Gaardhøje

Preface

I was first introduced to the High Energy Heavy Ion group at the Niels Bohr Institute in the spring 1999 through my bachelor thesis. That thesis concerned the testing of a Time Projection Chamber later used in the BRAHMS experiment.

Since then I have become more and more involved with the group and also spent some time at the experimental sight at Brookhaven National Laboratories. Here I got my first "hands on" feeling for the experiment and I feel that this has been a great help for my global understanding of the project. During my stay in Brookhaven I also got to meet and work with other people from the Collaboration.

My special thanks goes out to the people of the High Energy Heavy Ion group at the Niels Bohr Institute, whom without help this thesis would not be in your hands right now. I also want to thank my father Arne Sandberg for his support through difficult times and Erik Jakobsen, Mattias Matsson and Ulf Hansson for letting me crash at their places when in accomodation problems.

Copenhagen, March 2002

David Sandberg

Contents

Chapter 1

Introduction

The major goal for High Energy Heavy Ion physics is to understand the properties of matter under extreme conditions (heat and pressure). To achieve this goal we have to create an environment where such conditions are present.

New theories developed in Relativistic Heavy Ion physics about the properties of hot and dense matter has led to new experimental challenges in the same field. It is believed that when matter is extremely hot ($T > 10^{12}$ K) and dense ($\rho > 10^{15}$ g/cm^3), a phase transition between a hadron gas and Quark Gluon Plasma (QGP) occurs. It is believed that the early universe was in this state [1]. Due to these new ideas the Relativistic Heavy Ion Collider (RHIC) in Brookhaven was build.

RHIC collides gold-gold nuclei at center of mass energies of 200 GeV and has been doing this during summer and autumn 2002. RHIC has four different experiments running, of which BRAHMS is the one to be referred to in this thesis.

When the gold-gold nuclei collide a hot and dense zone is created. This zone expands and cools off. While doing so it radiates particles, which are spread out with a certain momentum distribution. In the spectrometers these particles are detected and their momentum is measured. From the momentum distributions particle spectra are developed. This thesis will provide a description of how the spectra in BRAHMS are deduced. Different models have been developed to interpret these spectra. The thesis will focus mainly on two of these models, the thermal Boltzmann model and the hydrodynamical Blast Wave model. The thermal Boltzmann model is an idea based on the assumption that thermal equilibrium in the collision zone is reached before the particles radiates out. The blast wave model is based on features of the very high pressure reached in the collision zone. The model is purely hydrodynamical and the foundation is the idea of a collective flow during the expansion of the collision zone.

When fitting particle distributions a common feature is to fit them with an exponential function. This function is based on the idea of a thermal distribution and the fact that the spectra have an exponential shape. The function it self is not thermally correct. An investigation will be conducted of how fit results from this function and the two models differ. Both the two models and the exponential fit functions calculate the number of particles in a small rapidity region and temperature, explained in chapter 4. Once the number of particles and the temperature is found the two physical variables can be used to identify probes of the QGP signatures, described in chapter 2.

Chapter 2

Heavy Ion Collisions at Ultra Relativistic Energies

Studies of the background radiation in the universe shows that the universe is expanding. If one assumes that the universe has evolved adiabatically and in equilibrium it is possible to extrapolate back in time to the very early universe, 10^{-43} second after the big bang [1]. At this early stage quarks and gluons were deconfined in a quark-gluon plasma (QGP). Due to the continuous expansion of the universe the energy density decreased and a “freeze out” occurred 10^{-5} seconds after the big bang. Then the quarks and gluons where confined into hadrons. This is today the normal state of these particles through out the universe, as far as we know.

The current goal of heavy ion physics is to, in the laboratory, recreate the QGP state and study the details of the phase transition between QGP and the hadron gas state. By doing this we can get a better understanding of the fundamental issues of chiral symmetry breaking, color confinement and asymptotic freedom. The solution to these questions move us closer to the understanding of matter and its building blocks and thereby toward an understanding of our whole existence.

An important step toward this goal is to understand the collision mechanism and its dynamical evolution.

2.1 The Phase Transition and QGP

The phase transition between asymptotically free quarks and gluons to confined hadronic states depends on temperature and particle density. The correlation between the two is shown in figure 2.1. The curves and region in figure 2.1 are in principle calculable with Quantum Chromo Dynamics (QCD), the theory of the strong interaction.

2.1.1 Quantum Chromo Dynamics (QCD)

Quantum Chromo Dynamics (QCD) is the theory describing strong interactions between particles. The strong interaction has a very short range (1 fm). Therefore it is only active between neighboring (close) nucleons inside the nucleus and between quarks and gluons inside the nucleons.

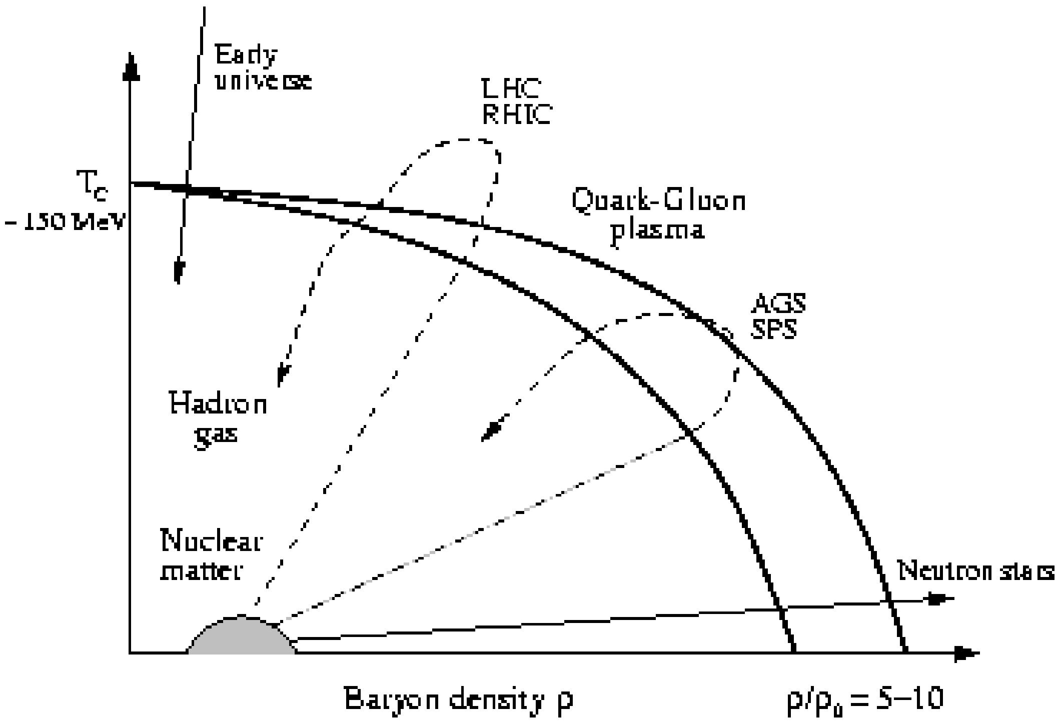

Figure 2.1: The phase diagram for phase transition between QGP and a hadron gas. The arrows shows different ways to enter and exit the two phases. Notice the hot early universe path and the cold, but dense neutron star path. Between the two boundary lines there is a mixed phase.

There is a great difference between the fields and forces inside and outside the nucleus. Outside the nucleus it is the electrical fields and forces together with gravity that describe the world. The behavior of the electrical fields and forces is well described by Quantum Electro Dynamics (QED). In QED the field is due to the photons. The photons neither interact with each other nor carry charge. In QCD we have a color field containing three different charges red, green and blue mediating the interaction between quarks. It is important to point out that in QCD the hadrons are color neutral, as it appears to be the case in nature. Color neutral means that the colors cancel out in combinations (rgb), $\bar{r}\bar{g}\bar{b}$, or color-anticolor. Since color neutrality is a requirement, a hadron must consist of either three quarks or antiquarks qqq or $\bar{q}\bar{q}\bar{q}$ (baryons) or one quark and one antiquark $q\bar{q}$ (mesons).

The color field inside the nucleus is mediated by the gluons. The gluons carry color and interact with each other. Since they carry color charge themselves, a quark that emits a gluon must change color itself. Suddenly the situation has becom a lot more complicated. The fact that the gluons carry color charge and that color neutrality is needed, force the quarks to be close together (less than 1 fm). Here they have the lowest potential energy see figure 2.2.

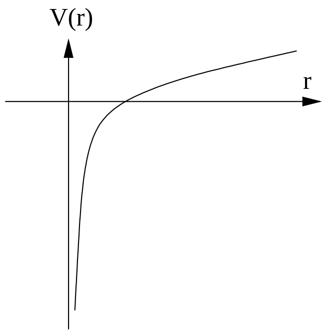

Figure 2.2: The potential between quarks vs distance. Notice the linearity in the potential when distance between the quarks becomes large enough.

The linear part of figure 2.2, where the quark potential $V(r)$ becomes positive, is due to the gluon-gluon interaction. Since the gluons interact with quarks and among themselves there is a constant energy density within neighboring quarks. This means that the total energy increases when the distance between the quarks increase, since the volume between them increases. To avoid a too large energy increase the field between the quarks is squeezed into a thin string. If the distance becomes large enough, there will be enough potential energy to create a new $q\bar{q}$ pair. It takes less energy to create two new quarks than to move the two originating quarks further away from each other. The result is that you get two quark pairs instead of two quarks split up. Therefore there are no existing free quarks. This is known as confinement.

2.1.2 QGP and the Hadron Gas.

We have talked about a phase transition between a dense hadron gas and a Quark Gluon Plasma. Being in the state of a hadron gas all quarks are confined into baryons and mesons (previous section). If now the pressure is increased on the nucleons and they are squeezed together the color fields of the quarks inside the nucleons will get mixed up. A *color screening* appears, where quarks from different hadrons will interact. We are now in the small radius part of figure 2.2, where the quark potential is negative. Here there is little energy loss moving around, since the quarks always are in a close distance to each other. The quarks in this state will be in a medium where the colors will be completely mixed. At small distances the interaction is small. The quarks are no longer confined in a certain hadron. This is the so called *asymptotic freedom*. Asymptotic since they only are allowed to move freely inside the medium. Also see figure 2.3.

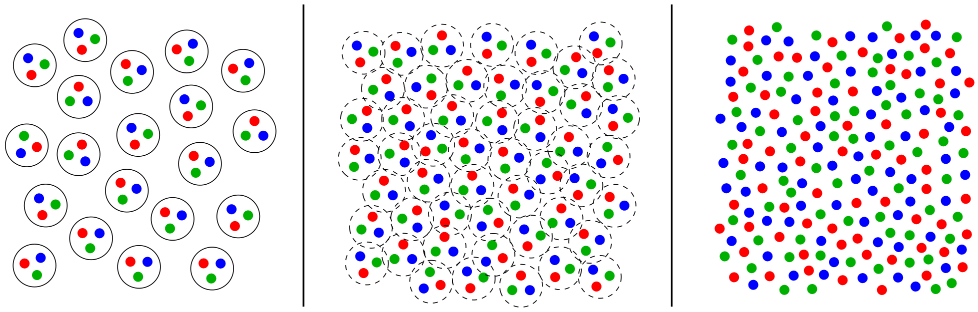

Figure 2.3: Left: Beginning quarks confined in hadrons. Middle: The pressure and energy is increased to create color screening. The phase transition is on the way. Right: Finally for sufficient energies and density the confined quarks undergo a phase transition and become asymptotically free quarks.

To calculate the critical temperature ($T_c \approx 140$ MeV [2]) for low densities and the critical density $\rho/\rho_0 = 5 - 10$ for low temperatures one has to use lattice QCD. Lattice QCD is the subfield of particle theory which attempts to solve QCD problems by approximating space-time with a discrete numerical grid. Once they are put on a grid, these problems can be approached by a variety of means, most often involving comlpex numerical methods on super-computers [3].

2.2 Nuclear Collision Properties.

The RHIC center of mass energy is $\sqrt{s_{NN}} = 200$ GeV. At this energy the nuclei are completely relativistic and Lorentz contracted from the laboratory system point of view. The nucleons are divided into two categories, participants and spectators, depending on their role in the collision. The spectators are the nucleons not participating in the collision and naturally the participants the nucleons participating in the collision (figure 2.4). At these energies, the idea is that only the overlapping nucleons participate.

The impact parameter b is a measure of how central the collision is. b is defined as the transverse distance between the center of mass of the nuclei in the collision point (figure 2.4). Experimentally, the impact parameter is not determined. Instead one measures the *multiplicity*, which is the number of particles radiated out of the collision zone. The more radiated particles the more central the collision assuming a monotonic relationship, between the number of produced particles and the number of participants. The impact parameter is measured in percentage (figure 2.5).

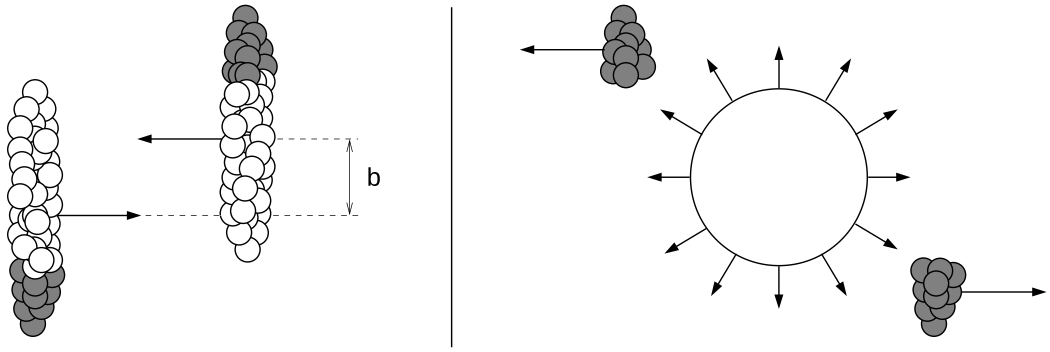

Figure 2.4: Participants vs spectators. The nuclei are completely Lorentz contracted and look like two pancakes. Furthermore the number of participants are completely dependent on the impact parameter b.

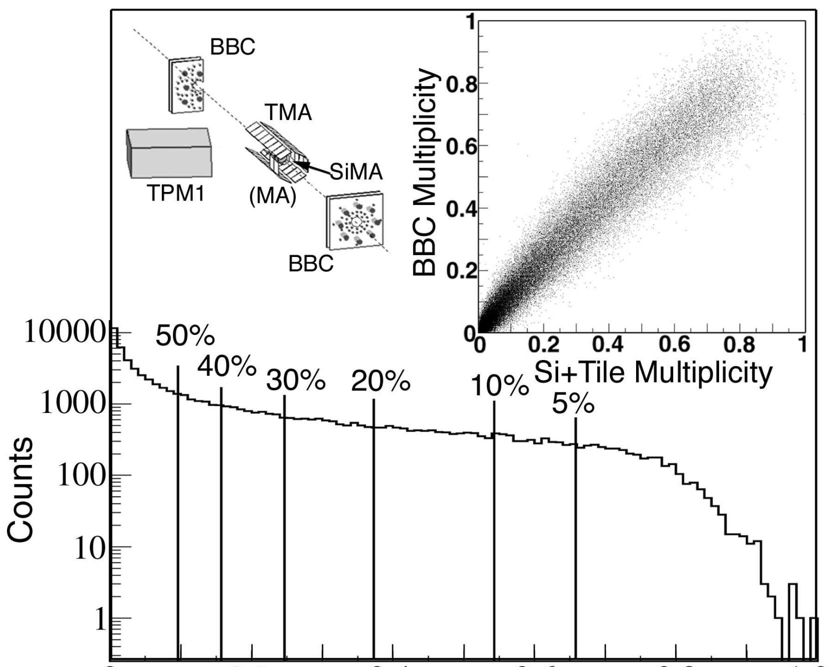

Figure 2.5: Centrality measurement at BRAHMS [4]. The centrality measured by multiplicity arrays. Right upper corner. The multiplicity measured by the beam-beam counters versus the multiplicity arrays. Also see chapter 3.

2.2.1 Collision Theories

There exist two major theories of how the collision evolves in relativistic heavy ion physics. They are both dependent on the amount of kinetic energy brought into the collision (beam energy). For lower energies ($\sqrt{s_{NN}} \approx 5 - 10$ GeV) nuclear stopping is dominant (figure 2.6) and for the very high energies presented here ($\sqrt{s_{NN}} \approx 200$ GeV) the transparent model is more appropriate figure 2.7.

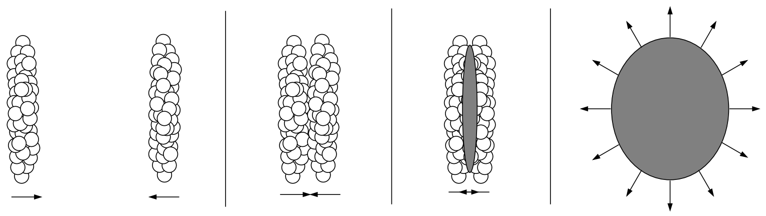

Figure 2.6: Nuclear stopping. The participants come to a complete stop and stay inside the fireball. Their rapidity is changed from beam rapidity to mid-rapidity ($y = 0$).

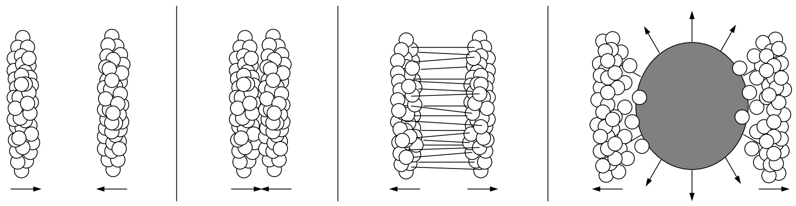

Figure 2.7: Nuclear transparency. In this scenario the participants are transparent and continue with high rapidity. As proposed by Bjorken and explained in the text. The participant rapidity may be shifted from the beam rapidity, but does not go all the way down to mid-rapidity. A fireball is created

Stopping is defined as shift in rapidity between beam rapidity and average rapidity of the net-baryons after collision $\delta y = y_{beam} - \langle y_b \rangle$. The net-baryon rapidity is calculated as

$$\langle y_b \rangle = \int_{y_m}^{y_{beam}} (y - y_m) \frac{dN}{dy} dy + y_m, \tag{2.1}$$

where y_m is midrapidity and $\frac{dN}{dy}$ is the net-baryon rapidity density. In the stopping model the kinetic energy of the participants is completely transfered to the fireball. There are several ways of measuring the degree of stopping. They all fit together.

- The ratio between anti-protons and protons $N(\bar{p})/N(p)$. Since the baryon-number is conserved in the collision, the ratio of produced particle/anti-particle is one. By looking at the ratio $N(\bar{p})/N(p)$ one can see how many primary protons have been stopped, and thereby find the stopping.
- The net-baryon density in the mid-rapidity region. Primary baryons that are stopped should be in this region.
- The average shift in rapidity for the primary nucleons.

At lower beam energies there are more primary protons left in the fireball than for higher energies. At AGS energies the net-proton ratio at midrapidity is much higher than RHIC. At RHIC the primary protons become transparent. By comparison between the different beam energies, transparency increases for higher energies, figure 2.9.

The major feature for transparency is the *formation time*, the time for new particles to be created (1 fm/c), since $\Delta E \Delta t < \hbar$. For sufficiently high energies relativistic effects come into play. The colliding nuclei have passed each other and are outside the formation zone when new particles are created. It will be shown in chapter 6 that a plateau of particle production as function of rapidity is present here. This is an assumption made in [6]. Inside the collision zone the entropy per rapidity is conserved. The particle production per unit rapidity is not dependent on the evolution of hydrodynamics, but only on the initial energy deported in the early stage of the collision. Once the two nuclei are further apart than their diameter the fireball will undergo an expansion and cool down.

Space Time Evolution of the Collision

Figure 2.8 shows a proposed illustration of what happens inside the hot and dense zone. It begins with the collision and continues from there into the phase where the particles are created. The formation time is 1fm/c. This is a color dense region. As the hot and dense zone expands (figure 2.8) the temperature decreases, due to energy conservation. After a few fm/c the critical temperature T_c is reached and the quarks and gluons hadronize. Hadrons are created and we have a mixed phase of a hadron gas and QGP inside the hot and dense zone. In this phase the interaction rate is very high. The hot and dense zone is expanding and cooling down. More and more hadrons are created. This state will be preserved until the mean free path between the hadrons is so big that they stop interacting with each other and become stabilized, 10fm/c. Finally there are only hadrons left in the hot and dense zone. We call this the (*freeze out time*). From then on the hadrons stream out of the hot and dense area unaffected and we can detect them in experiments.

2.3 On the Lookout for QGP

As pointed out in the beginning of this chapter we are searhing for QGP. If a phase transition has occurred, there are certain features of the system of particles radiating out of the hot and dense zone that may be expected. Our experiment is designed to look for some of these features. In the following section these features and a general overview of the experiment and the analysis will be outlined.

2.3.1 Some Signals of QGP

Strangeness Enhancement

For all heavy ion collisions, the initial baryons consist only of up (u) and down (d) quarks. In this scenario all the strange s quarks existing after the collision must have been created in the collision.

Estimates using chiral pertubation theory [8], predicts the strangeness content $\eta_s = \frac{2\langle N|\bar{s}s|N\rangle}{\langle N|\bar{u}u+\bar{d}d|\rangle}$ in a hadronic phase and temperature $T = 200$ MeV as $\eta_s \approx 0.20$. $\langle N|\bar{q}q|N\rangle$ is the QCD matrix elements of the scalar quark current. For the same temperature, but in a

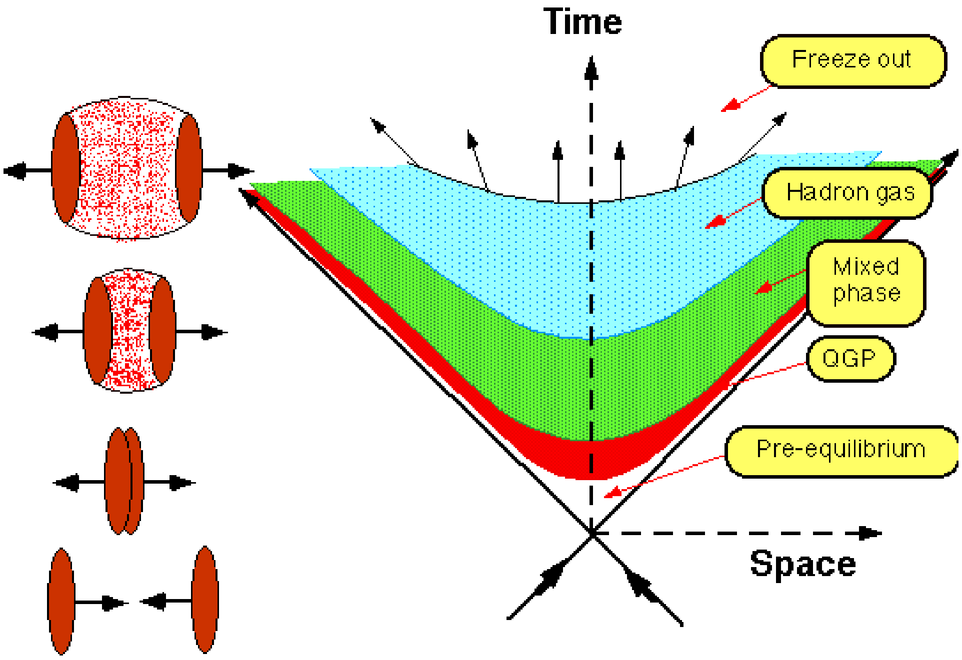

Figure 2.8: The development in space and time for nucleus-nucleus collision.

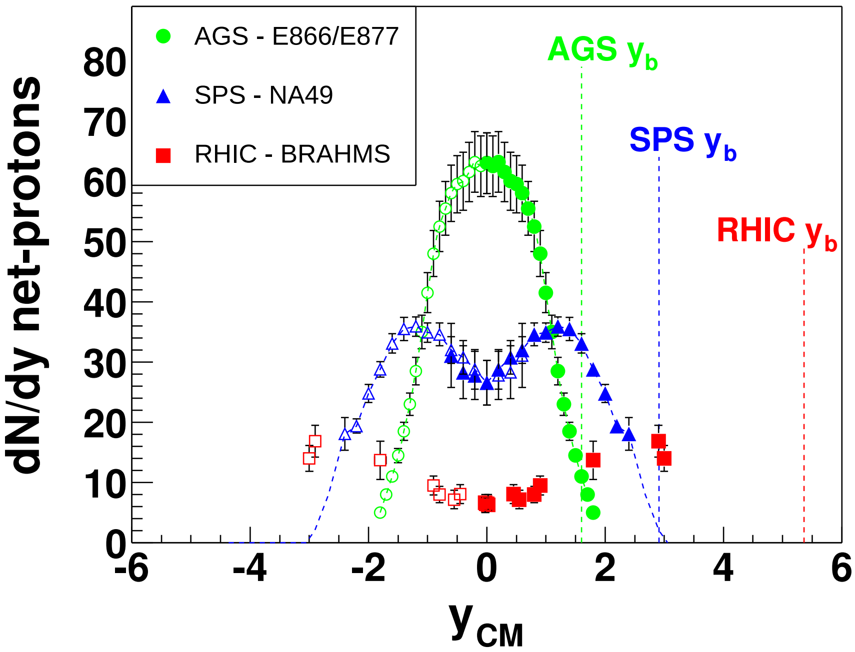

Figure 2.9: Net-proton distribution, with the beam rapidities shown as dotted lines. Figure gotten from private communication with Claus Ekman, and the BRAHMS date are taken from [7].

QGP phase, calculations give $\eta_s \approx 0.42$, the so called strangeness enhancement. Furthermore the threshold energy for production of hyperons-antihyperons in a hadronic phase is ≈ 2 GeV and in a QGP phase only $2m_s = 0.3$ GeV, where $m_s = 150$ MeV is the strange quarkmass, since in the latter case s quarks can easily recombine with u and d quarks. The enhancement will be larger for particles with more strange quarks. In figure 2.10 different collision systems for same energies are shown. The kaon to pion ratio is clearly higher for heavier collision systems, where more particles are created inside the fireball of the collision and the probability for a strange quark to bind with an up or down quark is higher.

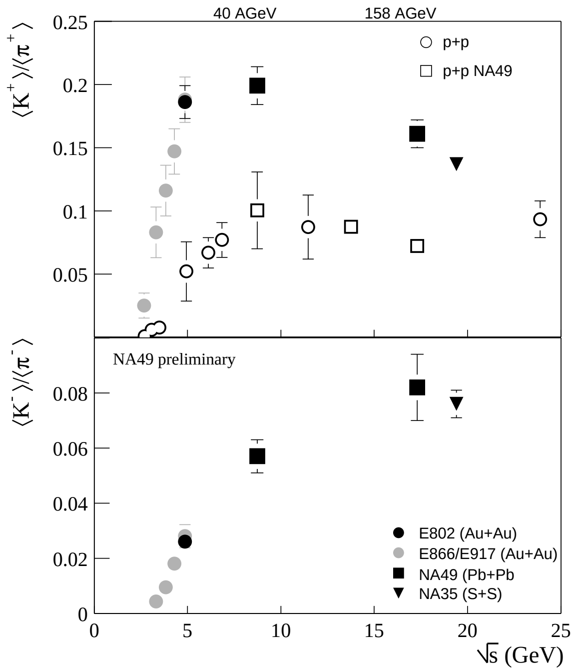

Figure 2.10: Kaon to pion ratio for different collision systems, data from [9]

In figure 2.11 the kaon to pion ratio as a function of beam energy is shown. For lower energies there is a steady increase in the ratio. The ratio reaches a saturation for positive particles around 5 GeV, but for negative particles the increase continues up to current maximum available energies 200 GeV. The peak in the positive particles is due to the primary baryons, which never are anti-particles. At AGS energies there are primary baryons left in the collision zone and there are more particles than anti-particles for the strange particles to bind with. In a mesonic system, due to color confinement, a quark always bond with an anti-quark. At RHIC energy, the same phenomenon is observed at rapidity $y = 3$, where there are primary baryons left after the collision.

J/Ψ Suppression

The J/Ψ meson consists of a charmed c and an anticharm $\bar{c}$ quark. For this meson to exist one must have a minimum potential energy as a function of the distance r between the quarks or in other words a bound state. This bound state exists in the hadron state, but breaks down

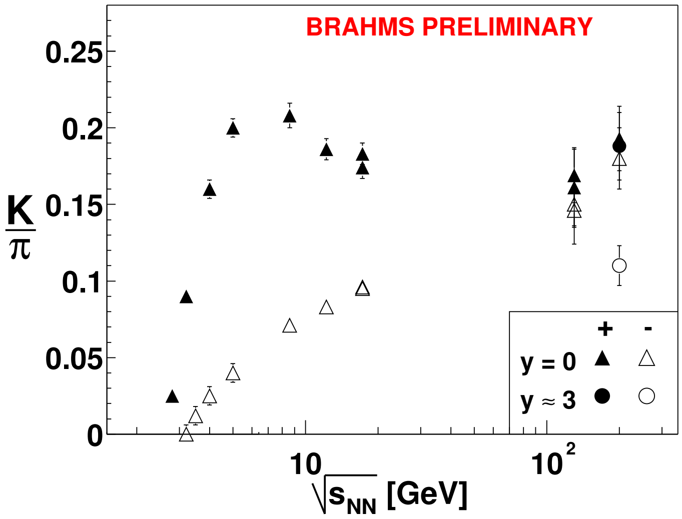

Figure 2.11: Kaon to pion ratio as a function of beam energy. The different data points are taken from [10, 11, 12, 13] for energies below $\sqrt{s_{NN}} = 5$ GeV, and for energies between 5 and 20 GeV from [14, 15, 16]. For energies at 130 GeV data points are taken from [17, 18], and the BRAHMS 200 GeV from [19].

in the QGP phase.

In QGP at RHIC, these color objects screen each other. There is a high density of light quarks (u, d, s), antiquarks and many gluons. Due to this screening the bound state potential disappears and the $c\bar{c}$ can no longer exist. Furthermore the quarks are no longer bound so the charm quarks move around. When hadronizing the charm quarks bind together with lighter quarks to create open charm mesons D rather than J/Ψ particles. Thus J/Ψ suppression has been proposed as a clear signal of QGP. But, J/Ψ could also be suppressed due to breakup, following collisions with for example pions. Shown in figure 2.12, from [20], are two situations. One where data are compared with non QGP absorption models and one comparing data with models including the phase transition. There is a strong similarity between the two figures. Furthermore the paper argues a strong suppression at low p_t. At RHIC there is an increase in low p_t pions due to multiple scattering and heavier particles decaying. Also shown in the spectra, chapter 5. These pions could be the answer to this suppression.

Jet Quenching

The initial collisions between the primary nucleons, the so called hard processes, can produce highly energetic particles. These particles have a much higher momentum than the average particles coming from rescattering among the collision products. Jets can be seen for small collision systems. For large collision systems, where phase transition has occured, these jets are supressed. The highly energetic quarks are slowed down, when interacting with other quarks in the plasma. Therefore there should be less high p_t hadrons (from jets) radiating out of the hot and dense zone if phase transition has occured. The energy lost in these interactions gives a broadening in the total transverse momentum p_t and a suppression of the high p_t part of hadron spectra. Thus a measurement of the broadening in p_t should give a signal of QGP.

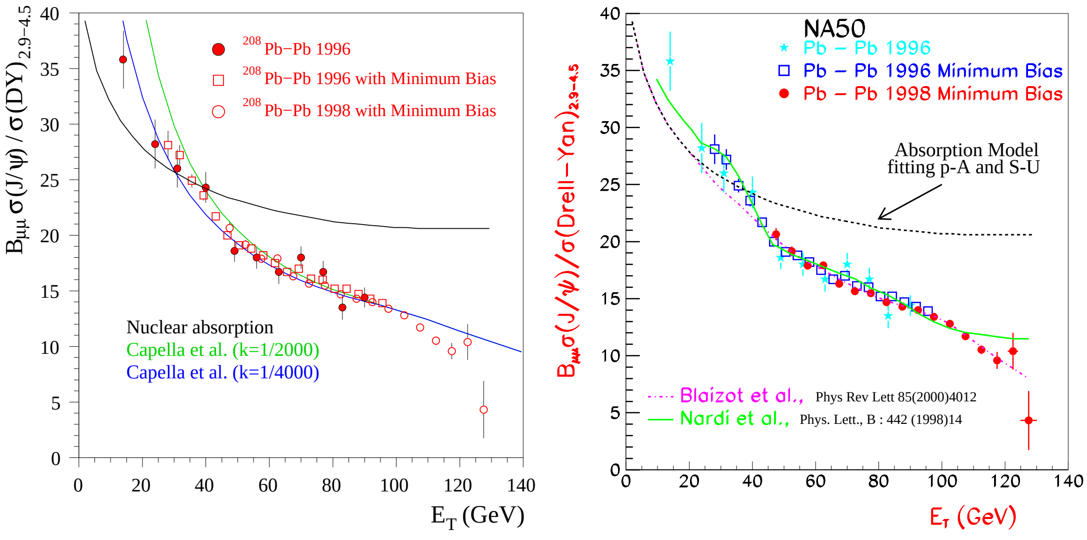

(a) no phase transition

(b) phase transition

Figure 2.12: Left. Some theoretical models based on absorption from comoving hadrons. Right. Models including the QGP phase transition.

2.4 Analysis Outline

There are certain other observables from the nuclear collisions we can analyze and which tell us about the reaction mechanics and the source dynamics.

2.4.1 Multiplicity

The multiplicity is a measurement of how many particles that are radiated out of the collision zone. In BRAHMS we can only measure the multiplicity of electrically charged particles.

The charged particle production is very dependent on the parton-parton scattering for the different stages in the collision. Thus, when charged particles radiate out from the collision region their density distribution and multiplicity may tell us about the collision-development. The recent results of multiplicity measurements from RHIC are presented in figure 2.13 taken from [21] with $\sqrt{s_{NN}} = 200$ GeV.

Another measurement is the particle production per nucleon pair as a function of centrality, figure 2.14, taken from [21]. For lower pseudorapidities particle production increases with the number of participants. This is due to hard-scattering processes, which are dependent on the number of binary nuclen collisions.

2.4.2 Particle Ratios for Identical Particles

The particle ratios tells us about the collision features. One example is the $N(\bar{p})/N(p)$ which tells us about the stopping and transparency, section 2.2.1.

The ratios $N(\pi^-)/N(\pi^+)$, $N(K^-)/N(K^+)$ and $N(\bar{p})/N(p)$ as a function of the transverse momentum p_t tell us about the charged particle distribution in the hot and dense region [24]. In a transparent Bjorken scenario these ratios should be constant for rapidities close to $y = 0$.

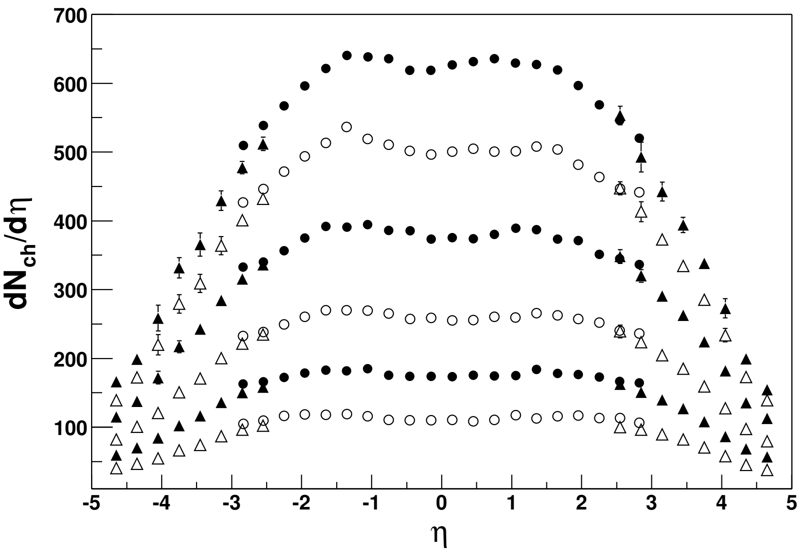

Figure 2.13: Charged particle pseudorapidity η density versus pseudorapidity η measured in BRAHMS for CM energies $\sqrt{s_{NN}} = 200$ GeV. Pseudorapidity is defined in appendix A. The different symbols are different centralities, from top to bottom $0-5\%$, $5-10\%$, $10-20\%$, $20-30\%$, $30-40\%$ and $40-50\%$. The circles and triangles represent SiMA and BBC respectively. Statistical error are shown for points where larger than symbol size. Systematic errors are 8% and 10% for the SiMA and BBC respectively.

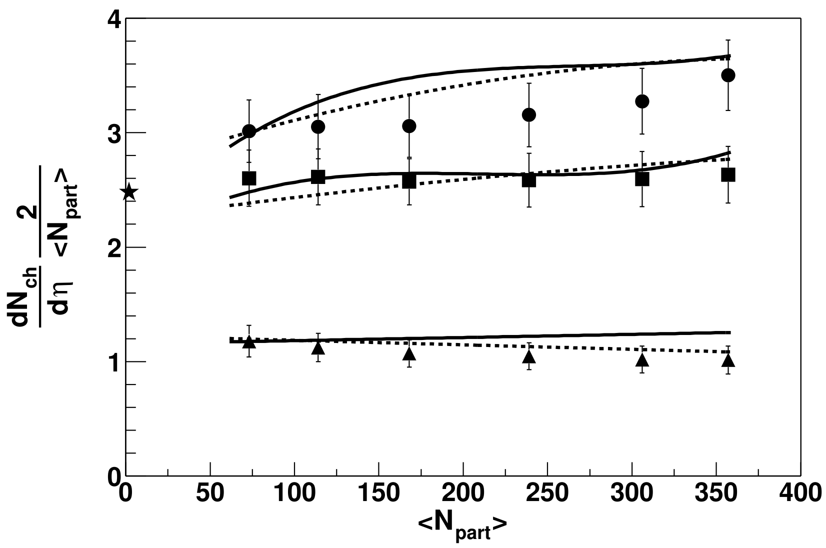

Figure 2.14: The number of produced particles per nucleon pair for the pseudorapidities $\eta = 0$ (circles), 3.0 (squares) and 4.5 (triangles) versus centrality (here as number of participants). Also shown are predictions by Kharzeev and Levin (solid line) and the AMPT model (dashed line).

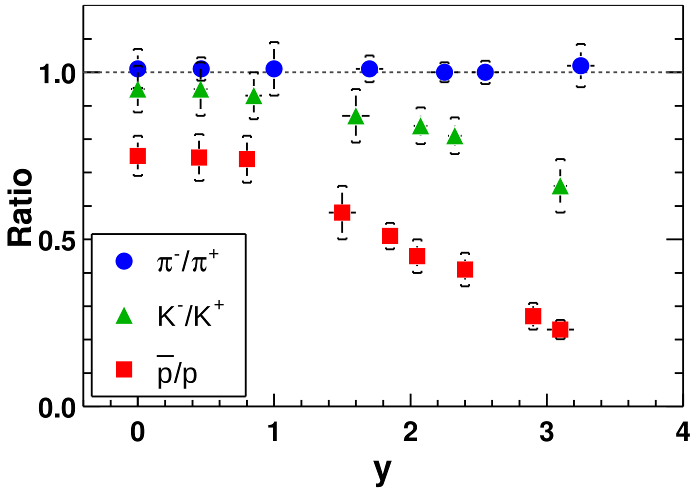

Figure 2.15: Anti-particle to particle ratio versus rapidity taken from [22].

The primary protons are expected to be at much higher rapidities, shown in figure 2.15, where there is a Bjorken plateau for rapidities lower than $y = 1$.

For a high stopping scenario, the situation would be different. Here we have a lot of primary protons in the hot and dense region. The creation of π^- requires $\bar{u}$s. Due to baryon conservation the probability for a $\bar{u}$ to be created in a proton dense region is much smaller, since this would reqiure the creation of a corresponding u quark. Furthermore the Coulomb interaction will repel the very low momentum positive pions and Kaons and correspondingly attract very low momentum negatively charged pions and Kaons.

So far only ratios of the same type of particles have been discussed. For the same particles we have the same acceptance corrections, efficiencies in the detectors etc. Therefore all these factors cancels out and we do not have to worry about them.

To find the ratios for different particle types we need the normalized number of particles. To get this we need to find the acceptance corrections, efficiencies etc for each type of particle. After corrections we can estimate the yields (section 2.4.3).

2.4.3 Particle Yields

The number of particles, normalized to number of collisions in a certain rapidity region is called the yield for that region. By comparison of the yields with a thermal model one can explore whether there is chemical equilibrium and try to determine the temperature of the hot and dense zone. The requirement for the thermal model to be used is that there is a thermal and chemical equilibrium through out the collision. Whether this requirement is fulfilled is still debatable and has yet to be proved. In figure 2.16 the anti-kaon to kaon ratio is plotted vs anti-proton to proton ratio. Also shown is the thermal model based on Becattini et al [23], assuming $T = 170$ MeV (full line). Also shown is the relation $K^-/K^+ = (\bar{p}/p)^{1/3}$ (dotted line).

To find the yields we need first to have the acceptances and efficiency corrections. The way to find these are described in chapter 5. After the data has been corrected they are fitted

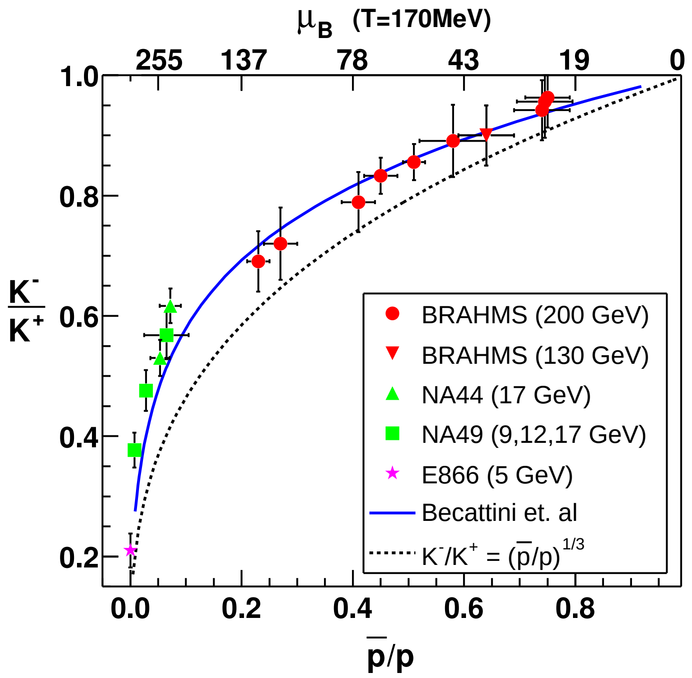

Figure 2.16: Strange meson ratios versus anti-particle to particle baryon ratios. Figure taken from [22].

with an exponential function

$$\frac{1}{m_t}\frac{d^2N}{dydm_t}\bigg|_{y=y_0} = Ce^{-\frac{m_t}{T}} \quad , \tag{2.2}$$

from which one obtain the temperature, the particle yield is the integral of the fitted function over the full m_t range. m_t is the transverse mass defined in appendix A. y is the rapidity and T the temperature inside the medium. Results may be compared to the thermal model. This has been done for SPS data in [25]. For RHIC data, yields and temperatures are only now becoming available. This thesis adresses such results for the BRAHMS experiment, (chapter 5).

2.4.4 Transverse Flow

The expansion of the hot and dense region in the transverse direction may provide information on how the matter expands, for example if there is a hydrodynamical flow of the matter. This would imply (at least) thermodynamical equilibrium. This can be explored by measuring the transverse kinetic energy of the radiated particles. Spectra of particles can be fitted with a Boltzmann distribution [28] as a function of p_t or m_t,

$$\frac{dN}{m_t dm_t} \propto e^{-\frac{m_t}{T}} \quad . \tag{2.3}$$

Here T is the inverse slope parameter which is equal to temperature only if there is no flow. Slope parameters for different particle species can be described by a model that takes the transverse flow into account. T can then be written as

$$T = T_{therm} + m < v_t >^2 \quad , \tag{2.4}$$

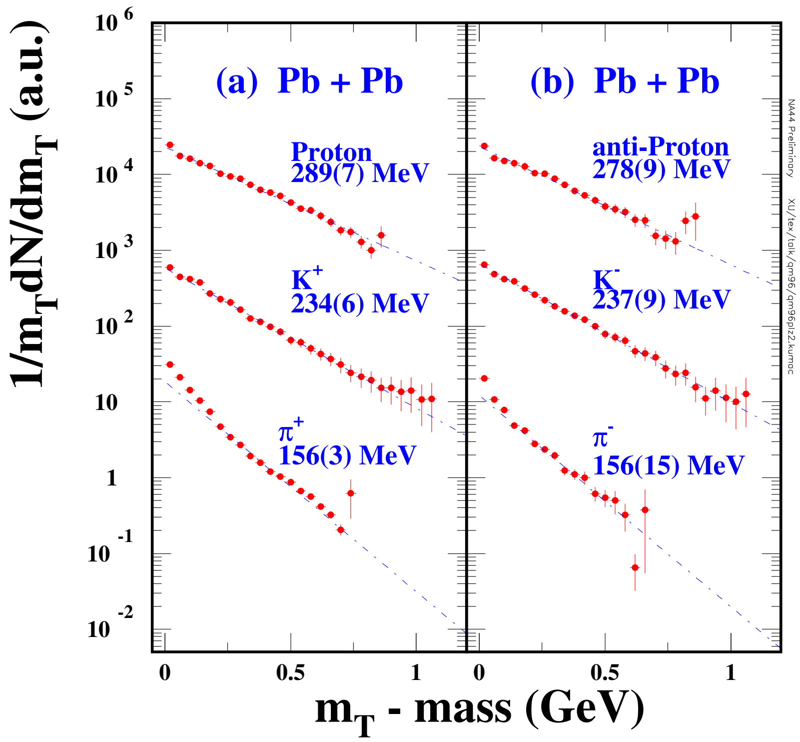

Figure 2.17: Thermal m_t spectra from the NA44 Pb+Pb 158 GeV/nucleon experiement at SPS. Figure taken from [26].

where T_{therm} is the freeze out temperature, m the mass of the specific particle and $< v_t >$ the average transverse flow velocity. Measurements have been done for different collision systems at SPS, as shown in figure 2.18. In chapter 6 such results for $\sqrt{s_{NN}} = 200$ GeV Au + Au collisions from this thesis are presented.

2.4.5 Deuteron, Triton Production and Coalescence

The process by which heavier particles, like deuterons and tritons are produced, in the collision region is coalescence.

Due to low binding energy for deuterons and tritons (a few MeV) it is impossible for these particles to be created in the early hot and dense stages of the collision. Therefor these particles are created in the final stages near freeze out. The probabilities for protons and neutrons to be close enough in phase space to bind into deuterons and tritons are inversely proportional to the size of the radiating source. Thereby the coalescence factor B_2 equal to the ratio of cluster particles and (single particles) squared, gives information about the size of the collision zone at freeze out. More information on the subject can be found in [29, 30].

2.4.6 Two and Three Particle Correlation

A way to investigate the temporal and spacial development of the collision is to look for two and three particle interference correlations. The probability for detecting identical particles in the same phase space region interfere. This interference is a well established quantum mechanics phenomenon, HBT [1, 31]. Measurements of the correlation function give away

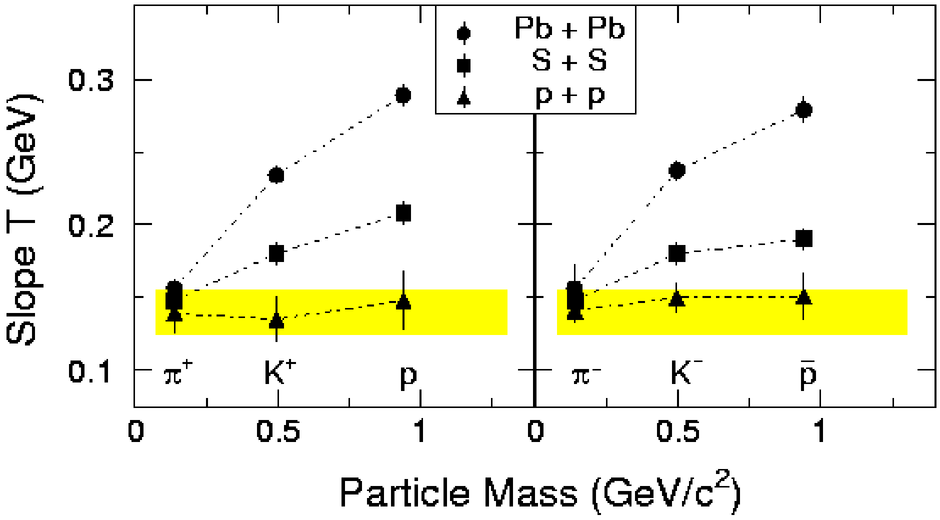

Figure 2.18: The inverse slope parameter T as a function of mass measured by the NA44 experiment at SPS [27].

information about the collision characteristics namely the source size. Often there are problems in interpreting the results independent of a model because the results strongly depend on flow. For increased knowledge in the subject look into [32].

Chapter 3

The BRAHMS Experimental Setup

This chapter gives an overview of the experimental apparatus of the BRAHMS experiment. BRAHMS stands for *B*road *RA*nge *H*adronic *M*agnetic *S*pectrometers.

3.1 RHIC Relativistic Heavy Ion Collider

The overall goal of relativistic heavy ion physics is to create and observe matter at extremes of temperature and density. The source of heavy ions is the RHIC *R*elativistic *H*eavy *I*on *C*ollider.

There are several steps in the acceleration procedure. These include stripping off the electrons from the Au nuclei to be accelerated and increasing the energy of the nuclei in different sectors of the accelerator. A schematic picture of the accelerator system is illustrated in figure 3.1, in which the major components of the system are labeled. By following the different sectors a schematic step by step description of the acceleration process is given here, see also in [33].

1. The ion source creates Au ions with a charge of -1.

2. The Tandem Van de Graff accelerator accelerates these ions in two major steps. First it uses the negative charge of the ions to accelerate them. Then it strips the ions of approximately 6 additional electrons and accelerates the ions further a bit before even more electrons are stripped off. Now the ions have a broad charge distribution and the ions with the highest charge +14 are selected by separation in a magnetic field.

3. The Heavy Ion Transfer Line transports the ions to the Booster. Now the ions have an energy of 1 A·MeV.

4. The BOOSTER stacks the ions up into bunches and accelerates them up to an energy of 95 A·MeV.

5. From the Booster the ions go through one more additional stripping foil and loose further electrons. The charge of the ions, when entering the Alternating Gradient Synchrotron (AGS) is +77. In AGS the stacking and acceleration continues. The final result is 4 bunches and an energy of 10.8 A·GeV.

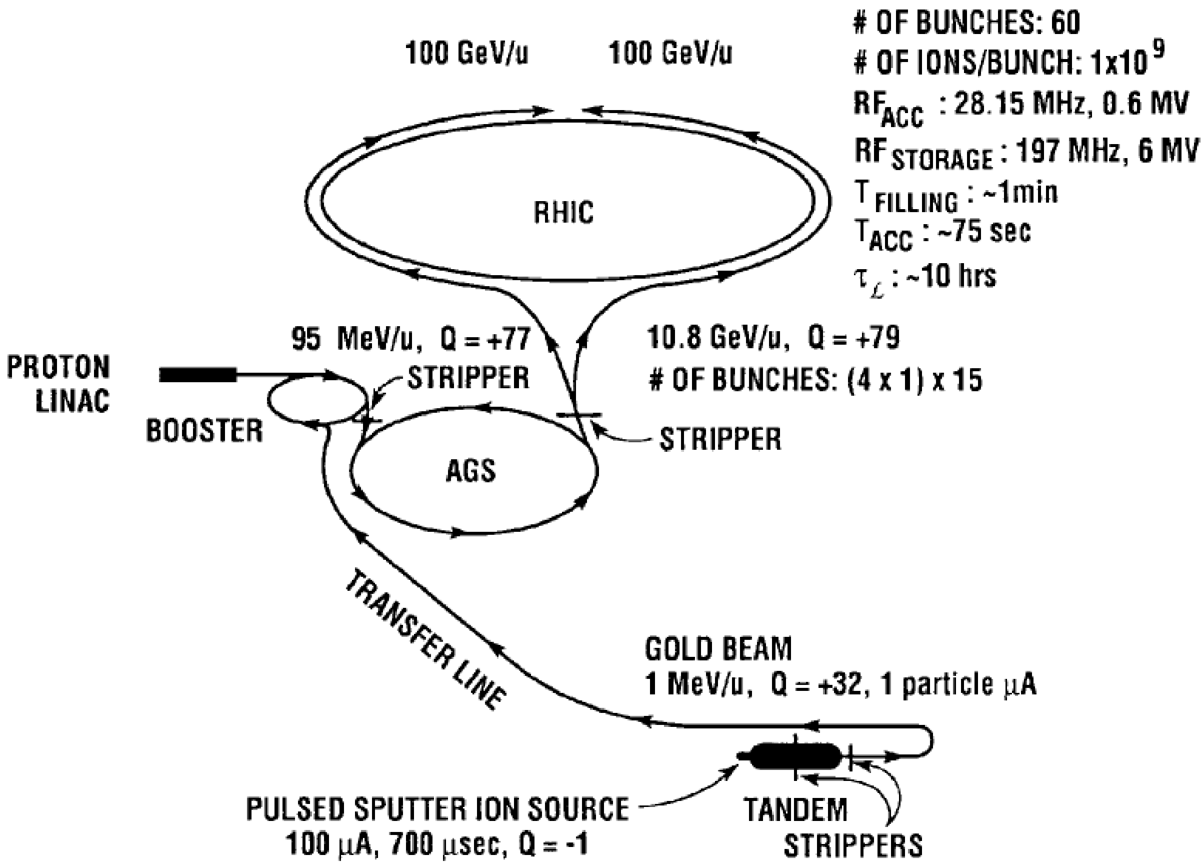

Figure 3.1: An overview of the RHIC facility, with its different accelerator systems. The gold nuclei goes through several different sectors before they reach their final energy of 100A·GeV.

6. On the way from AGS to RHIC the remaining electrons are stripped of the ions to a charge +79. Before entering RHIC the beam is split up in two, which enter RHIC in opposite directions. The RHIC ring itself has a circumference of 3.8 km. Here the ions are stacked in 55 bunches and accelerated to their final energy of 100 A·GeV. For Au+Au this gives the center of mass energy of $\sqrt{S_{NN}} = 200$ GeV.

The two beam lines are brought together in 4 collision regions where the experiments (BRAHMS, PHOBOS, STAR and PHENIX) are situated. In the crossing sections the beams collide at a small angle, so the collision distribution is determined by the length of the bunches.

Beam luminosity

The luminosity $\mathcal{L}$ is defined as

$$\mathcal{L} = \frac{N^2}{A \cdot \Delta t} \quad , \tag{3.1}$$

where N is the number of particles per bunch, A the cross section of the beam and Δt is the time width of the bunch. The reaction rate can then be written as

$$R_{react} = \frac{N^2 \cdot \sigma}{A \cdot \Delta t} = \mathcal{L} \cdot \sigma \quad , \tag{3.2}$$

where σ is the nuclear cross section and the rest of the symbols as above. The designed luminosity for RHIC is 10^{26} cm^{-2}s^{-1}, which gives approximately 1200 minimum bias collisions per second. This has recently been achieved (y2001).

3.2 BRAHMS Experiment at RHIC

The experimental design of BRAHMS is made in such a way that the experiment can measure charged particles, mainly hadrons, over a broad rapidity range. For this to be possible within a reasonable cost two spectrometers with small solid angle have been built, one for the midrapidity region and one for higher rapidities. Figure 3.2 shows a top view of the BRAHMS spectrometers. The forward spectrometer detects particles at higher rapidities ($y = 1$ to 4). It is split up in two sections FFS front forward spectrometer, which moves from 2.3° to 30° and the BFS back forward spectrometer, which moves between 2.3° and 15°. The midrapidity spectrometer is movable between 95° and 30°, and covers $0 < y < 1$ (pions). The fact that the spectrometers rotate about the collision zone gives BRAHMS its unique ability to measure over a a large range in rapidity. For more information on the experimental setup, see [34].

3.2.1 The Global Detectors

Detectors that measure global effects as vertex and multiplicity are the two beam-beam arrays (BBL) and (BBR), for beam-beam left and right, the two (ZDCs) zero degree counters, one on each side of the vertex region. Further global detectors are the two multiplicity detectors (TMA) and (SiMA) for tile multiplicity array and silicon multiplicity array. See Figure 3.2.

The beam-beam counters (BBC) are situated on either side of the nominal vertex point, 220cm away. The BBCs consist of Čerenkov detectors. The vertex position is determined by the beam-beam arrays which are Čerenkov radiators. They also give the start time of the collision. A schematic view of the BBCs is shown in figure 3.4.

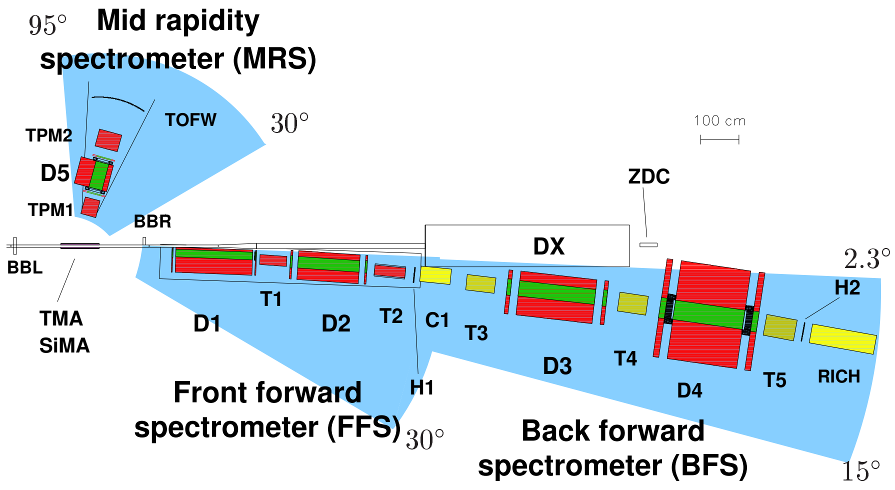

Figure 3.2: A top view of the BRAHMS experiment. The experiment consists of two detector arms, forward and midrapidity detectors. The shaded area shows the geometrical coverage of the detector arms.

The TMA and SiMA are situated around the beam pipe (figure 3.5). They measure the overall charged particle multiplicity, by measuring the energy loss of particles passing through the two arrays. The number of particles passing through an element is determined by dividing the total energy observed with the energy loss of a single particle determined by GEANT simulations. The arrays cover a region of $-2.2 < \eta < 2.2$ in pseudo-rapidity for collisions occurring at the nominal vertex point. To interpret the measurements from the multiplicity arrays model calculations are required. In figure 2.5 the percentage lines stands for the most cenntral collisions. Example 10% means the 10% most central collisions.

The ZDC are situated 18m from the nominal vertex point. They measure spectator neutrons. Thereby they measure the vertex position. The neutron multiplicity is correlated with the collision geometry [35]. The more central a collision is the less fast forward moving particles are found at small solid angles around the beam axis [36]. Therefore the ZDCs can be used together with data from the multplicity array and the beam-beam counters to estimate the centrality of the collision. All experiments at RHIC are equipped with ZDCs and cuts on the ZDC response provide a way to compare results from the different experiments.

3.2.2 MRS the Midrapidity Spectrometer

The midrapidity spectrometer consists of four major items. These are the two time projection chambers (TPCs) TPM1 and TPM2, the magnet D5 and the time of flight wall (TOFW).

The TPCs are placed on each side of the magnet, and are used to determine the trajectory of particles (how this is done will be explained below). Since there are tracks on each side of the magnet the arcs or the bending angles in the magnet can be calculated. All particles detected so far, have the charges plus or minus one. The magnetic field of D5 is known and from the bending force on a moving charge in a magnetic field (figure 3.7) the momentum to charge ratio p/q can be calculated, since the magnetic force is equal to the centripetal force. We have to take relativistic effects into account since the TOFW together with the beam-beam counters measures the flight of time, which gives the relativistic velocity β. Rembering the relativistic gamma factor

$$\gamma = \frac{1}{\sqrt{1-\beta^2}}, \tag{3.3}$$

where β is the velocity. The relativistic mass is $m = \gamma m_0$, with m_0 as the rest mass.

$$F = q\beta \times B = \frac{m\beta^2}{r} \tag{3.4}$$

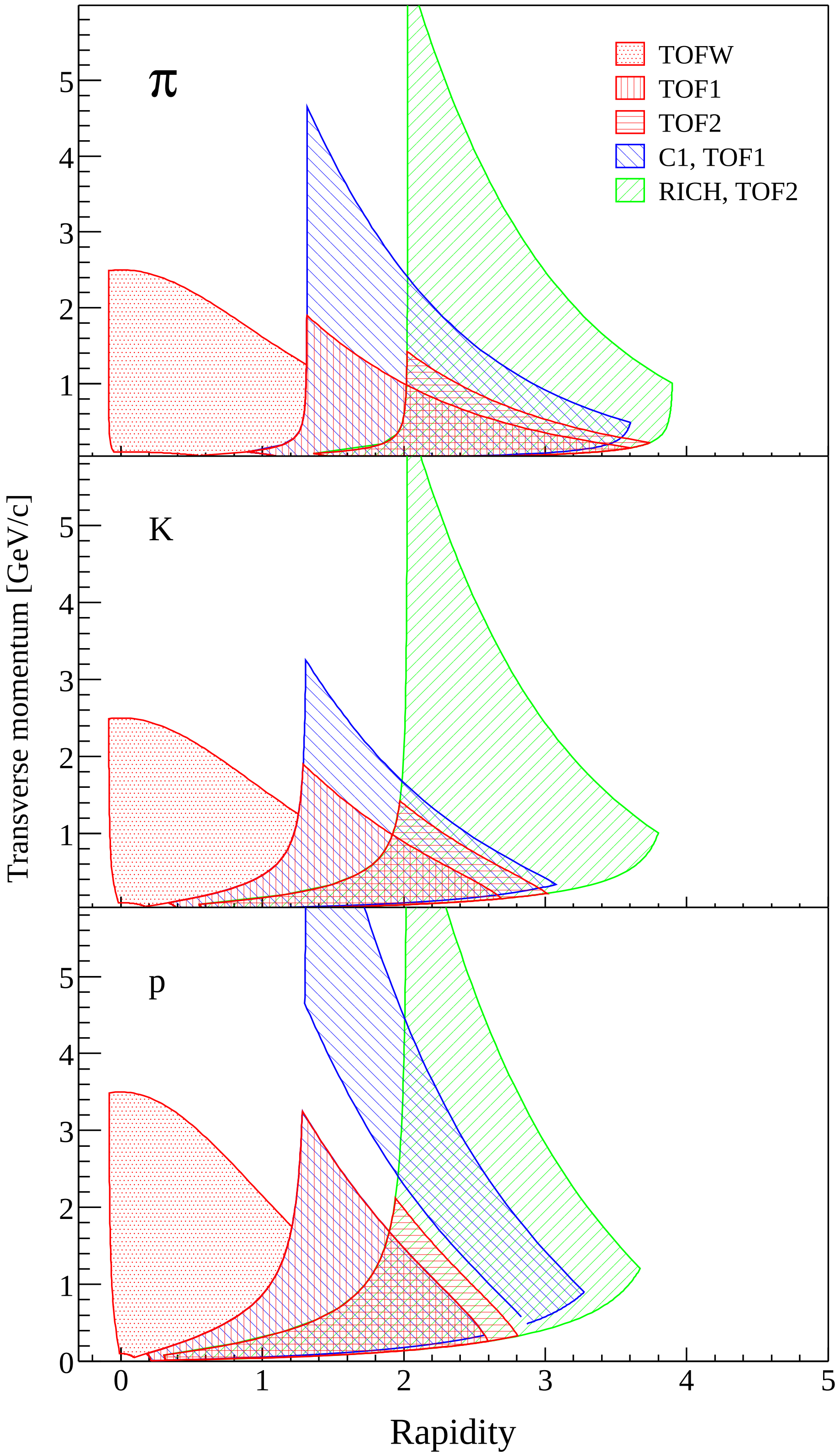

Figure 3.3: The overall acceptance for the BRAHMS experiment in rapidity and transverse momentum. The different patterns show the different detectors particle identification ranges for pions, kaons and protons.

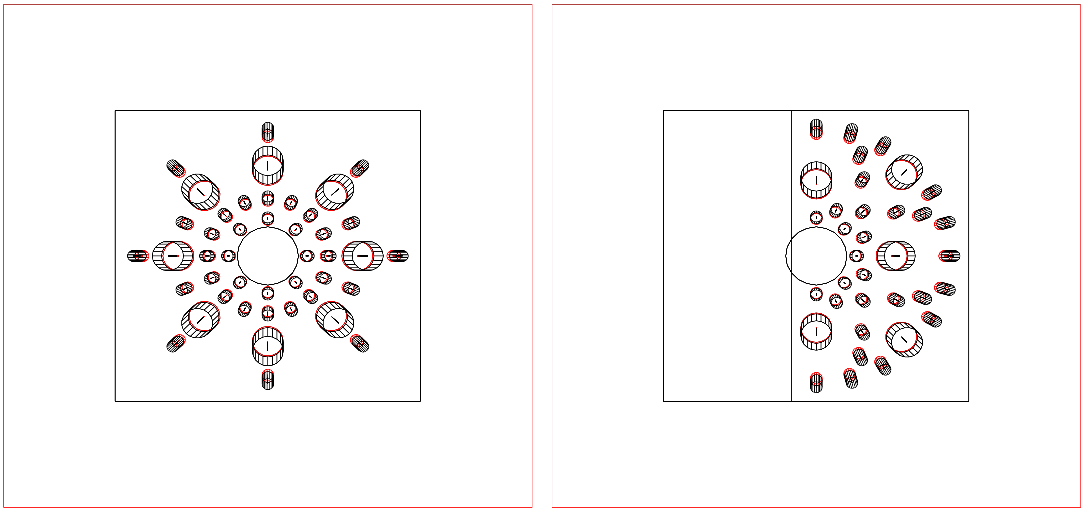

(a) Left array (b) Right array

Figure 3.4: The beam-beam arrays seen from the beam pipe. Left. The left beam-beam array. The Čerenkov detectors are placed in circles around the beam pipe at very forward angles. Right. The right beam-beam array. Due to visibility of the forward spectrometer, some detectors are removed.

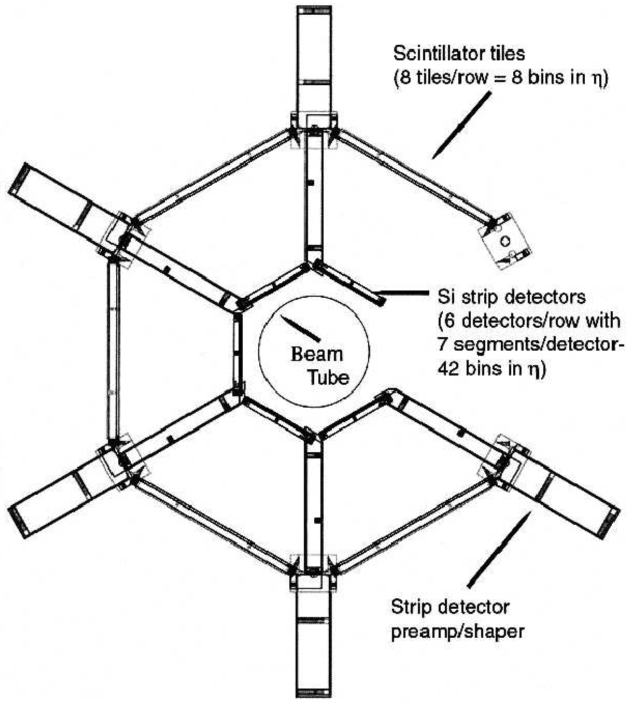

Figure 3.5: The multiplicity array seen from the beam pipe. Shown is the inner SiMA and the outer TMA.

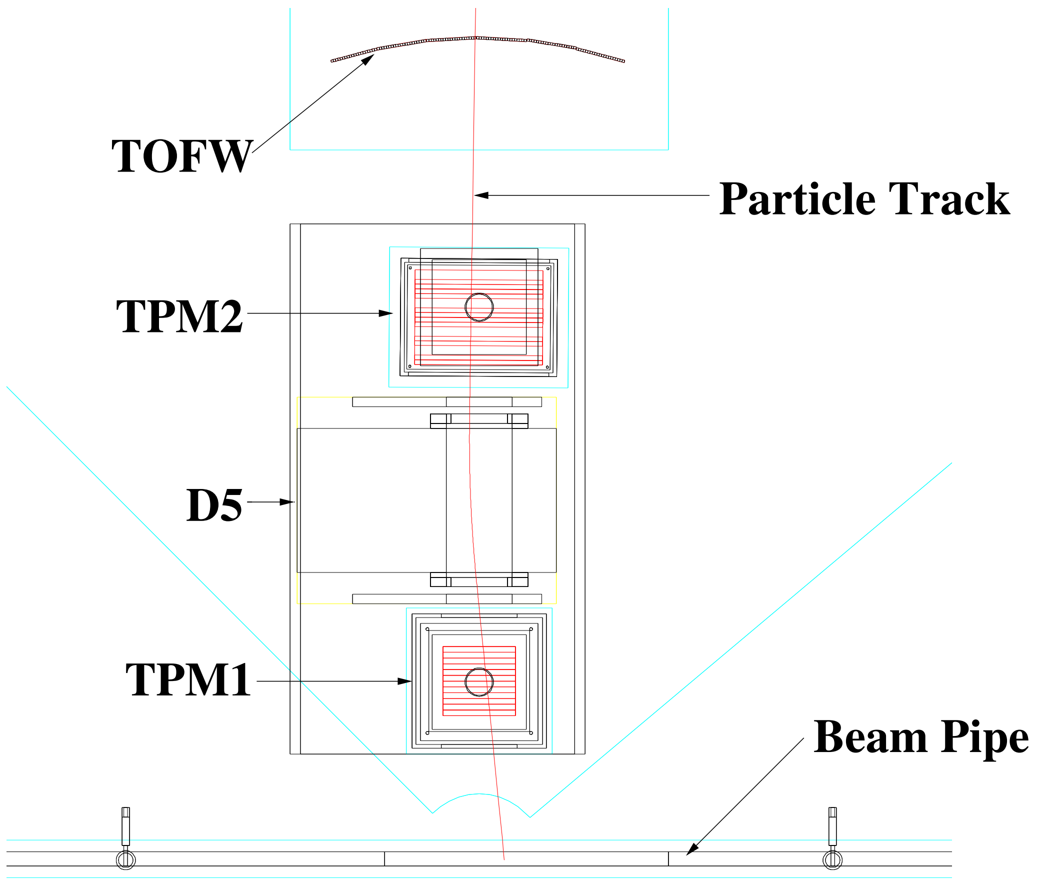

Figure 3.6: An overview of the MRS with a simulated particle flying through it. The picture shows the different detectors and the magnet between them. Notice how the particle track bends due to the magnetic field inside the magnet.

B is the magnetic field, m the relativistic mass and beta the velocity of the particle. The speed of light and the electrical charge is set to unity, (c=q=1). So the momentum can be written as

$$p = Br = m\beta = \gamma m_0 \beta. \tag{3.5}$$

The radius is known from the TPCs and the velocity β from the time of flight. The magnetic field B is also known, thereby the momentum is known and the mass can be calculated. By squaring the momentum equation 3.5 becomes

$$p^2 = (m_0 \gamma \beta)^2. \tag{3.6}$$

From expressions 3.3 and 3.6 the mass squared m^2 can be calculated.

$$m^2 = p^2 \left(\frac{1}{\beta^2} - 1 \right) \tag{3.7}$$

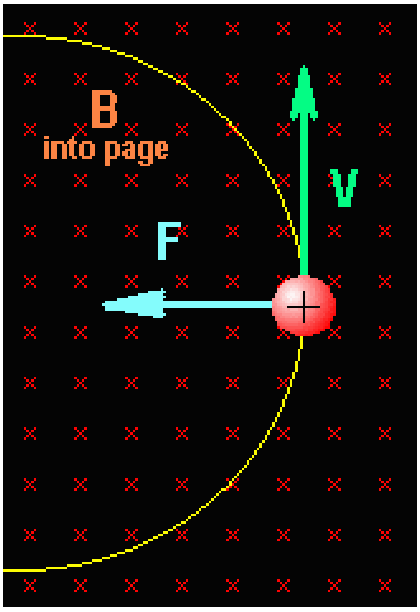

Figure 3.7: A charged particle moving in a magnetic field is influenced by the force $F = q\beta \times B$.

Due to the finite time resolution in the TOFW (60 ps) there is a limit to how high momentum a particle can have and still be identified by time of flight. This limit is 2 GeV/c for π/K separation and 3.5 GeV/c for K/p separation [34].

An introduction to the TPCs

As mentioned above the TPCs are used to determine the trajectory of the charged particles. A TPC is a volume filled with gas put in an electrical field. When charged particles travel through the box they ionize the gas molecules inside the box. The ions begin to drift inside the electrical field. The liberated electrons drift toward the read out volume of the TPC. This part of the TPC, which is shown in figure 3.8, consists of a gating grid, catode wires, field and "sense" wires and a pad plane. The sense wires are held at a large positive voltage (ca. 1200V). Since the sense wires are very small in diameter(15 μm) the electric field density is extremely high in the neighborhood of these wires, and the electrons which drift avalanche giving rise to a current on the sense wire. This in turn, induces a measurable charge on the readout pad, placed few mm away. The pad plane gives the local x and z positions. The y position is found using the drift time and the drift velocity the electrons have, when drifting toward the pad plane. The drift velocity is known and much smaller than the velocity of the particles entering the TPC. Thereby also the flight time is much smaller than the drift time. To find the y position, the detector electronics only has to be triggered before the first electrons reach the readout of the TPC. For more detailed explanation of TPM1 and TPM2 see [34] and TPCs in general see [37].

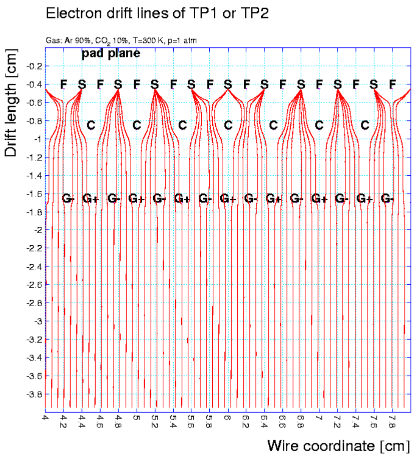

(a) The electrical field is shown as the thin lines from bottom to top, where the pad plane is placed. The different wires are G for Gating grid, C for cathode, F for field and S for sense wires, all running perpendicular to the paper.

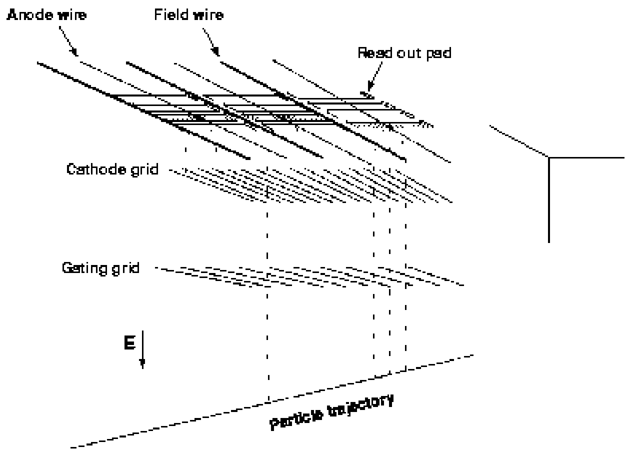

(b) A particle travels through the detector and electrons drift toward the pad plane.

Figure 3.8: The TPCs are gas boxes with a strong electrical field inside. Near the pad plane thin wires create electron avalanches strong enough, to induce signals on the segmented pad plane.

The time of flight wall TOFW and MRS PID

The TOFW consists of scintillator slats with photo-multiplier tubes connected to both ends of each slat. When a particle passes through a scintillator electrons in the scintillator atom are excited and give away light when falling back into their ground state. This light is registered by the photo-multipliers mounted at the end of the slats. The slat position gives the x coordinate and the differense in the time given by the two photo-multipliers allow us to calculate the y position.

Assuming that the first particles to hit the TOFW are pions, we can perform a calibration which allows us to convert the timing signal of the slats to a flight of time. Knowing this, and the distance the particles traversed from the known (via BBC) vertex, we can calculate the particle velocity associated with each reconstructed track. From equation 3.7 the mass leading to the particle identification (PID) can then be calculated.

3.2.3 The Forward Spectrometer (FS)

The forward spectrometer is what gives BRAHMS its unique ability to measure at forward rapidities. It registers particles at rapidities ($1 < y < 4$), which is higher than any other experiment at RHIC. It is split up in two sections, the Front Forward Spectrometer (FFS) and the Back Forward Spectrometer (BFS). The FFS can be rotated from 2.3° from the beam pipe to 30° degrees and the BFS from 2.3° to 15°, (figure 3.2).

The Front Forward Spectrometer

The FFS is built on the same principles as the MRS. Two tracking devices (TPCs) at each end of a magnet (D2) provied a measurement of momentum, and a time of flight wall provides PID. The big difference is at the front of the detector arm, where a dipole magnet (D1) is attached to sweep away undesired particles. There is also a Čerenkov detector (C1) attached at the back of the FFS.

A Čerenkov detector is filled with a medium, which emits light, when particles traveling through has a velocity greater than the speed of light in the medium. The light is emitted in a cone, with an angle θ_c relative to the particle propagation $\cos\theta_c = \frac{1}{n\beta}$, where n is the refractive index of the gas. The threshold velocity is given by $v = \frac{\beta}{c} = \frac{c}{n}$. The emitted light is picked up by photo-multipliers. C1 has a pion threshold of 2.6 GeV/c and can discriminate between pions and kaons up to the kaon threshold of 9.3 GeV/c.

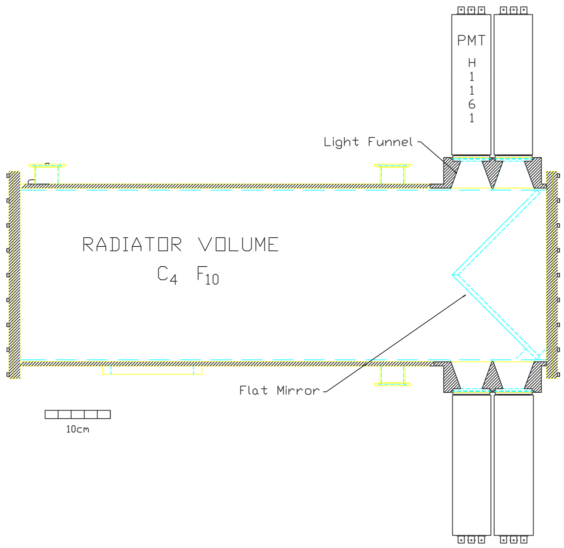

Figure 3.9: A schematic picture of C1, viewed from the side.

The FFS detector is used in two modes. For intermediate momenta it is used for PID and for high momenta it is used as a deflector, where high momentum particles are deflected by the magnets D1 and D2 into the BFS for identification. In the FFS, PID is done in the same way as for the MRS section 3.2.2, with the extension of the PID made by C1. The time-of-flight PID threshold in the FFS is 3.3 GeV/c for k/π separation and 5.7 GeV/c for

k/p separation. A combined picture of the PID for the entire BRAHMS experiment is shown in figure 3.10.

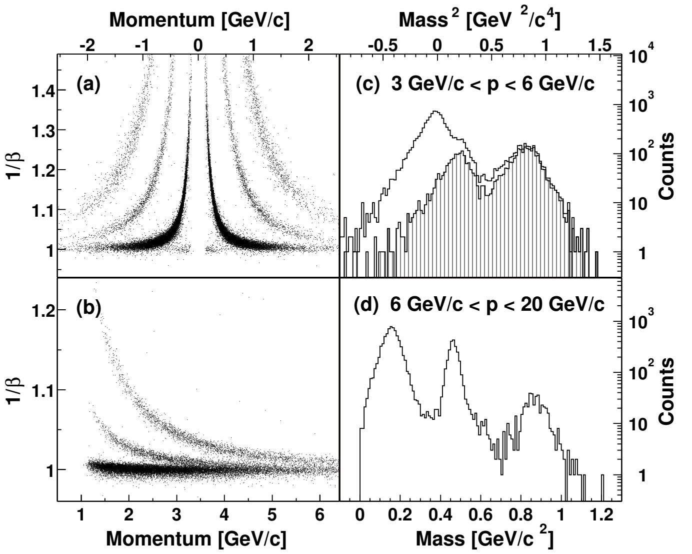

Figure 3.10: The PID capability by (a) the MRS at 90 degrees, (b) the FS at 12 degrees, (c) Mass squared spectrum in the FS measured with the two hodoscopes H1 and H2. The shaded histogram includes pions vetoed out by C1, (d) Mass spectrum in FS using the RICH.

The Back Forward Spectrometer

In the BFS tracking is done by three drift chambers (T3, T4 and T5). T3 is mounted in front of the bending magnets D3, T4 in between D3 and D4, and T5 behind D4. A drift chamber (DC) is like a TPC a gas chamber. Instead of inducing a field on a pad plane as in a TPC , wires are put in the chamber for particle detection. The wires are placed in planes, with different planes containing wires of different spacial orientation, as shown in figure 3.11 figure 3.11. When particles travel through the gas they interact with molecules from the gas, which become ionized. Due to an electrical field the ions are drifting toward the wires. The wires detects the ions and if the drift velocity is known the track can be deduced. T2 and T3 are mounted "in plane" with each other so a comparison between the two is possible.

Placed behind T5 hodoscope (H2) performs PID through time-of-flight. H2 is the third scintillator wall in the experiment. It is placed 19m from the nominal vertex point and can do k/π separation to 5.8 GeV/c and k/p separation to 8.5 GeV/c.

At the rear end of the forward spectrometer the Ring Imagining Čerenkov detector (RICH) is placed. The RICH has a pion threshold of 2.5 GeV/c, and can distinguish pions from kaons to a momentum of 20 GeV/c. Protons can be identified well above 30 GeV/c.

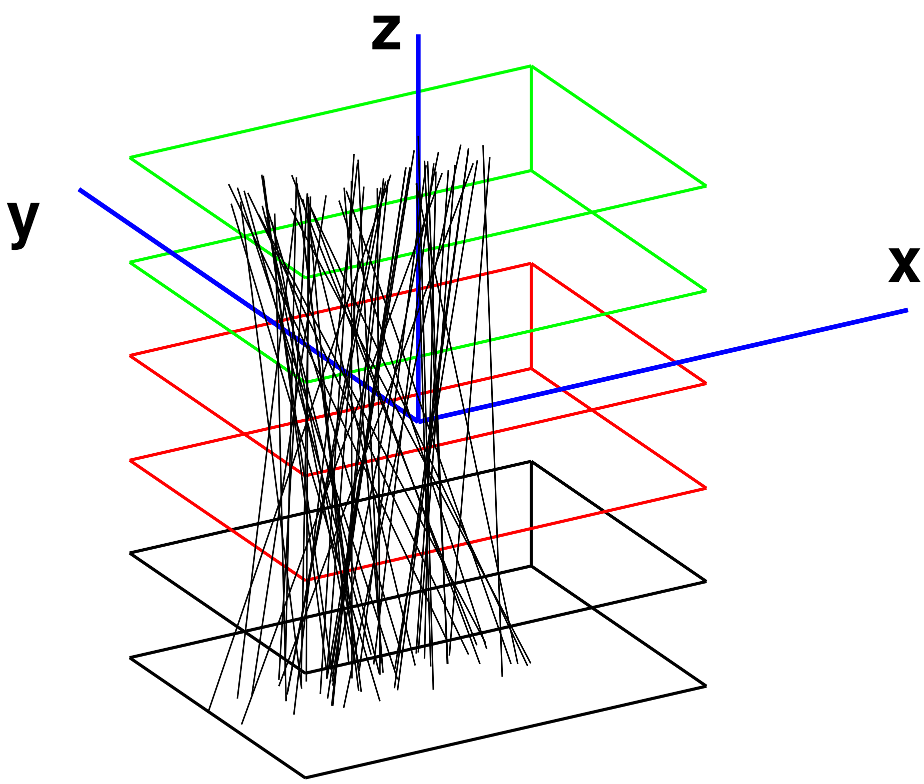

Figure 3.11: Tracking made by T3. Shown are also the planes, where wires are attached. Different colors represent different "views".

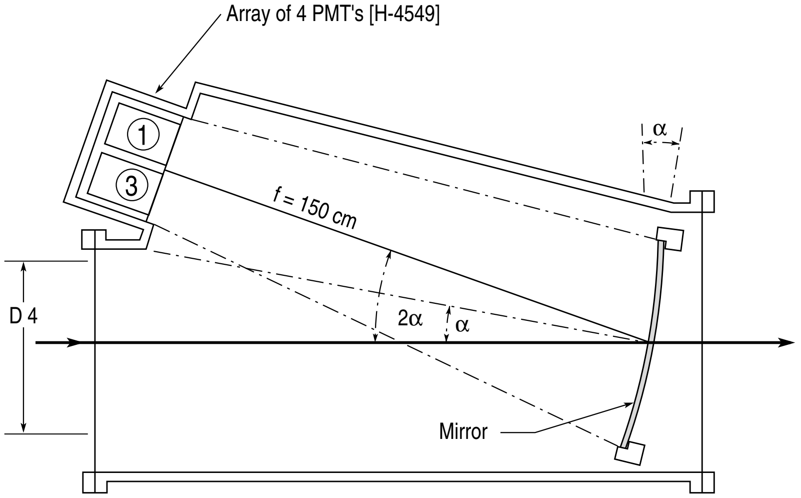

(a) RICH from the side

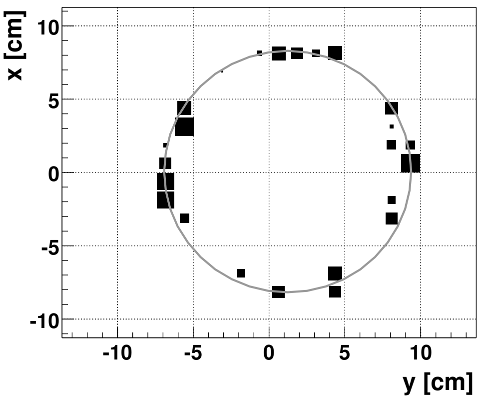

(b) Particle print in RICH

Figure 3.12: Top. A scematic view of RICH, viewed from the side. Bottom. Rings created by emitted photons, used for PID.

Chapter 4

Theoretical Outline

In this chapter I will go through the two models I have chosen to compare the measured single particle distribution data from BRAHMS MRS with, leading to exponential and blast wave fits. The exponential fit descends from a thermal model and the blast wave model is a version of a hydrodynamical model.

4.1 The Thermal Model

The idea behind the thermal model is that you look at a source assumed to be in thermal (and chemical) equilibrium. The source has a constant temperature. Heat is transported by particles leaving the source with a certain momentum distribution. In the same way a hot and dense region in a nuclear collision emits particles and cools down. Emitted particles also interact with each other and create new particles which radiate out of the collision region. The particles are emitted from the hot and dense region with a certain momentum distribution.

Lets assume a thermal source with N particles. In a momentum interval $\vec{p}, \vec{p} + d\vec{p}$ there are $\frac{d^3n}{op^3}$ particles, where

$$d^3p = dp_x dp_y dp_z \tag{4.1}$$

In BRAHMS, we use the kinetic variables transverse momentum p_t, rapidity y and the angle ϕ. These variables are convenient to work with in a Lorentz frame, since the perpendicular variables p_t and ϕ are boost invariant and y is boost additive. One can transform into these coordinates through

$$d^3p = dp_x dp_y dp_z = \frac{\partial(p_x, p_y, p_z)}{\partial(p_t, y, \phi)} dp_t dy d\phi = J dp_t dy d\phi, \tag{4.2}$$

where J is the *Jacobi determinant.* This is done in appendix A and gives

$$dp^3 = E p_t dp_t dy d\phi \tag{4.3}$$

So now the number of particles in the small momentum interval can be written as

$$\frac{d^3n}{dp^3} = \frac{d^3n}{E p_t dp_t dy d\phi} \tag{4.4}$$

Also from appendix A we have

$$p_t dp_t = m_t dm_t \tag{4.5}$$

Assuming no explicit dependence on the azimuthal angle, ϕ, equation 4.4 can be integrated over 2π.

$$E\frac{d^3n}{dp^3} = \frac{d^2n}{2\pi m_t dm_t dy} \tag{4.6}$$

When normalizing the data in our spectra we take the number of events N_{ev} or rather the number of triggers N_{trig} into account together with other factors as explained in chapter 5. Therefore the spectra will have the form

$$\frac{d^2n}{2\pi N_{ev} m_t dm_t dy} \quad vs \quad mt - m$$

Let us go back to the thermal condition. In statistical mechanics, with the requirement that we have a grand canonical ensemble (GCE), exchange of heat and particles, the partition function Z can be defined as

$$Z = \sum_n \langle n|e^{(H-\mu\hat{N})/T}|n\rangle, \tag{4.7}$$

where n are the quantum states, H the Hamiltonian, μ the chemical potential, T the temperature and $\widehat{N}$ is the particle number operator. From the partition function we can derive the thermodynamical relations for pressure P, entropy S and particle number N per collision, not to be mistaken for N_{ev} mentioned earlier.

$$P = T\frac{\partial \ln Z}{\partial V} \tag{4.8}$$

$$N = T\frac{\partial \ln Z}{\partial \mu} \tag{4.9}$$

$$S = \frac{\partial (T\ln Z)}{\partial T} \tag{4.10}$$

Here V is the volume. The energy E is given by

$$E = -PV + TS + \mu N \tag{4.11}$$

Imagine a box filled with noninteracting bosons and fermions. It can be derived that

$$\ln Z = V\int \frac{d^3p}{(2\pi)^3}\ln(1 \pm e^{-(\epsilon-\mu)/T})^{\pm 1}, \tag{4.12}$$

from [1], where ϵ is the energy of the boson/fermion and $\pm$ is for fermions and bosons respectively. This expression leads to the average number of particles through 4.9 and N can be written as

$$N = V\int \frac{d^3p}{(2\pi)^3}\frac{1}{e^{(\epsilon-\mu)/T} \pm 1}. \tag{4.13}$$

This expression leads to the differential multiplicity

$$\frac{d^3n}{dp^3} = \frac{V}{(2\pi)^3}\frac{1}{e^{(\epsilon-\mu)/T} \pm 1}. \tag{4.14}$$

We consider collisions at $s_{NN} = \sqrt{200}$ GeV center of mass energies. At such high energies (much larger than the rest mass of hadrons) and due to conservation laws for charge, strangeness and baryon number we get pair production of particles, which results in a low chemical potential. This gives the result that $e^{(\epsilon-\mu)/T} \gg 1$, so the ± 1 factor in the denominator in expression 4.14 can be ignored. We therefore get

$$\frac{d^3n}{dp^3} = \frac{V}{(2\pi)^3} e^{-(\epsilon-\mu)/T}. \tag{4.15}$$

For a fixed value of μ we have

$$\frac{d^3n}{dp^3} \sim e^{-\epsilon/T}. \tag{4.16}$$

Writing this up in terms of the invariant cross section gives

$$E\frac{d^3n}{dp^3} \sim Ee^{-E/T}, \tag{4.17}$$

where E again is the energy of the particle. From appendix A the energy E is defined as $E = m_t coshy$.

We assume the fireball to be in local thermal equilibrium. In high-energy hadronic physics the p_t distribution is decreasing nearly exponentially. Two commonly used approximations are exponentials in transverse momentum p_t and transverse mass $m_t - m$. From the thermodynamical model we go to the exponential interpretations 4.18 and 4.19.

$$f(p_t) = E\frac{d^3n}{dp^3} = A_p e^{-p_t/T} \tag{4.18}$$

$$f(m_t - m) = E\frac{d^3n}{dp^3} = A_m e^{-(m_t-m)/T} \tag{4.19}$$

A is a normalization constant. A comparison of the two exponentials with thermal p_t distributions (Bose, Boltzmann, Fermi) of pions and protons separately done in ref [39], and showing the curves for the different calculations shows that an exponential in transverse mass best reflects the thermal distribution. In this thesis I will use both the p_t and $m_t - m$ approximations.

I shall now derive the functions used to fit the data, from the two exponentials. Remembering equations 4.6 and 4.5 we can integrate over transverse mass and momentum.

$$I_p = \frac{dn}{dy} = 2\pi A_p \int_0^\infty p_t e^{-p_t/T} dp_t \tag{4.20}$$

From integration by parts we get

$$I_p = \frac{dn}{dy} = 2\pi A_p T^2. \tag{4.21}$$

Similarly for the exponential in transverse mass

$$I_m = \frac{dn}{dy} = 2\pi A_m \int_m^\infty m_t e^{-(m_t-m)/T} dm_t. \tag{4.22}$$

Integration by parts gives

$$I_m = \frac{dn}{dy} = 2\pi A_m T(m+T) \tag{4.23}$$

We want to find the absolute yield, the number of particles inside this rapidity region. When fitting to data the two fit parameters we have are A and T the temperature (slope) of the spectra. Instead of A we want the factor $\frac{dn}{dy}$ as fit parameter. To find the number of particles we need to normalize the spectra, see chapter 5. To get the correct $\frac{dn}{dy}$ factor, A also needs to be normalized to the integrals over p_t and m_t. The factors that come out of the extrapolation from respectively approximation is divided out, so when the spectra are fitted the parameters T and A have the correct values. Or analytically

$$A_p = \frac{I_p}{2\pi T^2} \tag{4.24}$$

The fit function for p_t becomes

$$f(p_t) = \frac{I_p}{2\pi T^2} e^{-p_t/T}, \tag{4.25}$$

and similarly for $m_t - m$

$$A_m = \frac{I_m}{2\pi T(m+T)} \tag{4.26}$$

$$f(m_t - m) = \frac{I_m}{2\pi T(m+T)} e^{-(m_t-m)/T}. \tag{4.27}$$

The Boltzmann fit

As said above the exponential fits are merely approximations. Therefore the spectra in chapter 5 will also be fitted with a Boltzmann fit.

If we go back to the thermal model and make use of expression 4.17, with the change of adding a constant A and remembering that $E = m_t \cosh{(y)}$, so here $T^* = \frac{T}{\cosh{(y)}}$.

$$f(m_t - m) = E\frac{d^3n}{dp^3} = AEe^{-E/T} = Am_t \cosh{(y)} e^{-m_t/T^*} \tag{4.28}$$

From equation 4.6 we now have

$$f(m_t - m) = E\frac{d^3n}{dp^3} = \frac{d^2n}{2\pi m_t dm_t dy} = AEe^{-E/T} = Am_t \cosh{(y)} e^{-m_t/T^*} \tag{4.29}$$

By integration over m_t we find $\frac{dn}{dy}$

$$I = \frac{dn}{dy} = 2\pi A \cosh{(y)} \int_m^\infty m_t^2 e^{-m_t/T^*} dm_t = 2\pi A T e^{-m/T^*} (m^2 + 2mT^* + 2T^{*2}) \tag{4.30}$$

Integration 4.30 is solved in appendix B. As described above we fit the spectra with two parameters, the yield A and the temperature T^*. Therefore we want to normalize the spectra in such way that we get the number of particles. We normalize the integral over m_t by dividing out the factors from the extrapolation, so that parameter A becomes $\frac{dn}{dy}$ in the fit. Analytically written as

$$A = \frac{I}{2\pi T e^{-m/T^*} (m^2 + 2mT^* + 2T^{*2})} \tag{4.31}$$

The final Boltzmann fit function becomes

$$f(m_t - m) = \frac{Im_t}{2\pi T^*(m^2 + 2mT^* + 2T^{*2})} * e^{-(m_t-m)/T^*} \tag{4.32}$$

and for p_t we have $m_t = \sqrt{p_t^2 + m^2}$ so the p_t fit function becomes

$$f(p_t) = \frac{I\sqrt{p_t^2 + m^2}}{2\pi T^*(m^2 + 2mT^* + 2T^{*2})} * e^{-\frac{\sqrt{p_t^2+m^2}-m}{T^*}}. \tag{4.33}$$

4.2 The Blast Wave

In the blast wave model the colliding nuclei are exploding fireballs. In these explosions, blast waves of mesons and nucleons are produced. The major difference between the two models is that all motion in the thermal model is due to thermal energy. In the blast wave model there is also a motion added from the blast (pressure), so here the available energy is translational energy of the blast and thermal motion of the particles in the exploding matter.

An example is the firecracker, which when lit explodes due to the high pressure created by the energy release of the burning gun powder. In our example we create extremely hot and dense zones by colliding nuclei at high energies. The blast wave is a result of the incompressibility of nuclear matter and of the frequent collisions between particles moving rapidly in the hot and dense zone. Particles at the surface can move freely outward, but when moving inward they will always collide with particles moving outward from the hot and dense inside. Thus particles on the surface will be moving outward. The anisotropy in the particles environment gives rise to an anisotropy in their velocity distribution. The particles acquire a net flow velocity β, which we call the blast wave. As the center layer of the particles move outward they fill up more space and the density decreases. The next layer of particles now feel an anisotropy in their environment and begin to move outward.

The paper [40] quantitatively describes the phenomenon above in hydrodynamical terms, within the limit of very frequent collisions. By converting internal thermal energy into work through a pressure gradient ∇P a macroscopic flow velocity β results. The system is isolated and therefore adiabatic and the force ∇P is reversible, so entropy is conserved during the expansion. While the system expands in coordinate space, this expansion is compensated by the concentration of velocity into a narrower momentum space. This concentration of velocity is due to the cooling of matter required to release energy for the macroscopic flow. Further energy added to the blast may be provided by the elastic forces between the nucleons. Their compressional energy is released as the density drops. Another energy factor is the reabsorption of pions and deexcitation of nucleon resonances as the temperature drops.

The transformation of thermal and compressional energy into a blast-wave flow continues as long as there are sufficiently frequent collisions. Eventually the density is too low and the collisions come to an end. The particles retain their momenta until they reach the detectors. The final momentum distribution is characterized by a mean expansion velocity β. The two main features of the blast wave is the peaking of the velocity around the mean velocity in contrast to the thermalized model, where the distribution peaks near the slowest particles in the fireball frame, (see thermal Boltzmann distribution) [1]. The second feature is the reduction of intrinsic excitation due to the cooling accompanying the expansion. This text follows [38] where more information on the subject can be found.

In chapter 5 the flow velocity will be obtained from the transverse mass spectra. Expression 2.3 will be used as fit function. This function requires local thermal equilibrium and it is based on hydrodynamical features [41]. The thermodynamical variables are related to each other through the equation of state, while their space-time evolution is determined by relativistic hydrodynamics. The idea is to begin from hydrodynamical equations with no transport effects like viscosity and heat conduction. In reference [41] global conservation laws are derived from local ones by integration of the local laws. From these integrals different parameters (temperature and flow at the fireball surface) can be deduced.

The fit function for transverse flow can be deduced from [42]

$$
\begin{aligned}
E\frac{d^3n}{dp^3} &= \frac{g}{(2\pi)^2}\int_{-\eta_{max}}^{\eta_{max}} d\zeta\left[m_t\cosh y\frac{\partial z}{\partial\zeta} - m_t\sinh y\frac{\partial t}{\partial\zeta}\right] \\
&\quad \int_0^R rdr\exp\Big(-\frac{m_t\cosh\rho\cosh(y-\eta)-\mu}{T}\Big)I_0\Big(\frac{p_t\sinh\rho}{T}\Big),
\end{aligned} \tag{4.34}
$$

where the azimuthal symmetry of ϕ has been used to integrate over ϕ, making use of the modified Bessel function $I_0(z) = (2\pi)^{-1}\int_0^{2\pi} e^{z\cos\phi}d\phi$. In equation 4.34 $E\frac{d^3n}{dp^3}$ is the invariant cross section and ζ, which has the range $-\eta_{max} \leq \zeta \leq \eta_{max}$ is the pseudo-rapidity term and runs in longitudinal directions. z and t are the z direction and time, where the time is invoked due to the large dilation in longitudinal direction. The transverse momentum is boost invariant and $\rho = \tanh^{-1}\beta$ is the boost angle, where β is the transverse flow velocity. Finally, μ is the chemical potential.

The transverse mass spectrum can be integrated with the help from the modified Bessel function $K_1(z) = \int_0^\infty \cosh y e^{-\cosh y}dy$ and by using 4.6 we get from 4.34

$$
\begin{aligned}
\frac{dn}{m_t dm_t} &= \frac{g}{\pi}m_t\int_{-\eta_{max}}^{\eta_{max}} d\zeta\left[\cosh\eta\frac{\partial z}{\partial\zeta} - \sinh\eta\frac{\partial t}{\partial\zeta}\right]\int_0^R rdrK_1\Big(\frac{m_t\cosh\rho}{T}\Big)I_0\Big(\frac{p_t\sinh\rho}{T}\Big) \\
&= \frac{2g}{\pi}m_t Z_{\tilde{t}}\int_0^R rdrK_1\Big(\frac{m_t\cosh\rho}{T}\Big)I_0\Big(\frac{p_t\sinh\rho}{T}\Big)
\end{aligned} \tag{4.35}
$$

R is the radius of the fireball$R \propto A^{1/3}$, where A is the number of nucleons in the nuclei. From here we get the final fit function used in chapter 5, where we have

$$
\frac{dN}{m_t dm_t} \propto \int_0^R rdrm_t I_0\Big(\frac{p_t\sinh\rho}{T_0}\Big)K_1\Big(\frac{m_t\cosh\rho}{T_0}\Big). \tag{4.36}
$$

The transverse flow profile is determined by

$$
\beta = \beta_s\left(\frac{r}{R}\right)^\alpha, \tag{4.37}
$$

where β_s is the transverse flow at the surface of the fireball and α describes the evolution of the flow velocity.

Chapter 5

Experimental Analysis

This chapter will explain how the spectra for the Mid Rapidity Spectrometer (MRS) are constructed. The analysis is made in two parallel steps. We do simulations to find the characteristics of the detector (geometrical acceptance), and data clean up, where we select which data to analyze and remove background etc. Finally we correct the data for acceptance found in the simulations. It is done for vertexes between ±15 cm in vertex bins of 5 cm width. As an example, pions at 90° are being used.

1. The "simulated data" analysis. Simulated data are generated to make acceptance maps.

2. The "real data" analysis. Cuts are applied on events and tracks to clean up the data and particle identification (PID) is done.

3. The acceptances found in the simulated data analysis are then applied to the real data to correct for the geometry and instrumentation of the detectors, so that data from different settings, efficiencies of the detector and vertex positions become comparable. Corrections for decays, absorption and secondaries are also applied.

5.1 Simulated Data Analysis

To get the simulated data we use a program called BRAG, which stands for BRAHMS Geant. Geant is a simulation library that simulates propagation of particles and interaction of these particles with materials. BRAG is a special version of geant which includes a description of the BRAHMS experiment.

5.1.1 BRAG Analysis Tool

In the BRAG analysis program single particles are thrown into the detector. In this analysis I a flat distribution for the vertex, p, θ and ϕ ranges was used. For this to be accurate, the ranges have to be split up in small bins, since the real distributions most likely are not flat, but seem flat when looked upon in these small bins. The vertex distribution ranges from ±15 cm and is split up in 6 bins, each 5 cm wide. The momentum range goes from 0.05 GeV/c to 4.0 GeV/c and is split up in bins of 50 MeV/c.

The idea is to create a purely geometrical acceptance map described in rapidity y and transverse momentum p_t or transverse mass m_t. Therefore, are all physical features except coulomb scattering and energy loss due to the particles traveling through medium are turned off in the simulation. Furthermore the only object stopping the particles is D5. Interactions in the beam pipe, multiplicity arrays etc are turned off.

The acceptance is found by comparing thrown particles with detected particles. For the particles to be detected it is required that they have traveled through the whole detector. This means that the particles must leave a track in TPM1 and TPM2. They are not allowed to hit the iron in D5 and they must be detected in the TOFW. The acceptance map is found by, for each bin in p_t and y dividing the number of detected particles that make it to TOFW by particles thrown.

Figure 5.1 shows an example of a pion simulation, and in figure 5.2 an example of an acceptance map is shown.

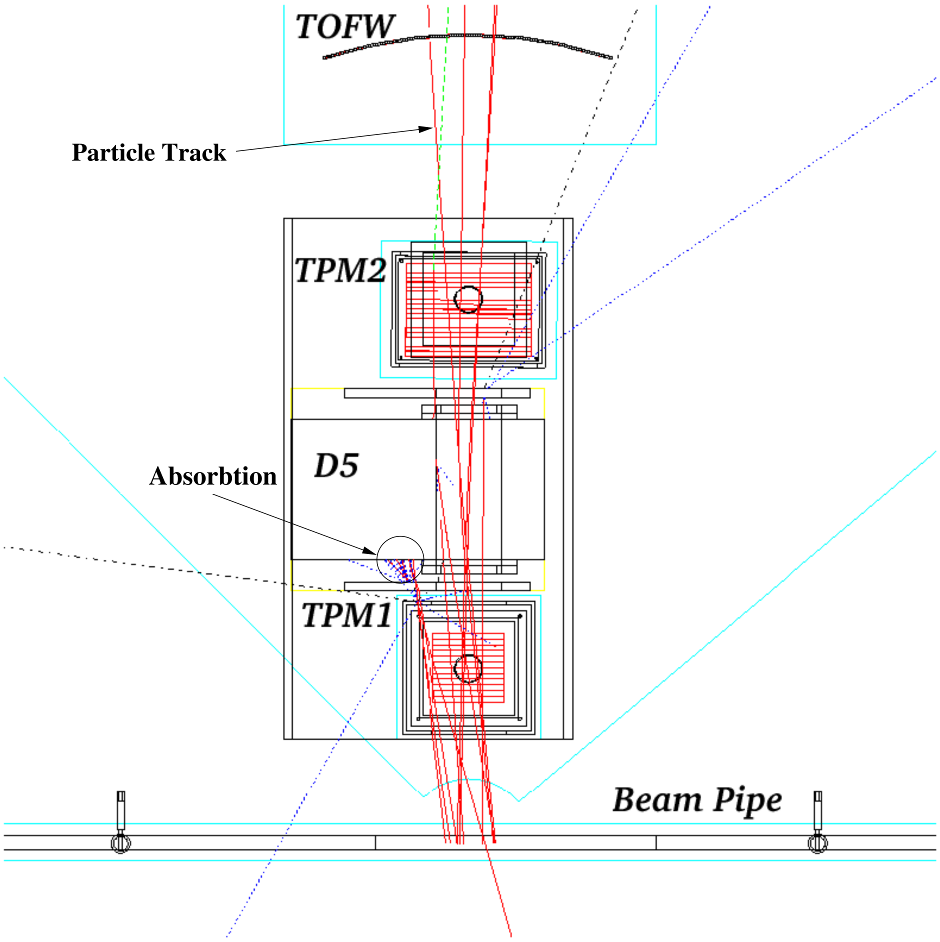

Figure 5.1: A BRAG simulation of 10 π^+ thrown into the MRS detector with a field setting of 2.16 kGauss seen from above. The particles have p between 0.1 and 2.0 GeV, θ between 80° and 100° and ϕ between ±2.0°. The red lines show the particle tracks through the detector. To the left of the D5 magnet gap, pions hitting the iron may be seen. For this event the overall acceptance is thus 3/10.

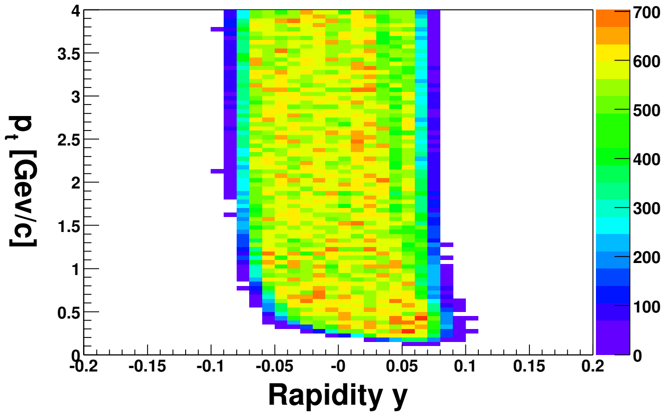

Figure 5.2: The colored areas show the detector acceptance of the MRS. The current example shows the p_t and y acceptance for particles positively charged at 90° and a magnetic field of 2.13 Gauss. The vertex runs between 0 and 5 cm.

5.2 Real Data Selection

The different modules in the detector detect charged particles and we are only interested in particles originating from the collision. Therefore as a first step the data must be cleaned up. Background radiation, particles originating from the beam pipe etc have to be removed from the sample. This is done in a step we call particle identification (PID) selection. Not only do we sort out the right particles, but we also determine their identity.

The first step is to make an event selection. We do not accept events outside our vertex limit, in this case ±15 cm. Further requirements for the events to be good are that they are trigger 6 events and that the vertex is determined from either two big tubes with one in each BB array or two small tubes with one in each BB array. A trigger 6 event is an event that require the vertex to be between -25 and +20 cm and a multiplicity large enough for the energy threshold in the multiplicity array to be passed. We also check that the beam-beam vertex and the ZDC vertex are no more than 25 cm away from each other. We also impose a 5% centrality cut, so only the most 5% central events are chosen.

Once good events have been selected, the tracks from TPM1 and TPM2 have to be combined. By "swimming" tracks from TPM2 through D5 and matching them to tracks in TPM1 global tracks can be found. Tracks are then given the status OK.

Further requirements are that the particles hit the TOFW and generate signals signaling where and when the hits occurred.

5.2.1 Particle Identification (PID)

In the PID step, not only is the PID determined, but some bad tracks are also being expelled. By extrapolating TPM1 tracks back to the vertex and comparing with the beam-beam vertex, particles not originating from vertex can be sorted out. In the y direction the distribution is a Gaussian and tracks diverting more than $3^*\sigma$ are not accepted. The y direction is defined as the direction between "earth and sky", perpendicular to the x direction, which points in the same direction as MRS set to 90°. The z direction is the same as the direction of the beam, positive toward FS. If the hit slat in the TOFW is not the same as the slat pointed to by extrapolation of TPM2, the track is not accepted. The same goes for hits and extrapolations in y differing more than 3.0 cm from each other.

By subtracting the TOF mass squared from mass squared a Gaussian distribution is found. The PID is done by comparing the mass squared measured from TOF and mass squared from table, with the restraint that the masses squared do not differ more than 3*σ from the ideal mass squared.

$$m^2_{TOFW} - m^2 < 3\sigma \tag{5.1}$$

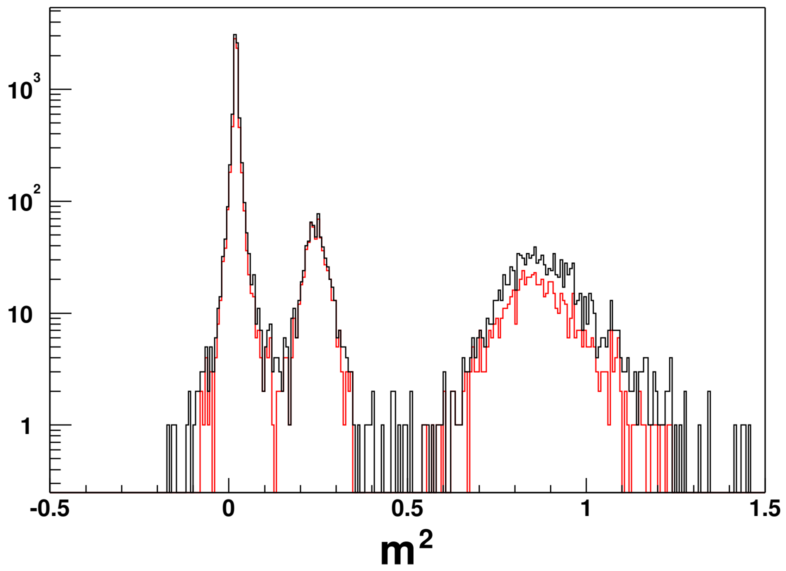

Figure 5.3: The black histogram shows all particles in mass squared picked up by TOFW and the red line shows particles that are within the different requirements for PID, mentioned in the text. The setting is 90 degrees and D5 magnetic field is -2.12 kGauss. The reduction in protons is due to the correction for protons originating from the beam pipe (knockout by pions).

5.2.2 Data Corrections

The tracks collected must be corrected for efficiencies, absorption and decays. The efficiency correction is made by using runs with no field and extrapolating hits from TOFW back to vertex. When there is no field the particle track is straight and the position of the track in TPM1 is known. Then we look in TPM1 and see if we find a track. The reason for only looking at TPM1 is that this is the major contributor to the efficiency correction, since it is placed closest to the vertex and thereby has the most tracks. For 90° we find a efficiency of 92% and for 40° we have a decreasing efficiency depending on the number of clusters in the TPC,

$$E(x) = 0.98 - 0.000109x \tag{5.2}$$

where E is the efficiency and x the number of clusters in 5.2. The decay correction is calculated with the help of BRAG simulations. There are different steps for different particles. Protons do not decay, but multiple scattering has to be accounted for. Two simulations are done, one with only energy loss turned on and one with energy loss and multiple scattering turned on. The two simulations goes through digitization of hits, reconstruction of track and PID. Digitization is a way to simulate the response of the detector to simulated "ideal" particles. This is needed since a pure comparison of the output of the two simulations does not take into account the detector resolution. Further, the simulated tracks are checked in the same way as real data with slats comparison and position matching within 3*σ, see section 5.2.1. Next, the ratio "multiple scattering on" versus "multiple scattering off" is found and a fit function is found 5.3

$$f(p) = A - Be^{-Cp}, \tag{5.3}$$

where p is the momentum of the incoming particle. For kaons, pions and anti-protons the procedures are the same except for the additional simulations of decay processes. Here, one simulation including energy loss is made and one including energy loss, multiple scattering and decay. To check for differences the calculations are made for settings 90° and 40°. The results can be found in table 5.1.

particle	**setting\parameter**	**A**	**B**	**C**
$\pi^{\pm}$	90°	0.9856	0.4371	2.671
	40°	0.9903	0.4394	2.629
$K^{\pm}$	90°	0.84	1.069	1.395
	40°	0.8392	1.073	1.406
p	90°	0.997	26.78	12.57
	40°	0.9969	33.46	13.64

Table 5.1: The different parameter values for the decay function for pions, kaons and protons, with multiple scattering included (equation 5.3).

For anti-protons there is also a absorption factor from the beam pipe, that needs to be accounted for. The absorption function has the same parameters and shape as the decay function and the values can be found in table 5.2.

setting\parameter	**A**	**B**	**C**
90°	0.9828	0.1623	4.508
40°	0.9797	0.1714	3.937

Table 5.2: The parameter values of the absorption function for anti-protons crossing the beam pipe. Decay and multiple scattering is included.

Finally all the corrections are applied to the data. This is done by dividing real data with the correction values and the results are plotted in p_t versus y and $m_t - m$ versus y histograms.

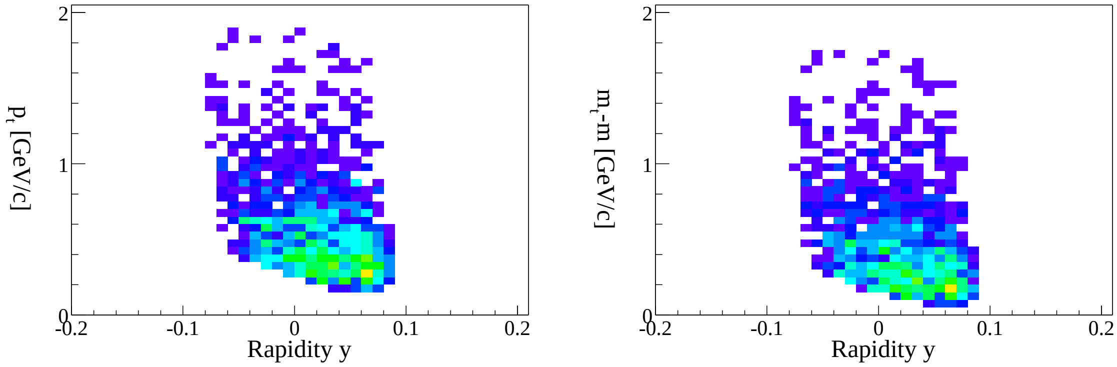

(a) p_t (b) $m_t - m$

Figure 5.4: Transverse momentum p_t and mass $m_t - m$ versus rapidity y for π^+ corrected for multiple scattering, efficiencies and decays. The vertex range is the same as for figure 5.2.

5.2.3 Acceptance Correction of Data

The data have so far been selected in a way that all particles originate from the vertex. Corrections for efficiencies, multiple scattering, absorption and decays have been taken into account. The next step is to merge the data and the acceptance maps. Before acceptance cuts, data and acceptance maps look as in figure 5.2.3.

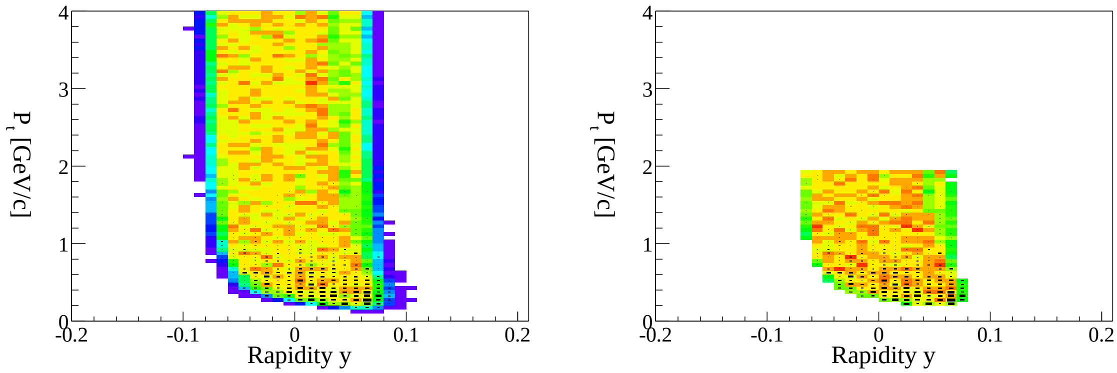

(a) The whole map. (b) The map after cuts has been provided.

Figure 5.5: Left: Acceptance map from figure 5.2 overlapped by p_t data (black squares) from figure 5.4. Right: The same values, but with acceptance and PID cut for pions.

Only acceptances with no ambiguities are wanted. By taking an acceptance value, $A_{mean} = 0.004 * \sin\theta$, near the mean acceptance and defining a lower and a higher limit, $A_{low} = 0.5 * A_{mean}$ and $A_{high} = 1.5 * A_{mean}$ an acceptance range is obtained. All data outside this range are rejected to avoid edge effects. Once all data outside the acceptance range, i.e the edges have been trimmed, has been removed, we apply the numerical acceptance correction to the data. This is done in a bin by bin division of data with acceptance in the different p_t and y bins of the 2d histograms.

5.3 Estimation of the Yields

The first step in the analysis of the yields is to divide the merged data by p_t, since the relation between p_t spectra and yields goes through equation 5.4, also see chapter 4.

$$Ae^{-p_t/T} = \frac{1}{N_{ev}} \frac{d^2N}{dy dp_t} \frac{1}{p_t} \tag{5.4}$$

The next step is to normalize the data to a unit of rapidity and number of events. This includes dividing out the bin width in p_t and y for the p_t vs y histograms and scaling with the number of events in the different vertex ranges.

Finally, the weighted mean of the spectrum at a given p_t over the selected rapidity range y is calculated. For fixed p_t, multiply the acceptance with the data and sum up over the different rapidity bins in the selected range. Then for the same p_t bin sum up the acceptance for the different rapidities and divide the two. In other words,

$$M_w = \frac{\sum_i a_i d_i}{\sum_i a_i} \tag{5.5}$$

where, M_w is the weighted mean, a is the acceptance value and d is the data value. The index i is the number of rapidity bins. This is individually done for the different p_t bins and is projected to create the spectra, (figure 5.6). To avoid dividing by zero, for bins with acceptance sum equal to zero, the weighted mean is set to zero. We can now fit an exponential

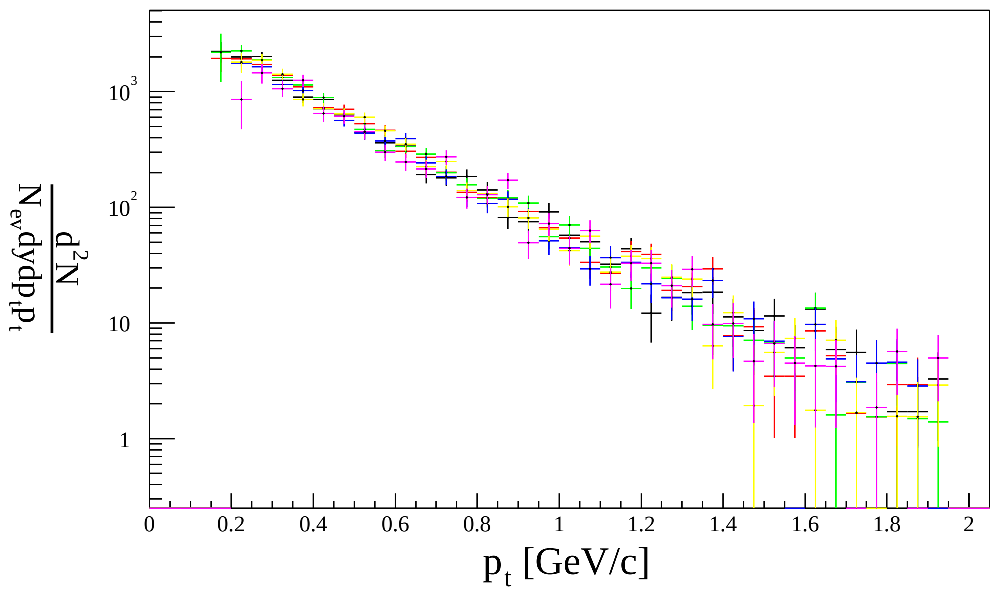

Figure 5.6: Spectra from a projection of p_t for $-0.03 < y < 0.03$. Shown is the comparison of the different normalized p_t spectra for 6 different vertex bins ($-15cm < vtx < 15cm$).

function to the found spectra. The function used is 5.6, also see chapter 4. This is not the final exponential fit-function, but gives us a hint to check that we are on the right track.

$$f(p_t) = N/T^2 * e^{-p_t/T} \tag{5.6}$$

Where N stands for number of particles (Yields) and T for temperature. The results can be viewed in figure 5.7.

The 2d histograms for the different vertexes are summed up. The summation is weighted due to different statistics in the different vertex ranges. The total weighted mean of the 2d histograms over the different vertexes, y and p_t is calculated in the same way as for the weighted spectra 5.5, with the difference that here the same bins for different y versus p_t histograms are summed up. The event weight factor is included by multiplying the number of events for the different vertexes, measured by the beam-beam counters,

$$M_w = \frac{\sum_i a_{ijk} d_{ijk} N_{evi}}{\sum a_{ijk} N_{evi}}, \tag{5.7}$$

where j, k are the bin numbers and i the subscript for the different vertex ranges. This new 2d histogram is projected and fitted as described in the section about projection and fits above. The result is shown in figure 5.8

The 2d histograms summed over the different vertex ranges are collected for the different settings (magnetic fields and detector angle θ) in the same rapidity range. By including data from all settings the statistics become good enough to choose a narrow rapidity bin and inside this bin project the p_t or m_t to create a spectrum, (figure 5.9). While doing this the individual histograms are averaged according to equation 5.5. Spectra with counts in less than five p_t bins are not included. By finding the p_t with the maximum number of counts and removing all particles with p_t lower than this value, particles at the low p_t edge of the acceptance are disregarded. The kept spectra are merged and averaged bin by bin according to the least squares method.

$$A_{bin} = \frac{\sum_i \frac{d_i}{\sigma_i}}{\sum \frac{1}{\sigma_i}} \tag{5.8}$$

Here i are the different spectra, σ_i are the individual spectrum errors for the different points, d_i are the data points and A_{bin} the averaged bin values.

The beam is unpolarized and we average over many events. We assume a uniform distribution over ϕ, therefore the spectra are divided by 2π (chapter 4) and exponentially fitted. p_t spectra are fitted with equation 5.9 and m_t spectra are fitted with function 5.10.

$$f(p_t) = \frac{N}{2\pi T^2} e^{-p_t/T} \tag{5.9}$$

$$f(m_t - m) = \frac{N}{2\pi(m+T)T} e^{-(m_t-m)/T} \tag{5.10}$$

N is the number of particles, the yield, and m the particle mass. The fits are extrapolated and integrated. The temperature T can be deduced from the slope of the fit and the yield from the integral of the fit. The final spectra and their corresponding yields for $y = 0$ are shown in figures 5.10 and 5.11.

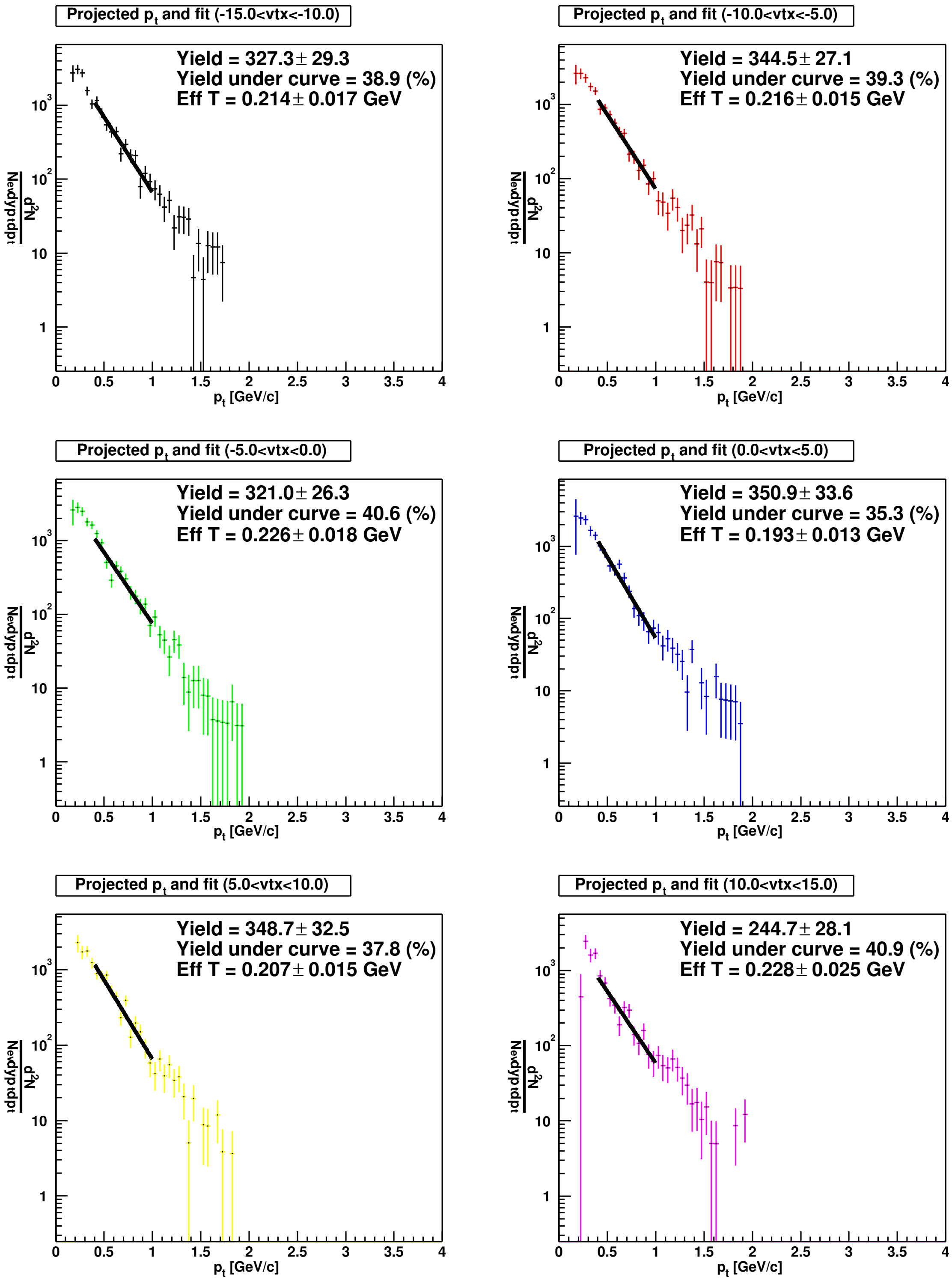

Figure 5.7: Exponential fits to the spectra. The fits are made by function 5.6. Here all six vertex ranges are shown. The setting is the same as before and the particles discussed are π^+.

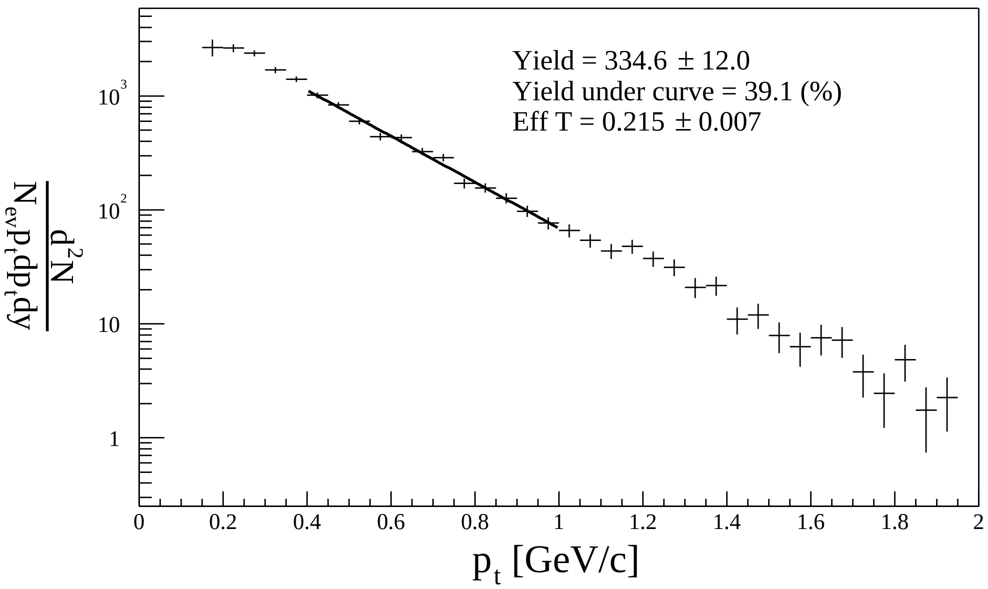

Figure 5.8: The weighted mean of spectra for the different vertex ranges. The same particles and settings as for the rest of the analysis outline are being used.

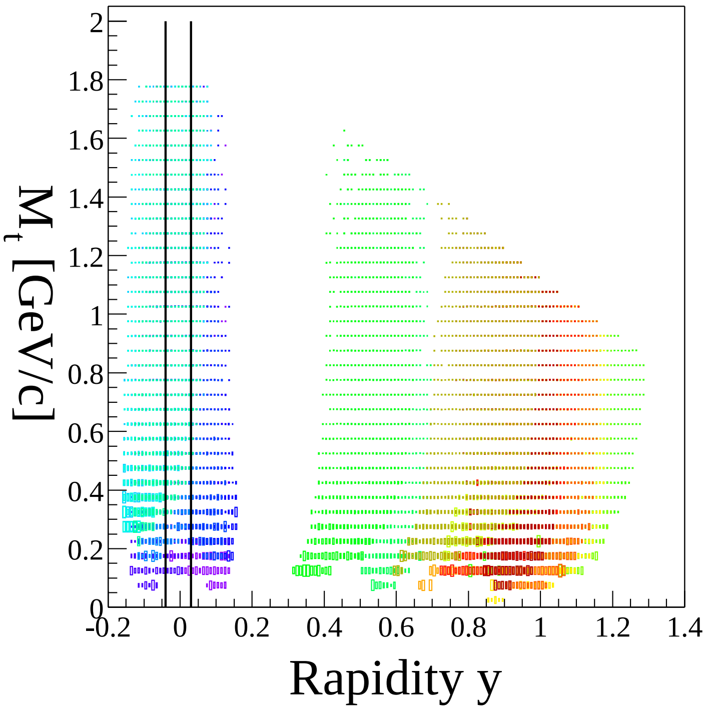

Figure 5.9: The phase space coverage of the data from MRS used in this thesis. The two lines show the dy cuts in rapidity for the midrapidity region. The slice is projected on the p_t axis to create p_t spectra.

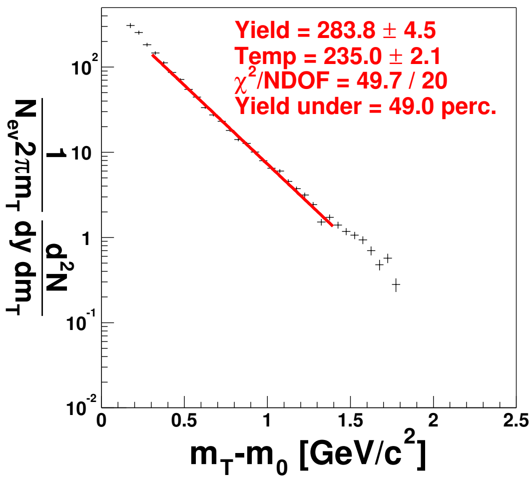

(a) Spectrum for π^+ in $m_t - m$.

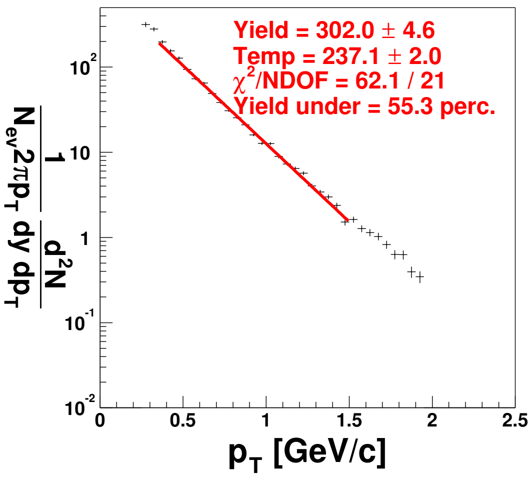

(b) Spectrum for π^+ in p_t.

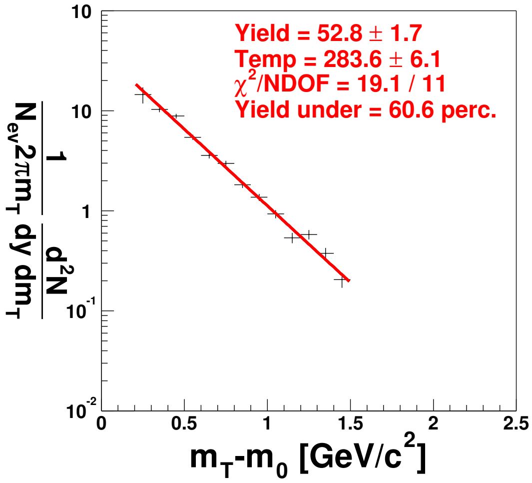

(c) Spectrum for k^+ in $m_t - m$.

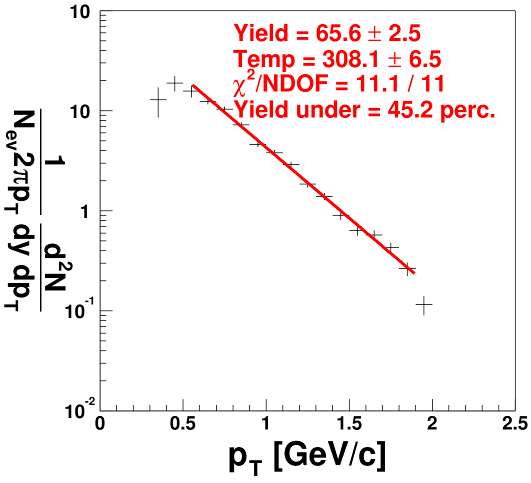

(d) Spectrum for k^+ in p_t.

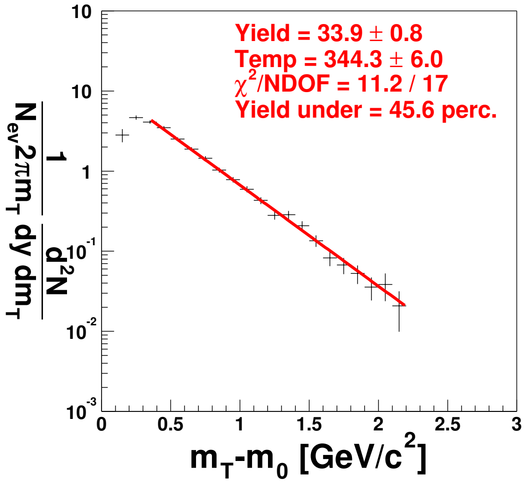

(e) Spectrum for p in $m_t - m$.

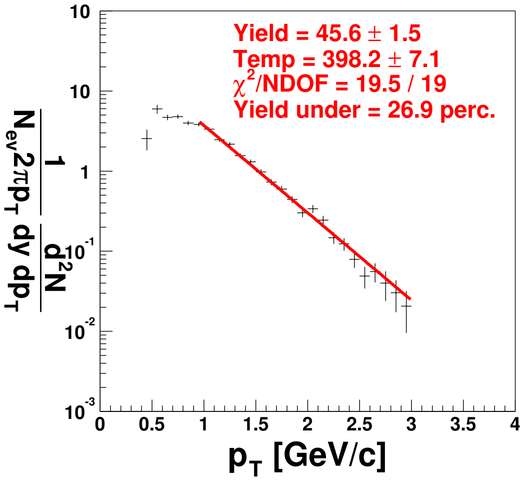

(f) Spectrum for p in p_t.

Figure 5.10: The spectra and corresponding fits for positive particles in the rapidity range $y = \pm 0.03$.

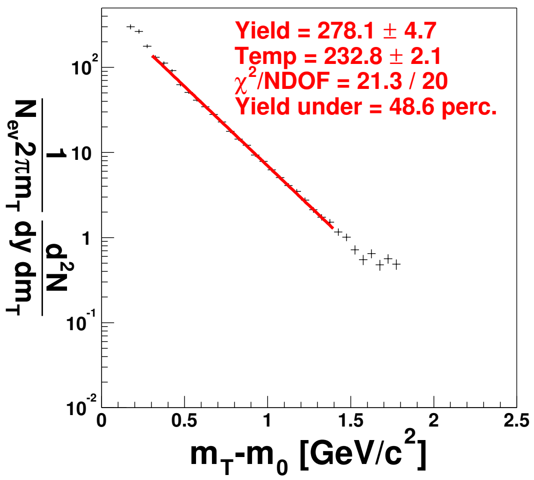

(a) Spectrum for π^- in $m_t - m$.

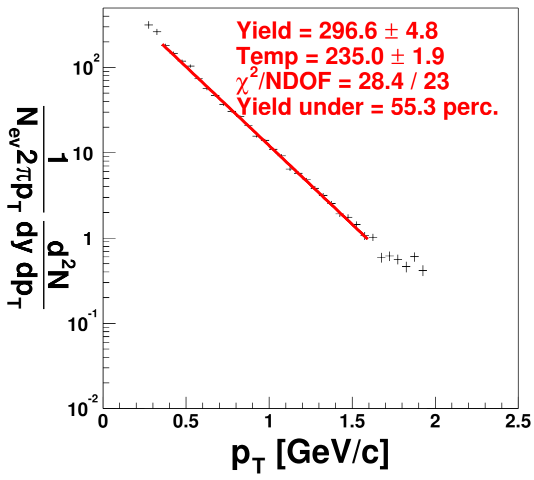

(b) Spectrum for π^- in p_t.

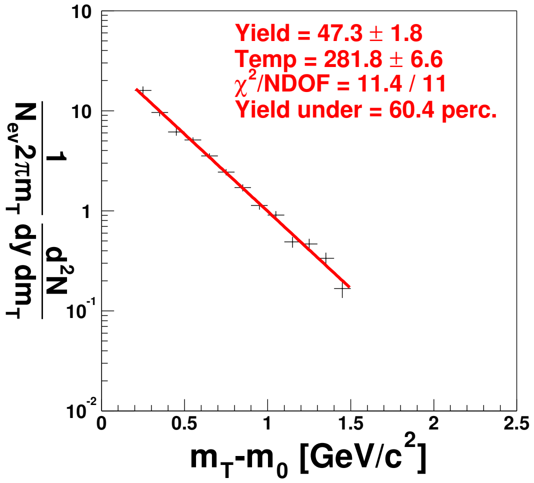

(c) Spectrum for k^- in $m_t - m$.

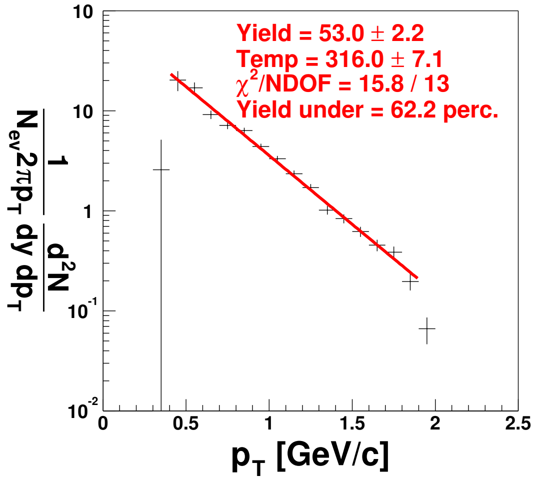

(d) Spectrum for k^- in p_t.

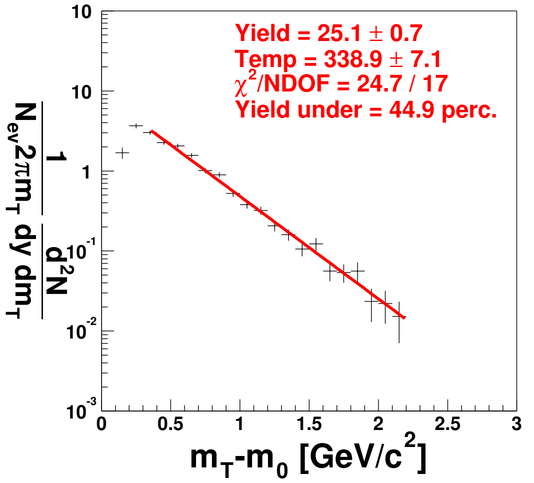

(e) Spectrum for $\bar{p}$ in $m_t - m$.

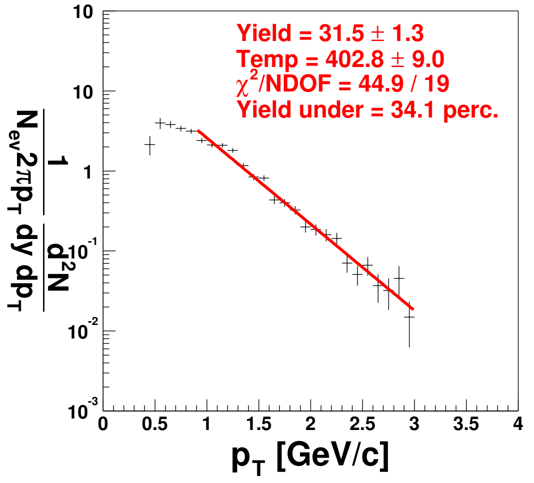

(f) Spectrum for $\bar{p}$ in p_t.

Figure 5.11: The spectra and corresponding fits for negative particles in the rapidity range $y = \pm 0.03$.

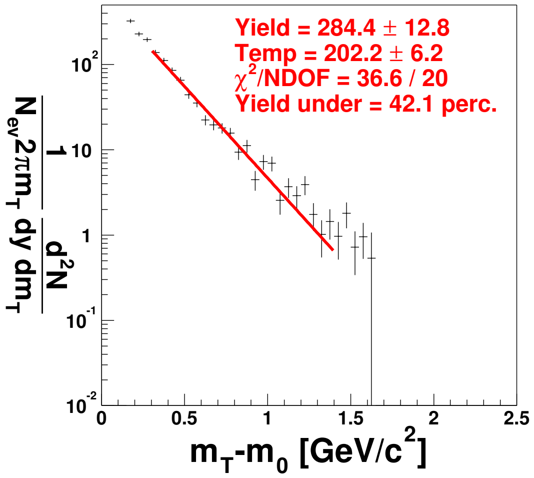

(a) Spectrum for π^+ in $m_t - m$.

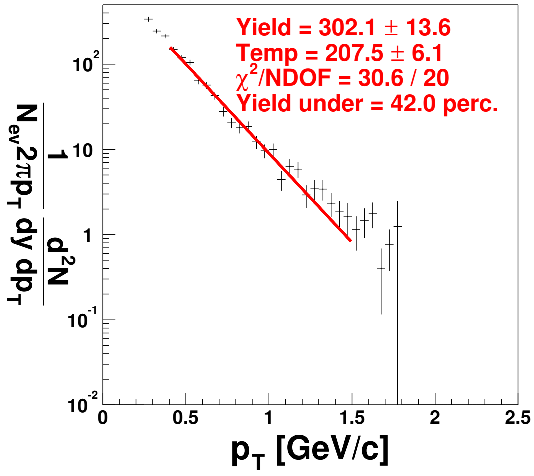

(b) Spectrum for π^+ in p_t.

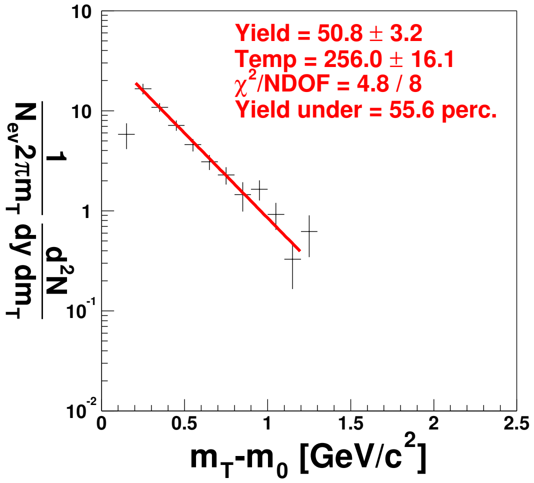

(c) Spectrum for k^+ in $m_t - m$.

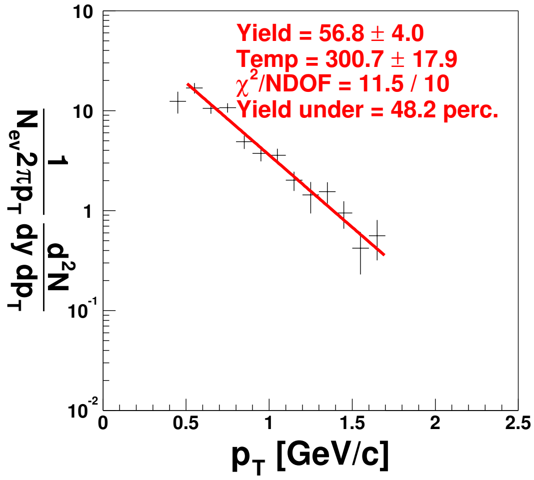

(d) Spectrum for k^+ in p_t.

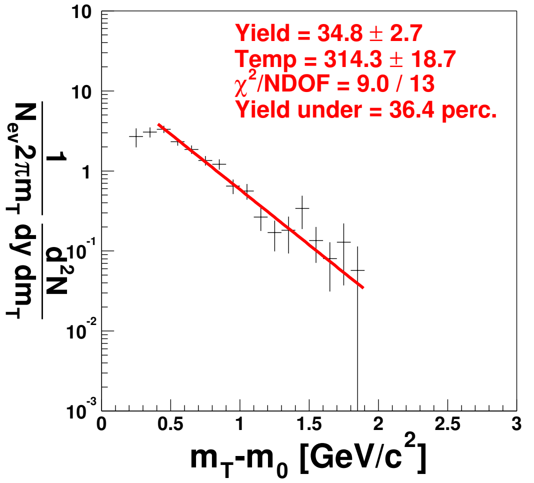

(e) Spectrum for p in $m_t - m$.

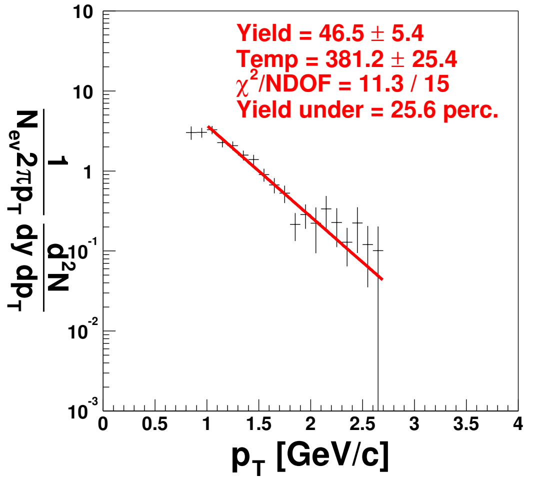

(f) Spectrum for p in p_t.

Figure 5.12: The spectra and corresponding fits for positive particles in the rapidity range $y = 0.45 \pm 0.03$.

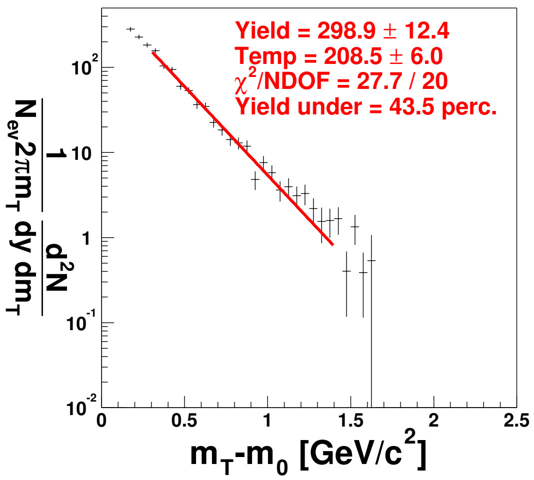

(a) Spectrum for π^- in $m_t - m$.

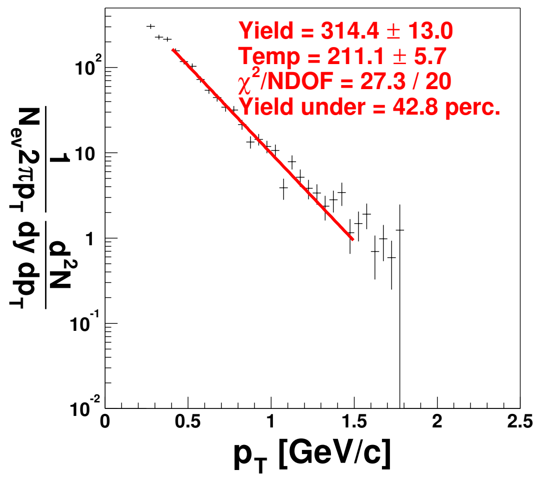

(b) Spectrum for π^- in p_t.

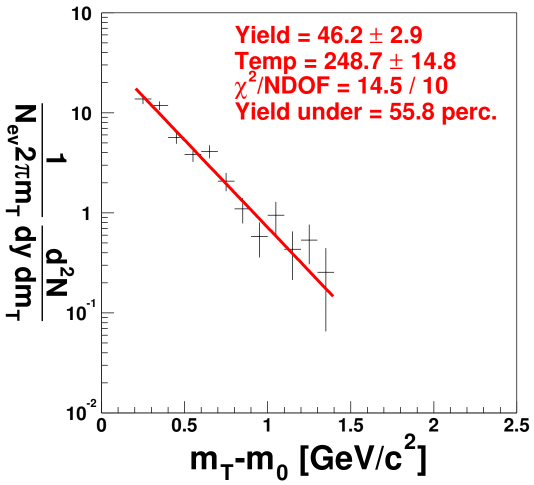

(c) Spectrum for k^- in $m_t - m$.

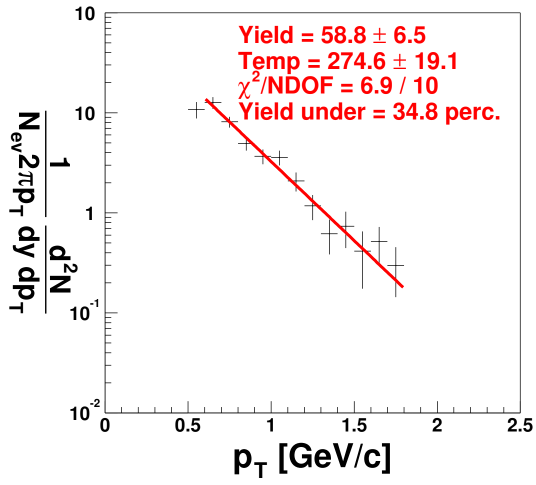

(d) Spectrum for k^- in p_t.

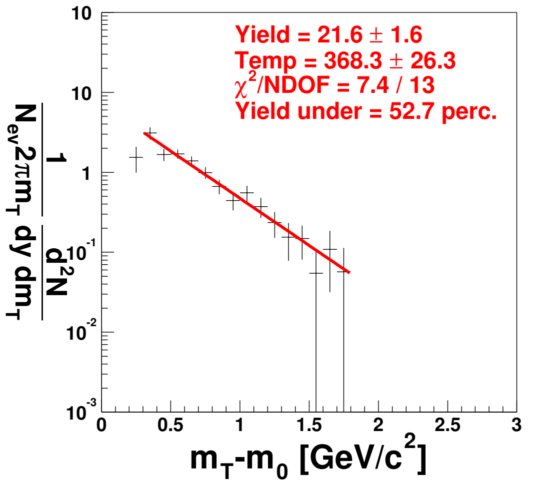

(e) Spectrum for $\bar{p}$ in $m_t - m$.

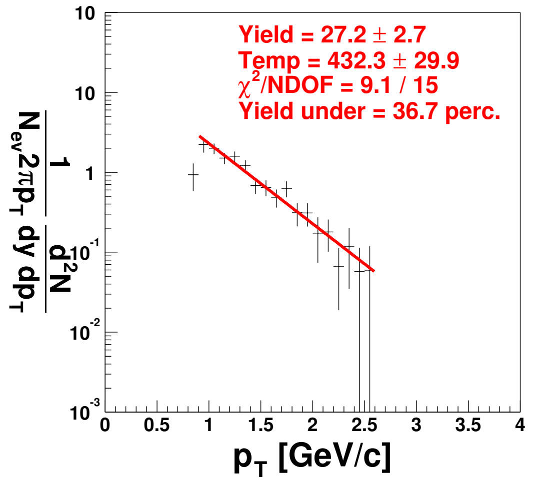

(f) Spectrum for $\bar{p}$ in p_t.

Figure 5.13: The spectra and corresponding fits for negative particles in the rapidity range $y = 0.45 \pm 0.03$.

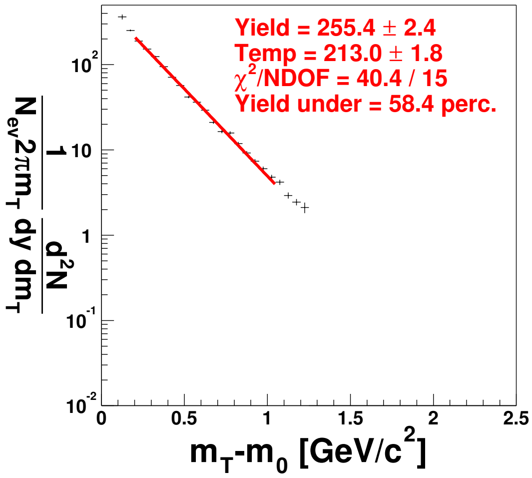

(a) Spectrum for π^+ in $m_t - m$.

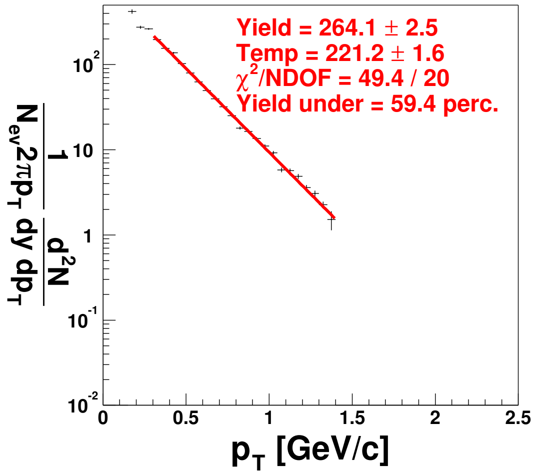

(b) Spectrum for π^+ in p_t.

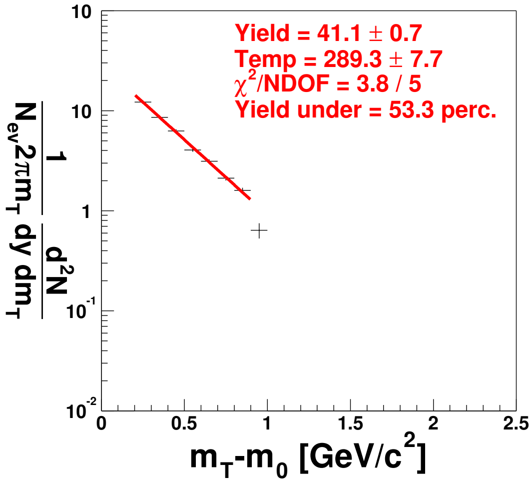

(c) Spectrum for k^+ in $m_t - m$.

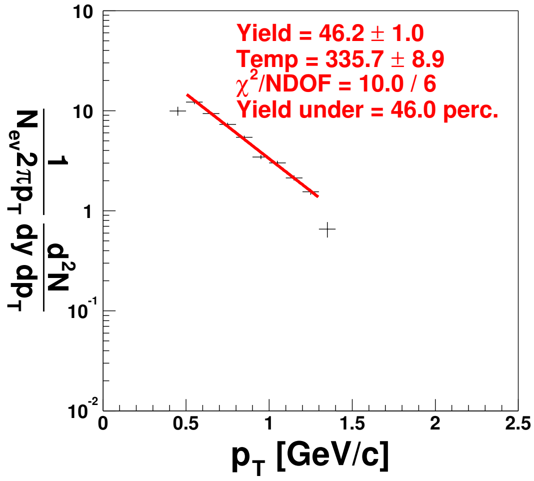

(d) Spectrum for k^+ in p_t.

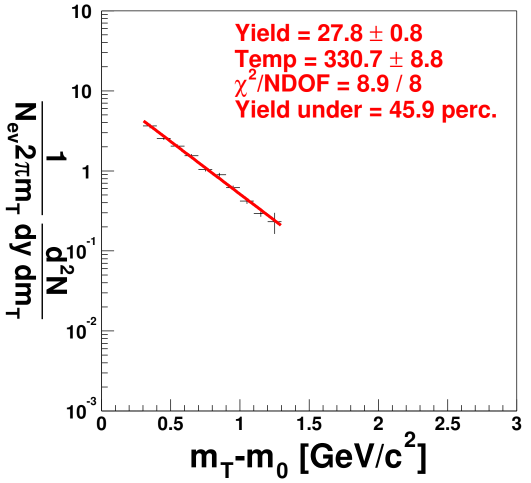

(e) Spectrum for p in $m_t - m$.

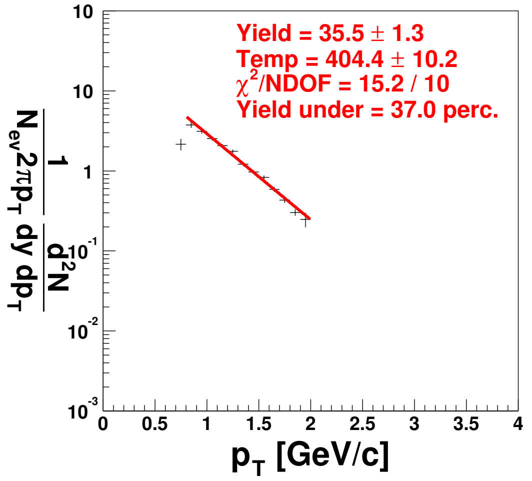

(f) Spectrum for p in p_t.

Figure 5.14: The spectra and corresponding fits for positive particles in the rapidity range $y = 0.9 \pm 0.03$.

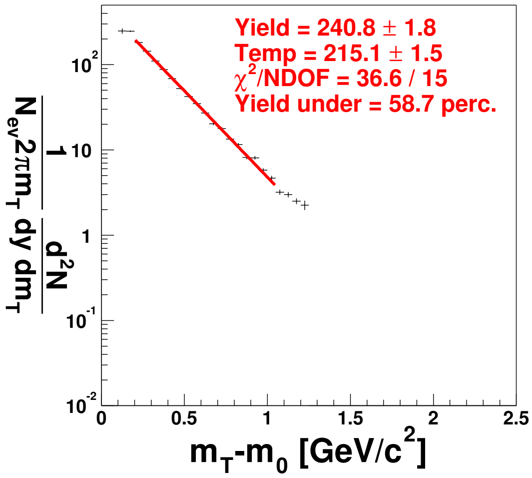

(a) Spectrum for π^- in $m_t - m$.

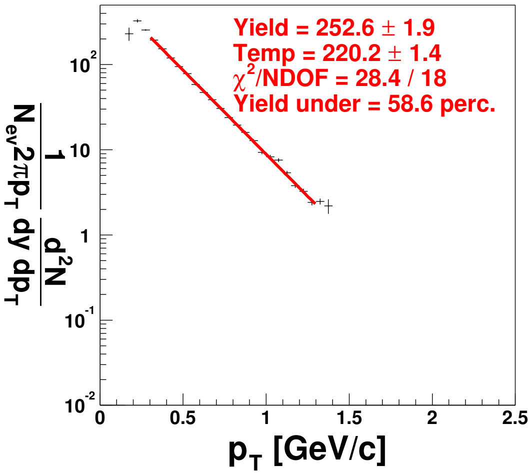

(b) Spectrum for π^- in p_t.

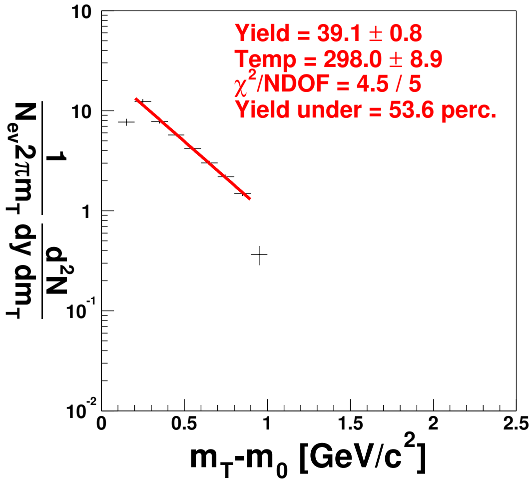

(c) Spectrum for k^- in $m_t - m$.

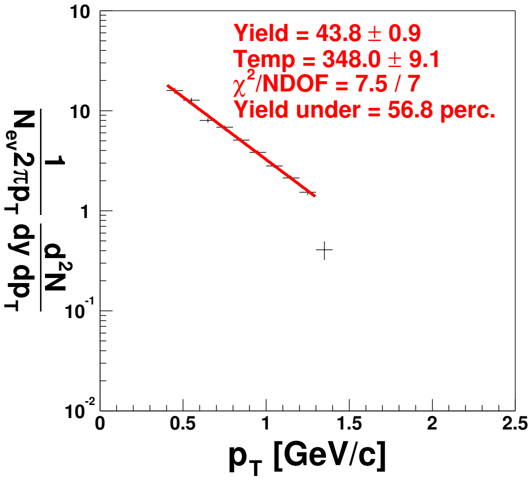

(d) Spectrum for k^- in p_t.

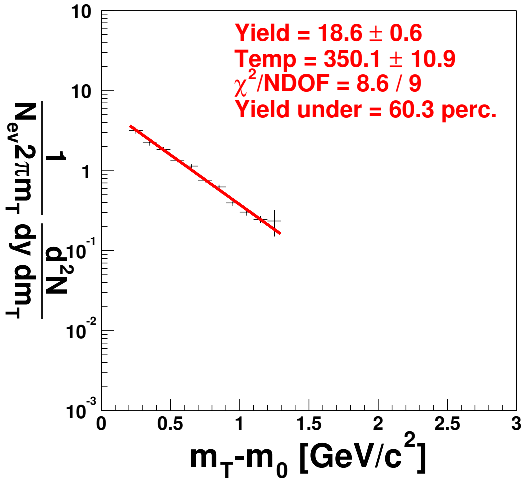

(e) Spectrum for $\bar{p}$ in $m_t - m$.

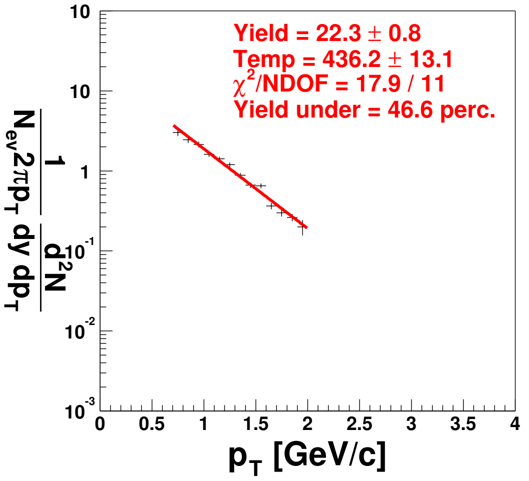

(f) Spectrum for $\bar{p}$ in p_t.

Figure 5.15: The spectra and corresponding fits for negative particles in the rapidity range $y = 0.9 \pm 0.03$.

At midrapitity there is a slight increase in pions around 1.5 GeV/c. These may very well come from high p_t jets, but rather from high field settings. There is also an increase of pions at low p_t, which comes from multiple scattering and from heavier particles which have resonances which decay into low p_t pion states. The exponential approximations are just estimates. We can see a clear bend in the proton and anti-proton spectra, which is interpreted as an evidence of flow. Since we subtract the mass in the $m_t - m$ spectra their extrapolated yields should approach the yields found in Boltzmann fits. They do not have the same tail as the exponential p_t spectra. But even if the exponential $m_t - m$ fits have the same yields they will not have the same slopes as the Boltzmann fits. In figure 5.19 I have fitted these particles with a thermal Boltzmann distribution, in the midrapidity region $y = 0$, where the energy $E = m_t$, since $E = m_t \cosh y$, appendix A. Furthermore I fitted pions, kaons, protons and anti-protons to the $m_t - m$ spectra for the different rapidities to the Boltzmann distribution, (figures 5.16, 5.17, 5.18). Due to heavier particle resonances and decays we have more pions in the low m_t region. In the upper m_t region there is also the influense of high p_t pions coming from jets. Therefore the Boltzmann distribution fits poorly for pions. In all the fits the mentioned temperature (Temp) is $T_{emp} = \frac{T}{\cosh{(y)}}$. The fit functions 5.11 and 5.12 are derived in chapter 4.

$$f(p_t) = \frac{N\sqrt{p_t^2 + m^2}}{2\pi T(m^2 + 2mT + 2T^2)} * e^{-\frac{\sqrt{p_t^2+m^2}-m}{T}} \tag{5.11}$$

$$f(m_t - m) = \frac{N m_t}{2\pi T(m^2 + 2mT + 2T^2)} * e^{-(m_t - m)/T} \tag{5.12}$$

5.3.1 The Blast Wave

Another way to describe the chain of events in the collision is through a blast wave. The basic idea of a blast wave was developed by Philip J. Siemens and John O. Rasmussen [38], see chapter 4.

The idea is to have an expanding system in local thermal equilibrium and describe it through a hydrodynamical model. This leads to equation 4.36.

In my analysis I assume that the flow velocity is constant over the whole r range. This constant velocity will then be the average flow velocity. By doing this in expression 4.36 the integral over radius becomes a delta function and therefore goes to unity. We have

$$\frac{dN}{m_t dm_t} \quad \propto \quad m_t I_0 \left[\frac{p_t \sinh\rho}{T_0}\right] K_1 \left[\frac{m_t \cosh\rho}{T_0}\right]. \tag{5.13}$$

This simplified expression is fitted to the spectra. First I fit all particles individually and finally simultaneously.

In the individual fit I have three fit parameters. The normalization N, the transverse flow velocity β_t and the temperature T_0.

By looking at the individual fits one can see the strong anti-correlation and conclude that there is a wide range, where the flow velocity and temperature is accepted, and especially for the kaons it is difficult to find the correct flow velocity and temperature. Furthermore the idea behind the blast wave is a common flow velocity. In the simultaneous fits I have eight fit parameters, one for each particle normalization, one for flow velocity and one for temperature.

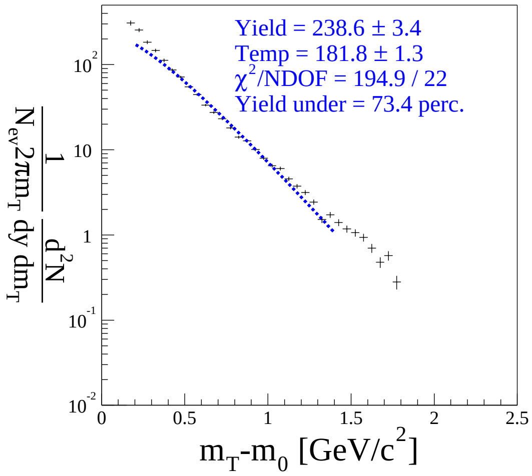

(a) π^+

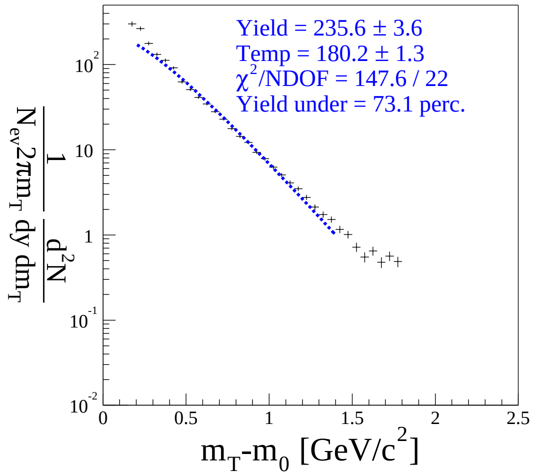

(b) π^-

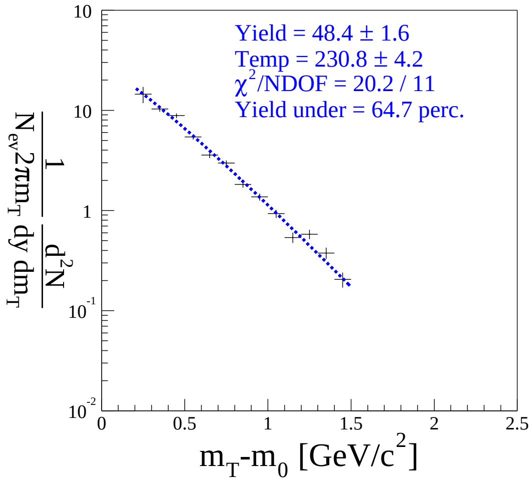

(c) k^+

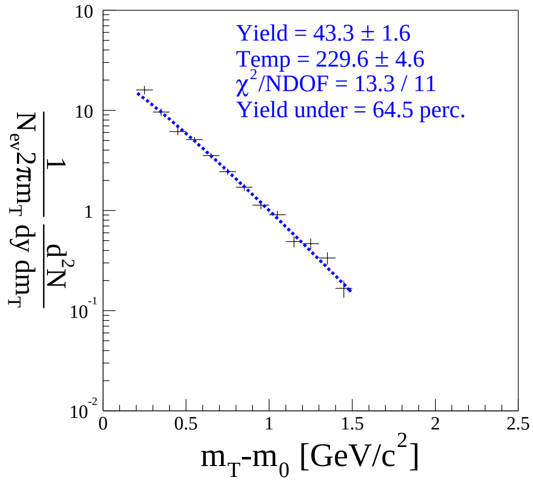

(d) k^-

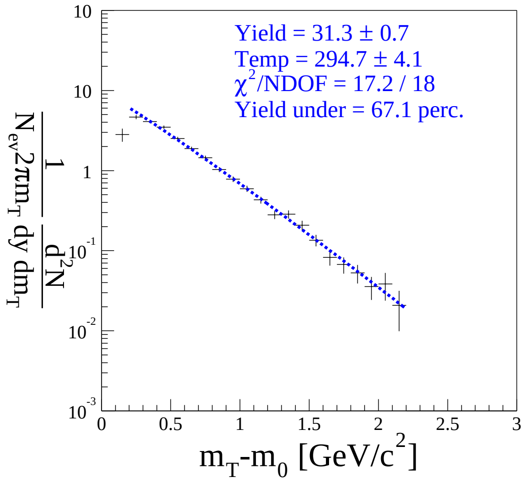

(e) p

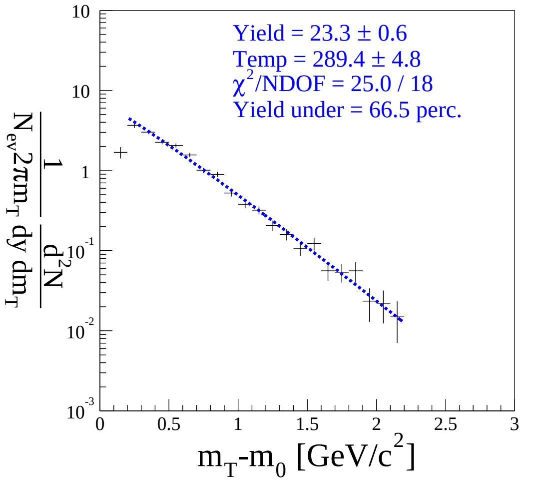

(f) $\bar{p}$

Figure 5.16: The spectra and corresponding Boltzmann fits for pions, kaons, protons and anti-protons in the rapidity range $y = \pm 0.03$.

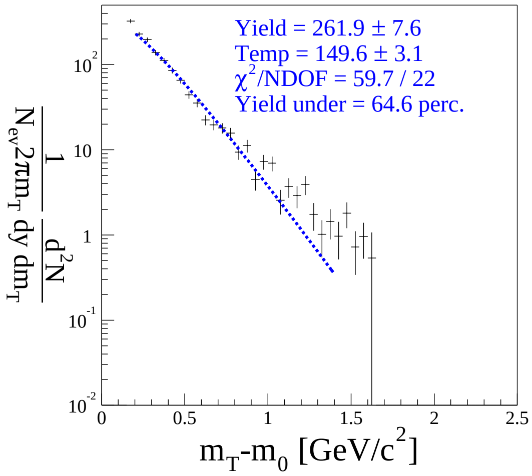

(a) π^+

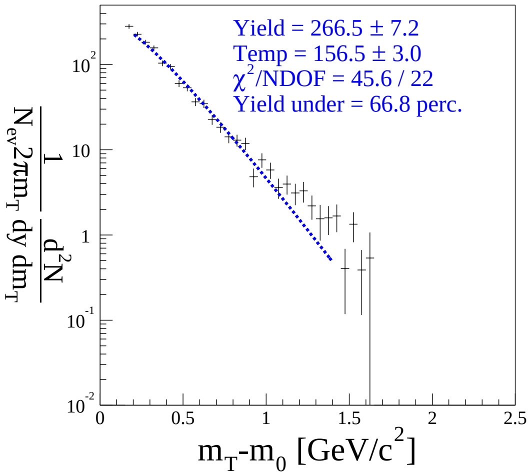

(b) π^-

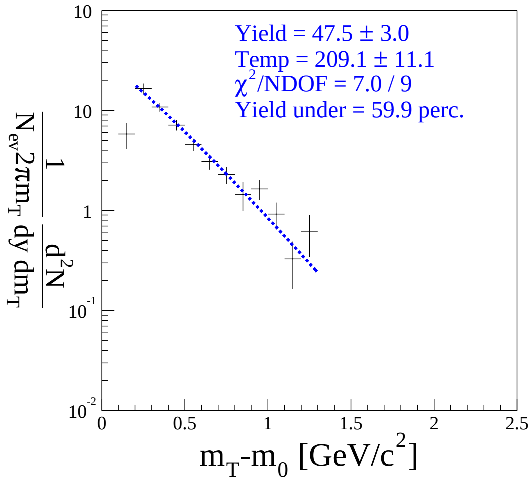

(c) k^+

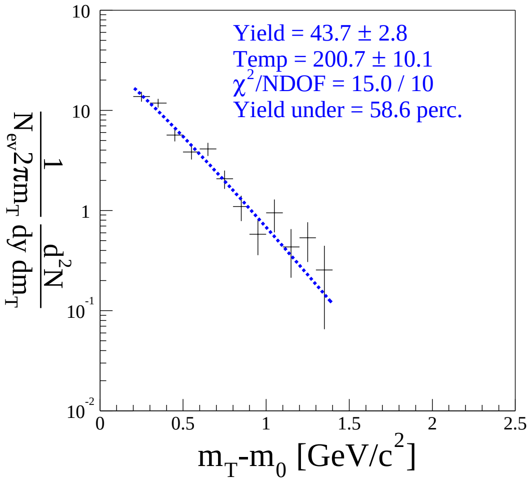

(d) k^-

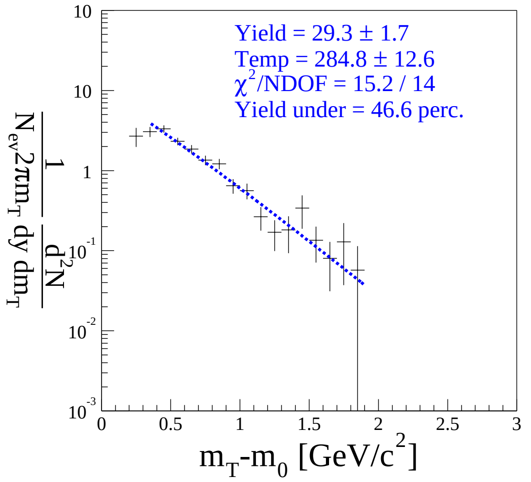

(e) p

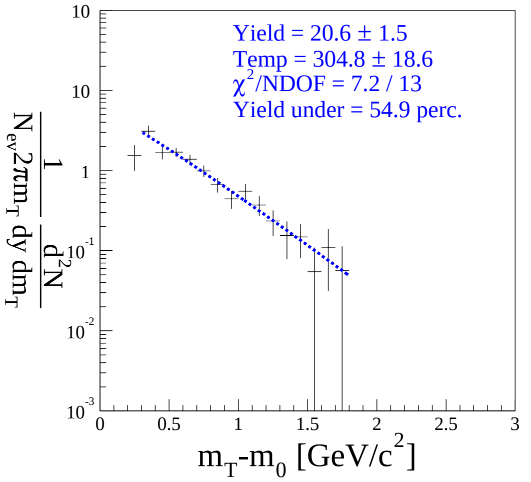

(f) $\bar{p}$

Figure 5.17: The spectra and corresponding Boltzmann fits for pions, kaons, protons and anti-protons in the rapidity range $y = 0.45 \pm 0.03$.

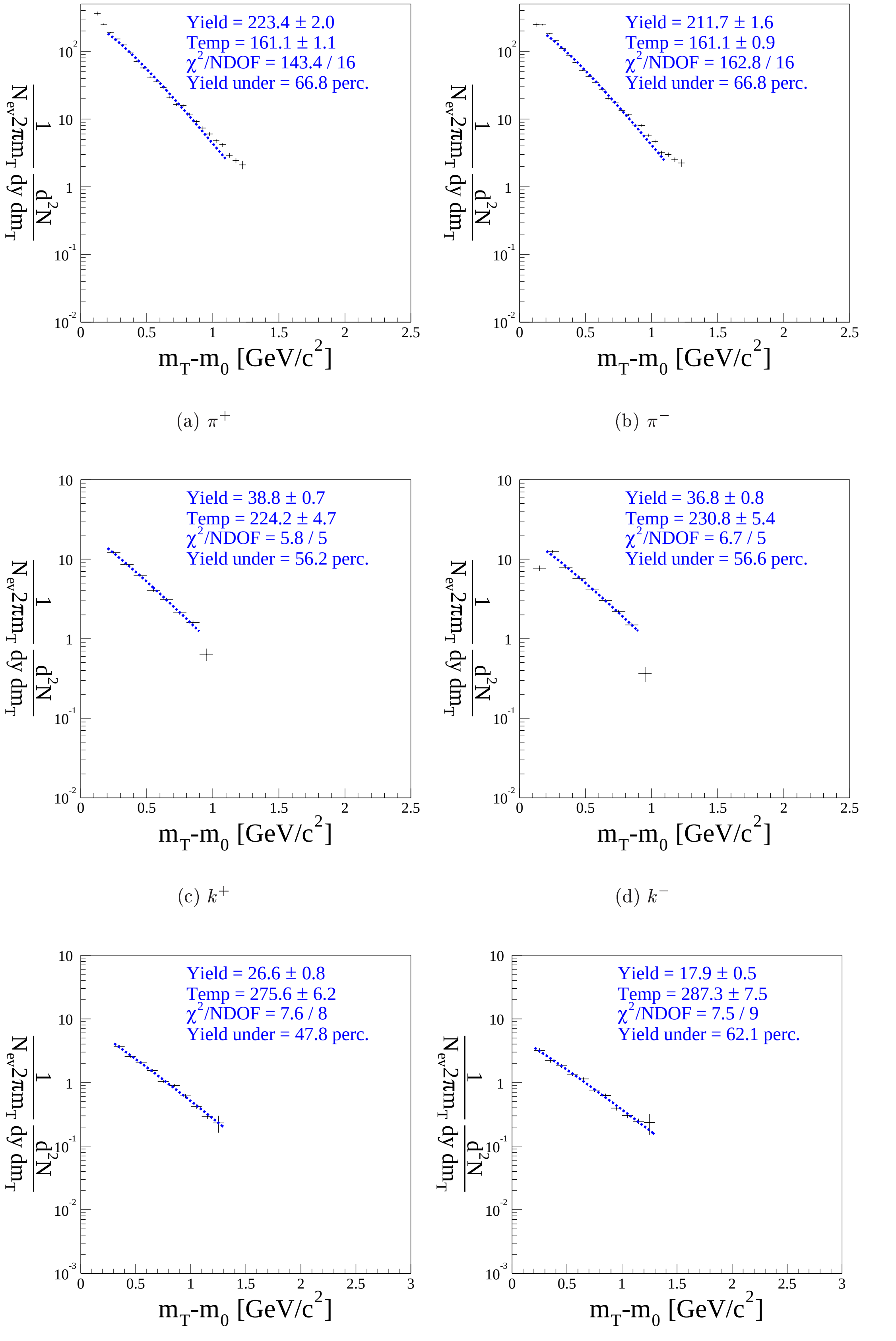

(a) π^+ (b) π^-

(c) k^+ (d) k^-

(e) p (f) $\bar{p}$

Figure 5.18: The spectra and corresponding Boltzmann fits for pions, kaons, protons and anti-protons in the rapidity range $y = 0.9 \pm 0.03$.

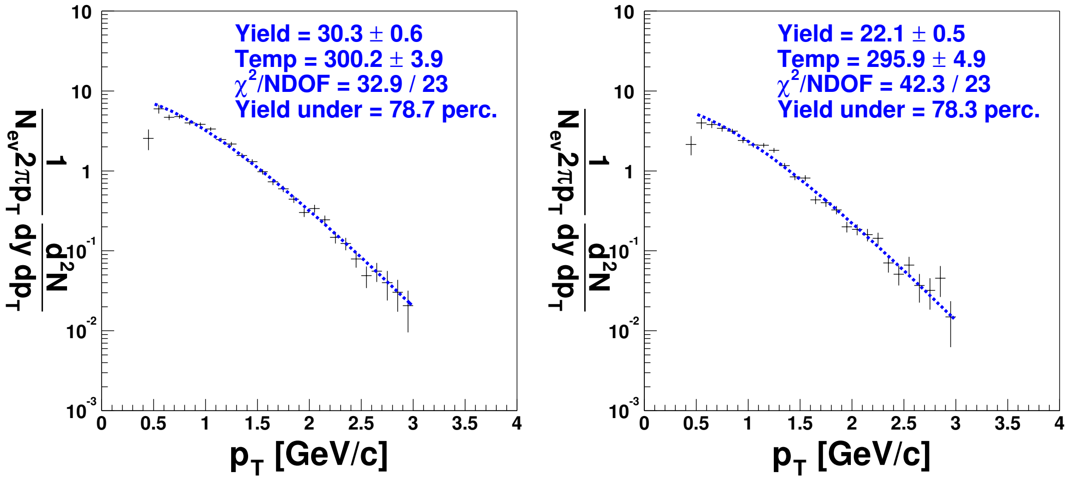

(a) Proton fit in p_t

(b) Anti-proton fit in p_t

Figure 5.19: A Boltzmann fit to protons and anti-protons in p_t. Due to the drop in low p_t the yields are lower for the Boltzmann fit than for exponential p_t. Also the temperatures are lowered for the Boltzmann fit.

The idea is to create a 2D-histogram, with $m_t - m$ on one axis and particle type on the other. Then fit a 2D function to this histogram. All particles are fitted simultaneously.

The value of the simultaneous flow velocity is higher than all the individual flow velocities and the temperature correspondingly lower, also shown in Table 5.3. By looking at the different χ^2 maps 5.23, one realizes that the individual fits all point to a common minimum at lower T and higher β than their own values.

$y = 0$	Positive	Negative
π	$T = 0.156 \pm 0.010$ $\beta_t = 0.416 \pm 0.047$	$T = 0.151 \pm 0.018$ $\beta = 0.427 \pm 0.089$
K	$T = 0.245 \pm 0.259$ $\beta_t = 0.158 \pm 0.259$	$T = 0.231 \pm 0.015$ $\beta_t = 0.224 \pm 0.073$
p	$T = 0.160 \pm 0.016$ $\beta_t = 0.532 \pm 0.037$	$T = 0.151 \pm 0.016$ $\beta_t = 0.546 \pm 0.035$
Sim	$T = 0.117 \pm 0.004$ $\beta_t = 0.615 \pm 0.008$	

Table 5.3: The flow velocities and temperatures from individual and simultaneous fits.

An interesting aspect to check is if there are any significant changes in flow velocity and temperature with rapidity. Therefore simultaneous fits have also been done for the rapidities $y = 0.45$ and $y = 0.9$. The results can be seen in chapter 6.

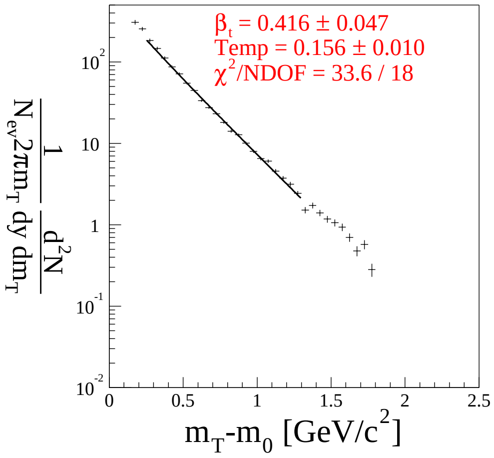

(a) Flow and temperature for pi^+

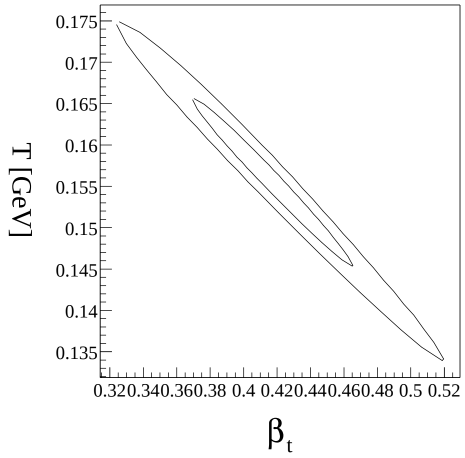

(b) χ^2 map for π^+

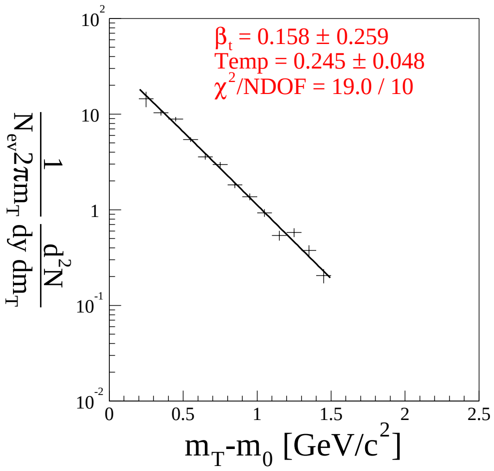

(c) Flow and temperature for K^+

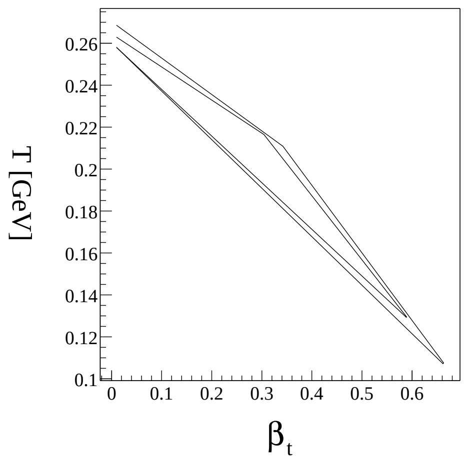

(d) χ^2 map for K^+

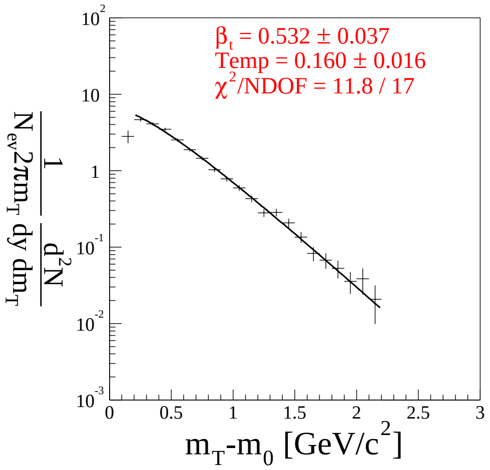

(e) Flow and temperature for p

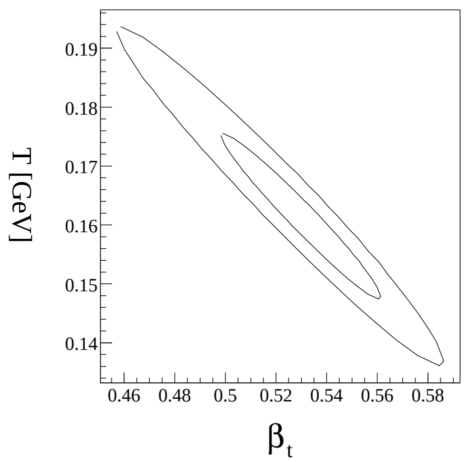

(f) χ^2 map for p

Figure 5.20: Left. Individual blast wave fits for positive particles at $y = 0$. Right. The corresponding χ^2 maps. The lines correspond to $\chi^2_{min} + 1$ and $\chi^2_{min} + 2$. Note the strong anti-correlation between flow and temperature. Due to the low curvature of the kaon spectra it is very difficult to find a proper fit for these, as also reflected in the errors.

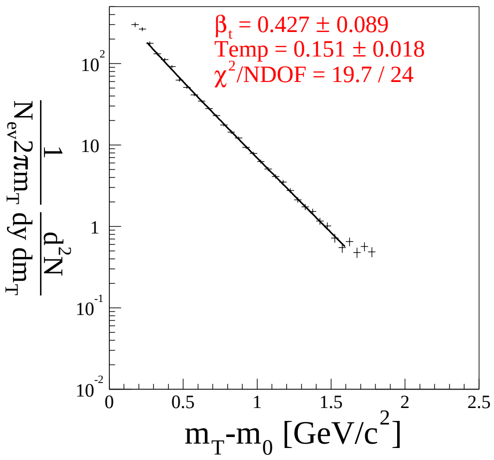

(a) Flow and temperature for pi^-

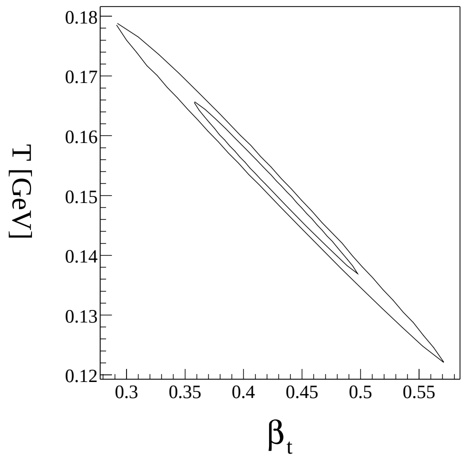

(b) χ^2 map for π^-

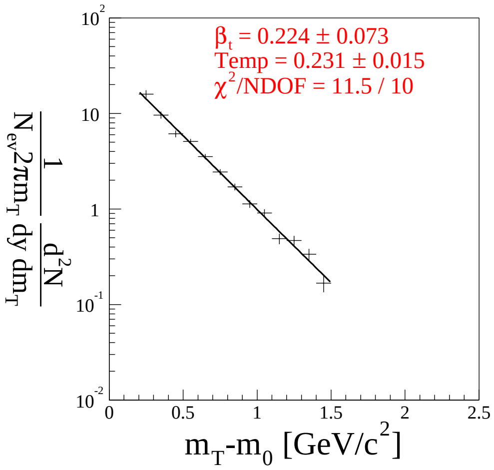

(c) Flow and temperature for K^-

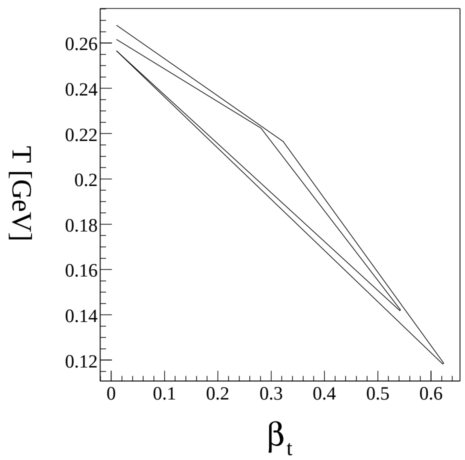

(d) χ^2 map for K^-

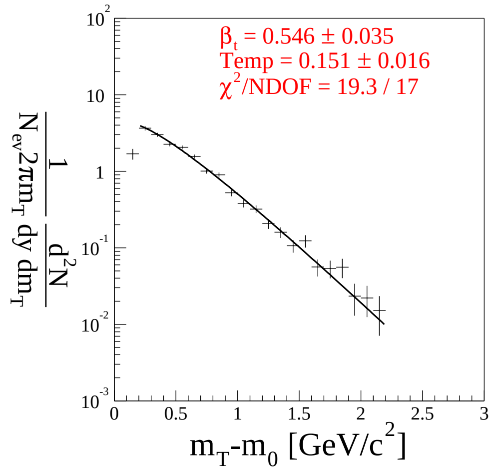

(e) Flow and temperature for $\bar{p}$

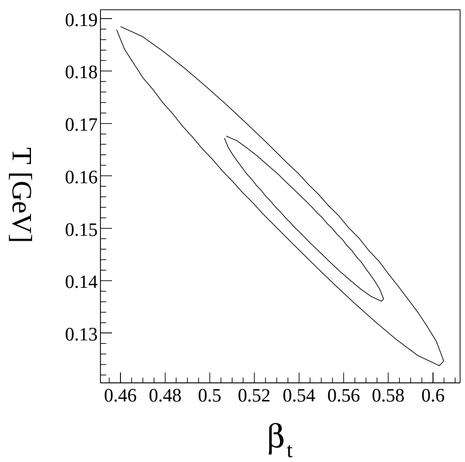

(f) χ^2 map for $\bar{p}$

Figure 5.21: Left. Individual blast wave fits for negative particles. Right, as figure 5.20.

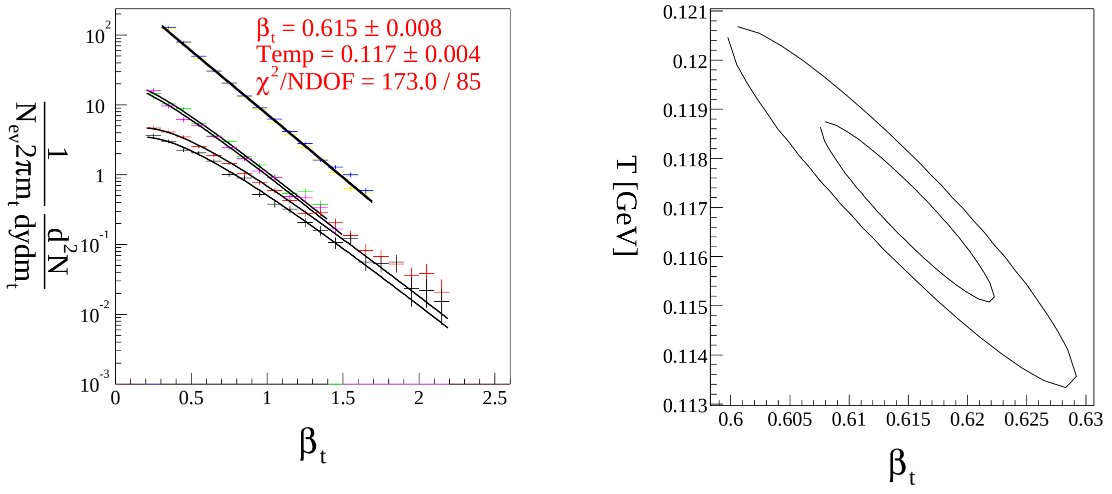

(a) Simultaneous flow and temperature

(b) The χ^2 map for simultaneous fits

Figure 5.22: The simultaneous flow fit. Here notice the much smaller ranges for the anti-correlation between flow velocity and temperature. By using different particle types we get a good estimation of the flow velocity and temperature.

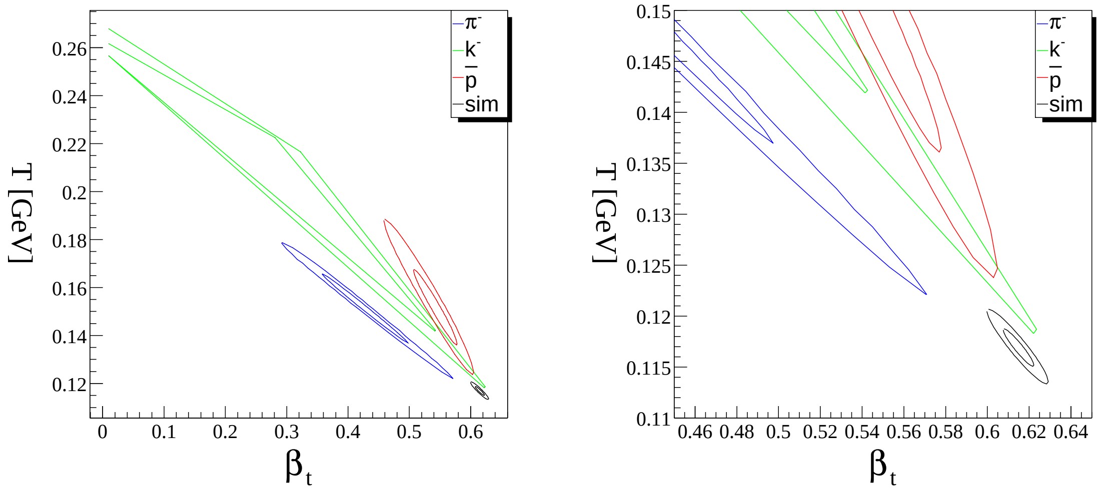

(a) The different χ^2 maps

(b) Zoom

Figure 5.23: A plot of the χ^2 maps for negative particles together with the simultanous χ^2 map. All the individual fits have bigger freedom to move in the anti-correlation directions toward the simultaneous fit values. Right. Zoom of the maps.

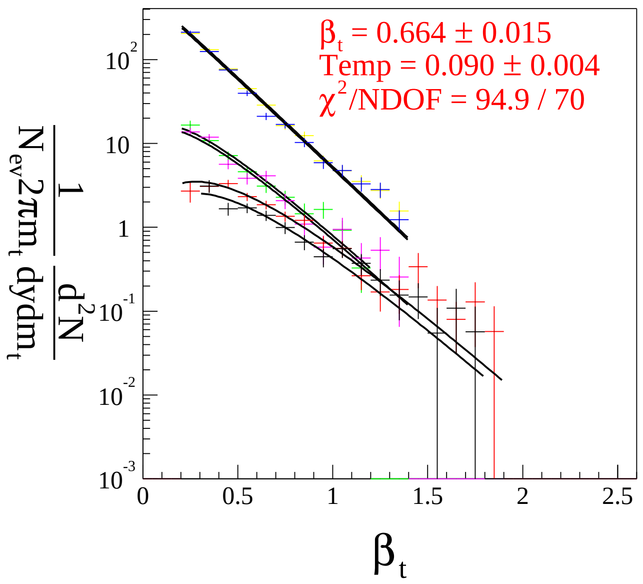

(a) $y = 0.45$

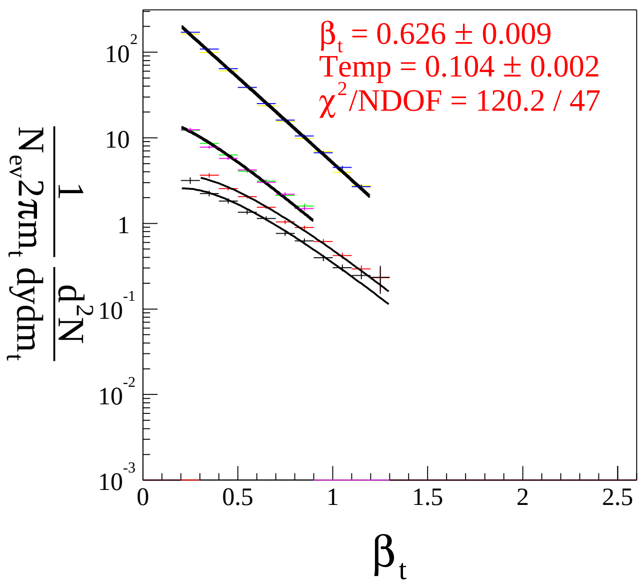

(b) $y = 0.9$

Figure 5.24: The flow velocities and temperatures for the simultaneous fit for rapidities $y = 0.45$ (left) and $y = 0.9$ (right).

Chapter 6

Results and Discussion

In chapter 5 the spectra were fitted with different functions based on two models (thermal and blast wave). Results will be collected in this chapter. All values for rapidity $y = 3$ are obtained by fitting the spectra in [19] with exponential m_t.

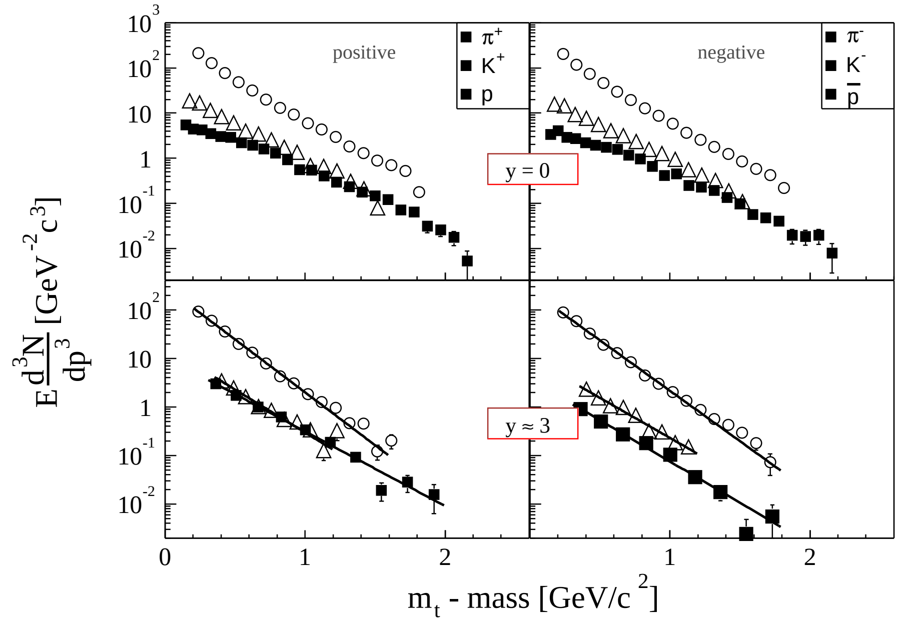

Figure 6.1: The spectra taken from [19] and fits made to get yields and temperatures. The drop in protons and anti-protons at $m_t - m = 1.55$ is due to the energy threshold, between vetoing pions and kaons out and making proton PID in the RICH. At this threshold there is an energy issue that yet has to be solved.

6.1 The Estimated Yields.

The yields are estimated from extrapolation of the fits from the different fit functions. The yields differ in value, since the extrapolations of the models are different, also see figure 6.2. The different yields have a plateau behavior around midrapidity in common.

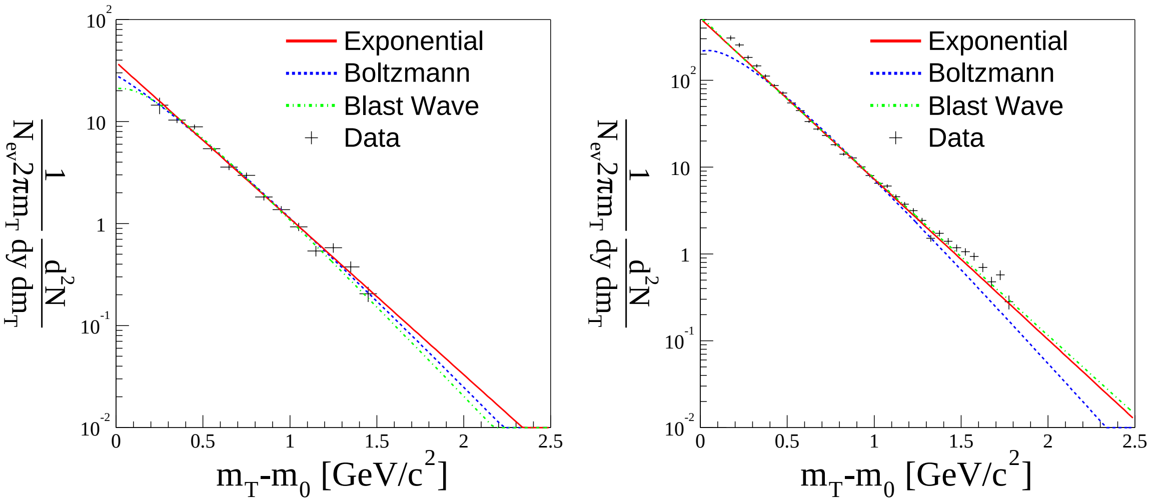

(a) kaons

(b) pions

Figure 6.2: The extrapolations and data for kaons and pions at midrapidity. At low and high p_t there is a deviation between the models. This will affect the yield calculations.

6.1.1 The Exponential Fit in Transverse Mass

In chapter 5 I fitted the created spectra with exponentials in $m_t - m$ and p_t. From these two approximations the yields and flow velocity for different particles could be estimated. In figure 6.3 the different yields for the different particle types and rapidities are shown. There is a slight decrease, 10% for $y = 0.9$. This might very well come from systematic errors. At this forward angle, there are more background radiation, which decreases the efficiency of TPM1. The corrections for this effect may not be sufficient enough. The thickness of the beam pipe is also increasing by a factor $1/\sin 40$, reducing the number of particles. So, the particles have approximately the same yields for the different rapidities. This is an indicator of the presence of a Bjorken plateau around midrapidity. This figure will be used to make kaon to pion ratio calculations. Stopping will also be discussed based on the results shown here.

Particle	$y = 0$	$y = 0.45$	$y = 0.9$	$y = 3.0$
π^+	283.8 ± 4.5	284.4 ± 12.8	255.4 ± 2.4	128.1 ± 1.8
π^-	278.1 ± 4.7	298.9 ± 12.4	240.8 ± 1.8	118.5 ± 2.3
k^+	52.8 ± 1.7	50.8 ± 3.2	41.1 ± 0.7	19.9 ± 1.2
k^-	47.3 ± 1.8	46.2 ± 2.9	39.1 ± 0.8	12.9 ± 0.7
p	33.9 ± 0.8	34.8 ± 2.7	27.8 ± 0.8	23.3 ± 0.6
$\bar{p}$	25.1 ± 0.7	21.6 ± 1.6	18.6 ± 0.6	7.2 ± 0.3

Table 6.1: The estimated yields for the different particles and rapidities shown in figure 6.3. The results from $y = 3$ are also added.

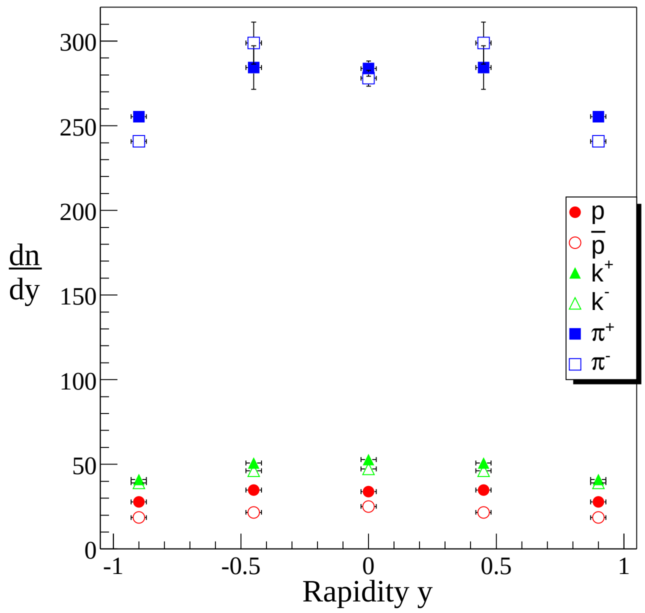

Figure 6.3: The yields are estimated from fits in exponential $m_t - m$ for the different rapidities and particles investigated in this thesis. Negative rapidities mirror positive rapidities around $y = 0$.

6.1.2 The Boltzmann Fits

A Boltzmann distribution was also used as a fitting function for the spectra in chapter 5. The results of the estimated yields from this model are presented in figure 6.4 and table 6.2. The pion fits have a large χ^2, also see the Boltzmann fits in section 5.3. Also this model has a plateau for the yields around midrapidity.

Particle	$y = 0$	$y = 0.45$	$y = 0.9$
pi^+	242.9 ± 3.4	261.9 ± 7.6	223.4 ± 2.0
pi^-	239.8 ± 3.6	266.5 ± 7.2	211.7 ± 1.6
k^+	48.4 ± 1.6	47.5 ± 3.0	43.7 ± 2.8
k^-	43.3 ± 1.6	43.7 ± 2.8	36.8 ± 0.8
p	31.3 ± 0.7	29.3 ± 1.7	26.6 ± 0.8
$\bar{p}$	23.3 ± 0.6	20.6 ± 1.5	17.9 ± 0.5

Table 6.2: The estimated yields based on a Boltzmann fit.

6.1.3 The Blast Wave

Once the blast wave model is fitted to the spectra it is also normalized to the same. Thereby the yields can be calculated by integration over m_t.

$$\frac{dn}{dy} = \int_m^\infty 2\pi N m_t^2 I_0 \left[\frac{p_t \sinh\rho}{T_0}\right] K_1 \left[\frac{m_t \cosh\rho}{T_0}\right] dm_t, \tag{6.1}$$

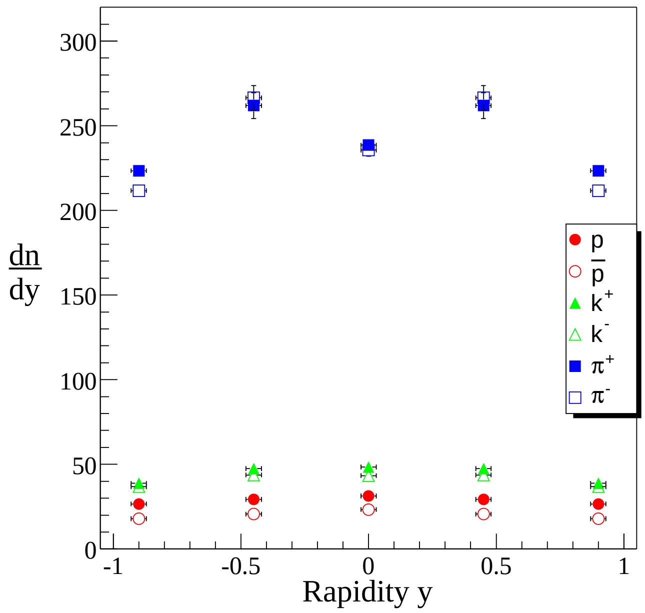

Figure 6.4: The yields estimated from a Boltzmann model. The negative rapidities are mirrored in the positive.

where N is the normalization constant. The other variables are explained in chapter 4. The errors in table 6.3 are estimates. When fitting with a blast wave function, the fits are made for a wider range in m_t. Therefore more data is included in the fits, and the fits should have smaller errors than for the exponential fits. Therefore the errors are over-estimated on an assumption that the errors are in the same order of magnitude as for the yields calculated in the exponential m_t fits. Also the blast wave model indicates a Bjorken plateau around midrapidity.

Particle	$y = 0$	$y = 0.45$	$y = 0.9$
π^+	287.0 ± 5.6	289.0 ± 13.0	256.9 ± 2.6
π^-	275.1 ± 5.5	305.6 ± 13.5	243.7 ± 2.4
k^+	46.7 ± 1.9	39.9 ± 2.4	35.9 ± 0.9
k^-	41.7 ± 1.7	36.0 ± 1.5	34.7 ± 0.9
p	25.9 ± 0.8	20.4 ± 1.6	19.5 ± 0.6
$\bar{p}$	19.1 ± 0.6	14.8 ± 1.2	13.8 ± 0.4

Table 6.3: The estimated yields calculated from the simultaneous blast wave fits.

6.2 The Estimated Slope.

In chapter 2 the slope parameter of the fits was explained. There were also shown results from the NA44 experiment, figure 2.18. By using equation 2.4, the freeze out temperature and

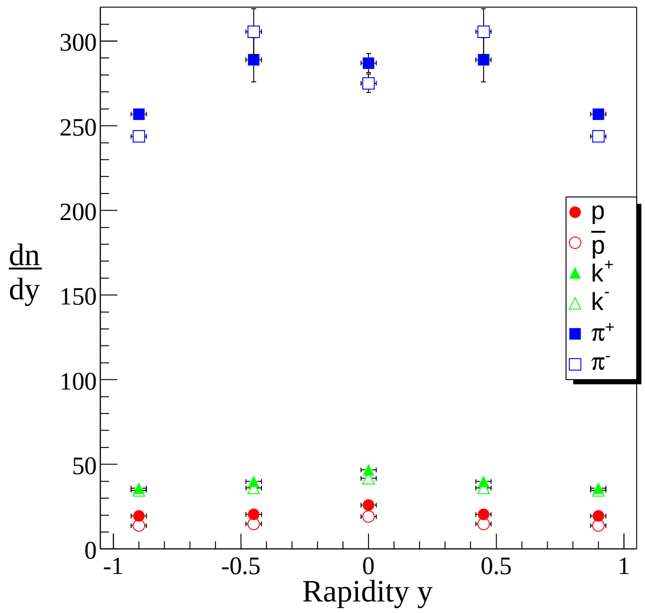

Figure 6.5: The yields calculated from the simultaneous blast wave fits for different rapidities. Negative rapidities mirror the positive rapidities.

flow velocity can be deduced for the exponential and Boltzmann fits. The blast wave model is a hydrodynamical model and the flow velocity and freeze out temperature are estimated directly from the fit.

6.2.1 Slopes from the Exponential fits

The slopes found from exponential $m_t - m$ fits in chapter 5 are here presented for the different particle masses and rapidities in figure 6.6 and table 6.4. Also added are the values from $y = 3$. In figure 6.6 the slopes are different for the different particle masses. If we had a static source

Particle	$y = 0$	$y = 0.45$	$y = 0.9$	$y = 3.0$
π^+	235.0 ± 2.1	202.2 ± 6.2	213.0 ± 1.8	199.3 ± 1.8
π^-	232.8 ± 2.1	208.5 ± 6.0	215.1 ± 1.5	208.9 ± 2.1
k^+	283.6 ± 6.1	256.0 ± 16.1	289.3 ± 7.7	245.6 ± 12.0
k^-	281.8 ± 6.6	248.7 ± 14.8	298.0 ± 8.9	263.0 ± 11.7
p	344.3 ± 6.0	314.3 ± 18.7	330.7 ± 8.8	282.6 ± 5.8
$\bar{p}$	338.9 ± 7.1	368.3 ± 26.3	350.1 ± 10.9	255.8 ± 8.0

Table 6.4: The slopes for the different particles and rapidities in exponential $m_t - m$ fits, with temperature in MeV.

in global thermal equilibrium, all particles would have the same temperature (slope). Instead we assume there is local thermal equilibrium.

The fact that the slope parameter increases with mass is a clear sign of flow, equation 2.4.

By fitting this equation to the different slope parameters in figure 6.6, the freeze out temperature T_{fo} and β_t are deduced. If there is a Bjorken plateau around midrapidity the flow velocity around midrapidity should also be the same. The rapidities are fitted to function 2.4 and the results can be reviewed in table 6.5. It is clear that the small changes in the flow velocity are not significant and the existence of a Bjorken plateau around midrapidity seems plausible. At rapidity $y = 3$ there is clearly a lower flow velocity. Here the Bjorken plateau is no longer present.

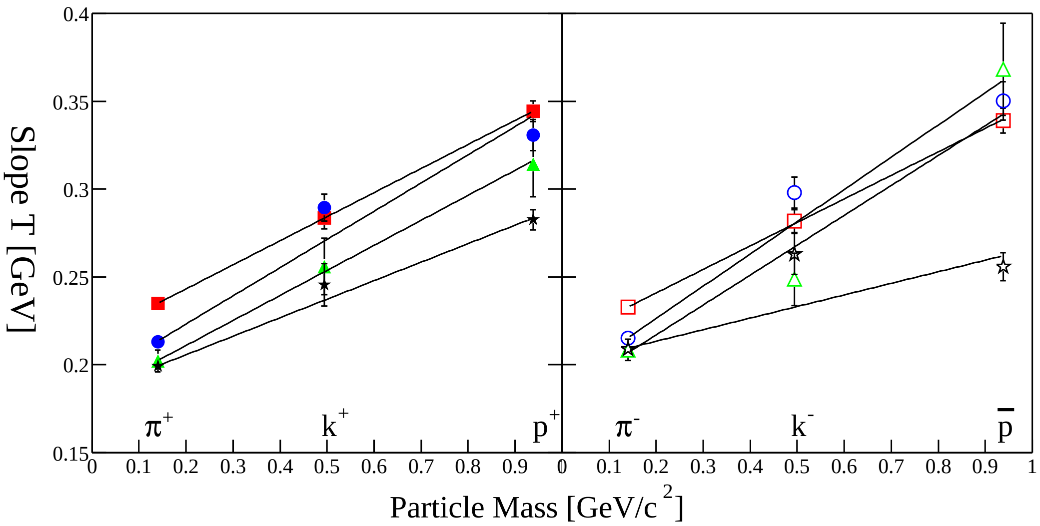

Figure 6.6: The slope parameters for the different rapidities, $y = 0$ (red squares), $y = 0.45$ (green triangles), $y = 0.9$ (blue circles) and $y = 3$ (black stars).

β_t and T_{fo}		$y = 0$	$y = 0.45$	$y = 0.9$	$y = 3.0$
Pos	β_t^2	0.137 ± 0.008	0.142 ± 0.023	0.161 ± 0.01	0.105 ± 0.007
	β_t	0.37 ± 0.004	0.377 ± 0.012	0.401 ± 0.005	0.324 ± 0.004
	T_{fo}	0.216 ± 0.003	0.183 ± 0.008	0.191 ± 0.003	0.185 ± 0.002
Neg	β_t^2	0.134 ± 0.009	0.170 ± 0.028	0.184 ± 0.012	0.066 ± 0.01
	β_t	0.366 ± 0.005	0.412 ± 0.014	0.429 ± 0.006	0.245 ± 0.005
	T_{fo}	0.214 ± 0.003	0.183 ± 0.008	0.190 ± 0.002	0.200 ± 0.003

Table 6.5: Flow velocities and freeze out temperatures calculated by fitting equation 2.4 to values from exponential fits.

6.2.2 Slopes from the Boltzmann fits

In the same way as the slopes were found by fitting exponentials to the spectra, also the thermal Boltzmann distribution were fitted to spectra. Here the slope parameter is $T^* = \frac{T}{\cosh(y)}$, where T is the actual temperature. The results are shown in figure 6.7. From figure 6.7 it can be seen that there is no significant difference in the flow velocities. But there is a clear difference between the slopes for the Boltzmann fits and the Exponential fits, see figure 6.11.

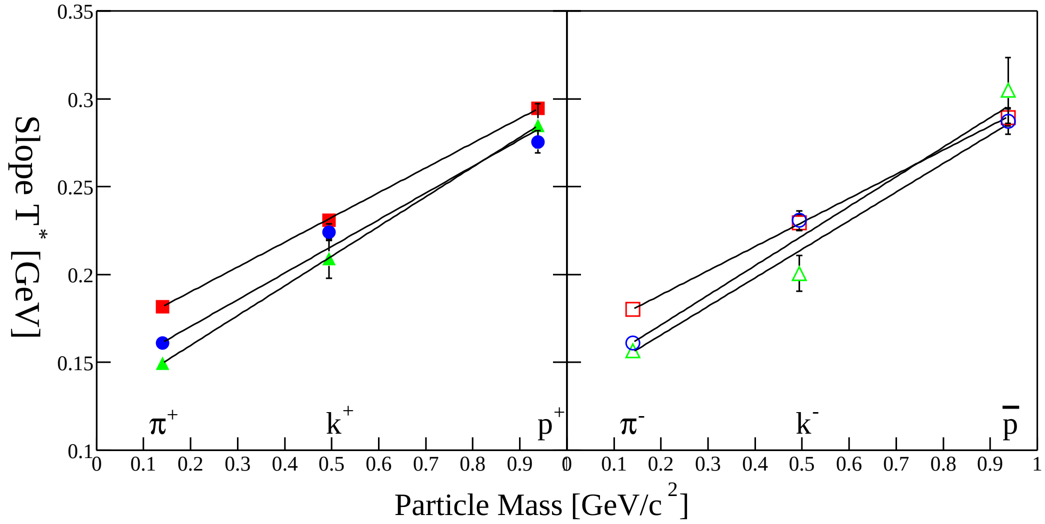

Figure 6.7: The slope parameters T^* for the different particles and rapidities estimated with a Boltzmann distribution. Also shown are the fits from equation 2.4.

β_t and T_{fo}		$y = 0$	$y = 0.45$	$y = 0.9$
Boltz pos	β_t^2	0.143 ± 0.005	0.169 ± 0.015	0.152 ± 0.006
	β_t	0.378 ± 0.003	0.411 ± 0.008	0.390 ± 0.003
	T^*_{fo}	0.160 ± 0.002	0.126 ± 0.004	0.140 ± 0.002
Boltz neg	β_t^2	0.140 ± 0.006	0.163 ± 0.019	0.169 ± 0.008
	β_t	0.374 ± 0.003	0.404 ± 0.01	0.411 ± 0.004
	T^*_{fo}	0.159 ± 0.002	0.133 ± 0.005	0.138 ± 0.002

Table 6.6: Flow velocities and freeze out temperatures (GeV) for Boltzmann distributions. The temperature T^* is used as slope parameter.

6.2.3 Flows and Temperatures from the Blast Wave

In section 6.2.1 and 6.2.2 the flow velocity was calculated by fitting the slope parameters in figure 6.6 and 6.7. Another way to describe flow is through the blast wave model, chapter 4. In chapter 5 this model was applied to data, where spectra were fitted. A constant flow profile ($\alpha = 0$) was used, also described in chapter 5. The fit has been done for the rapidities $y = 0$, $y = 0.45$ and $y = 0.9$, and the results are shown in figure 6.8 and table 6.7.

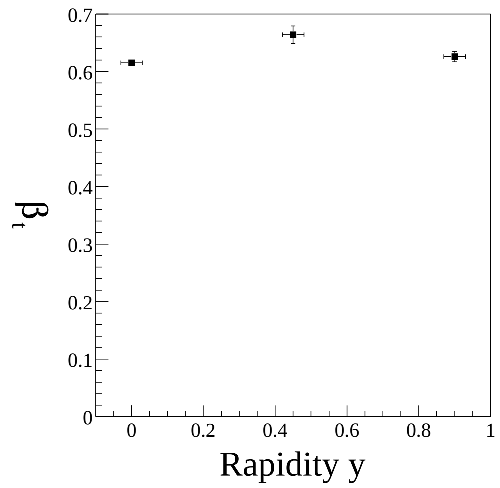

(a) The transverse flow β_t

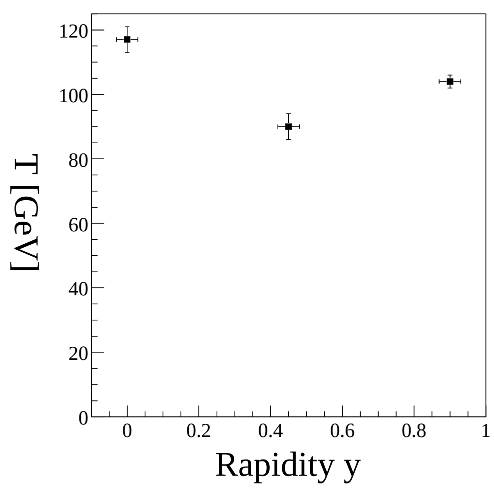

(b) The transverse flow β_t

Figure 6.8: The radial flow β_t and freeze out temperatures T_{fo} for the blast wave fit, with a constant flow profile.

Blast Wave	$y = 0$	$y = 0.45$	$y = 0.9$
β_t	0.615 ± 0.003	0.664 ± 0.015	0.626 ± 0.009
$T_{fo}[GeV]$	0.117 ± 0.004	0.090 ± 0.004	0.104 ± 0.002

Table 6.7: The flow velocities and temperatures for the different rapidities in a blast wave model.

There is a strong anti-correlation between temperature and flow. This anti-correlation combined with systematic errors give too large errors to call the small fluctuation around $y = 0.45$ significant. Also the blast wave model gives nearly constant yields over rapidity $y = 0$ to $y = 0.9$, although with different values compared to the other two fits.

Other experiments show a limiting behavior for flow velocity and temperature when beam energies become sufficiently large (SPS). For data presented in this thesis the freeze out temperature is the same, while the flow velocity has increased compared to SPS.

In the event of a phase transition, the major flow build up will occur during the early stages of the collision, in the QGP and mixed phases [47]. The flow velocity measured from experiment is measured after phase transition and thermal freeze out. In figure 6.10 it is clear that the two measured flow velocity values from SPS and RHIC should approach each

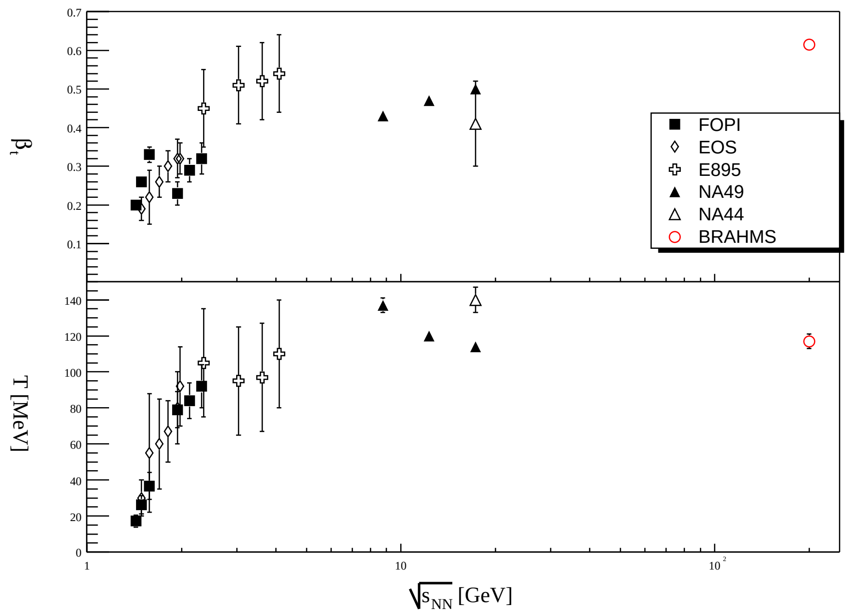

Figure 6.9: The flow velocities and temperature versus center of mass energy. The different data points are taken from [43, 44, 45, 27]. The points from this thesis are shown with statistical errors only.

other if the system has a sufficiently long life. The calculations are made for central $U + U$ and peripheral $Pb + Pb$ collisions in (3+1) dimensional hydrodynamics. In central $Au + Au$ collisions the conditions are very similar to the central $U + U$ collisions. At midrapidity the measured flow velocity is close to that predicted by this hydrodynamical model.

6.3 Summary

At rapidity $y = 0$ the definition of slope are the same for exponential and Boltzmann fits, $\cosh(y = 0) = 1$. Remembering that there was a very small difference in the yields for protons, the answer will not be the same for the slopes. A comparison of the two is done in figure 6.11.

While the yields for kaons and protons were similar for exponential $m_t - m$ and Boltzmann fits we get a different value for the blast wave. The yields from the blast wave includes the shift from flow in the $m_t - m$ spectra. This shift is more present for heavier particles, since they are most affected by flow. The effect is clearly seen in figure 6.12, where the ratio between yields estimated from the blast wave and exponential fits are shown. The difference is as much as 30% between yields of the two models. The errors are again estimated from the exponential fits.

In figure 6.13 the freeze out temperatures T_{fo} are compared to each other for the different fits and rapidities. Also the chemical freeze out temperature calculated from the Becattini model [23] (figure 2.16) is put in. The exponential freeze out temperatures end up above the chemical freeze out. If elastic scattering would occur at higher energies than the chemical

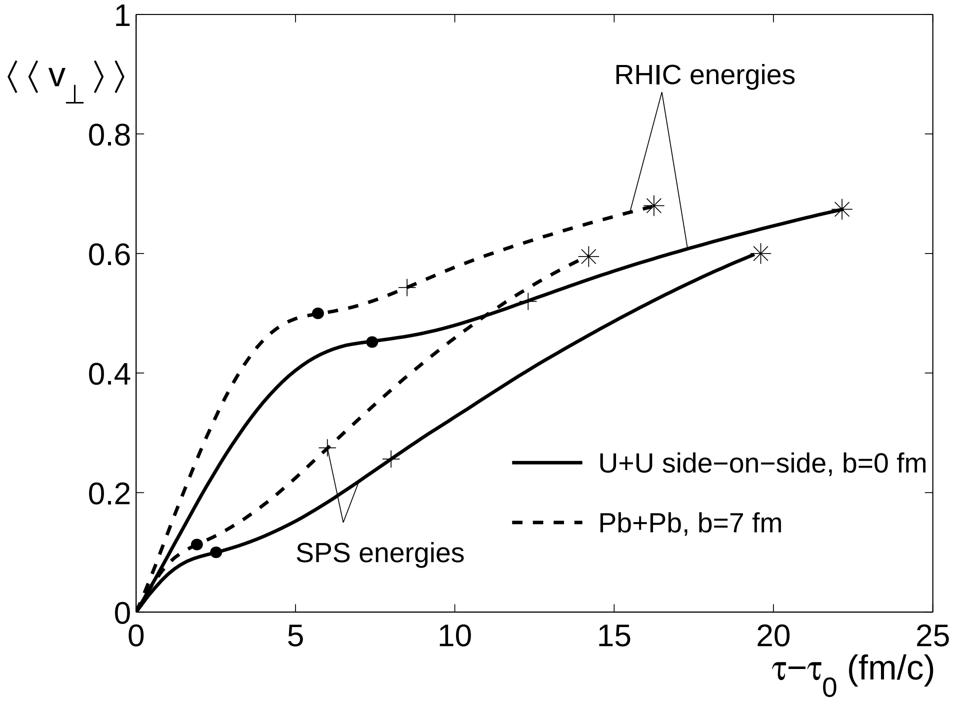

Figure 6.10: The flow velocity evolution versus time, ($\tau_0 = 0.38$ fm/c). Shown are also the end of the QGP phase (points) and mixed phase (crosses). The end points are the thermal freeze out. Figure taken from [47].

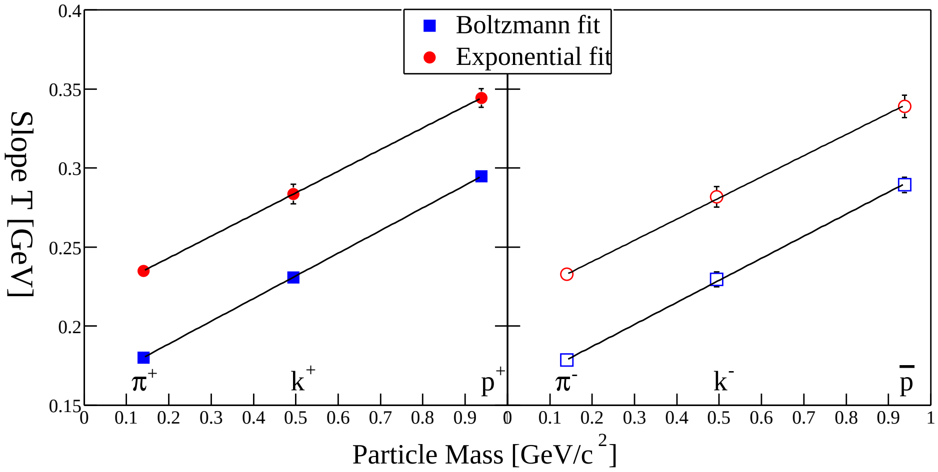

Figure 6.11: The two slopes for exponential $m_t - m$ and the thermal Boltzmann model at midrapidity ($y = 0$). Clearly the slopes are lower for the Boltzmann case.

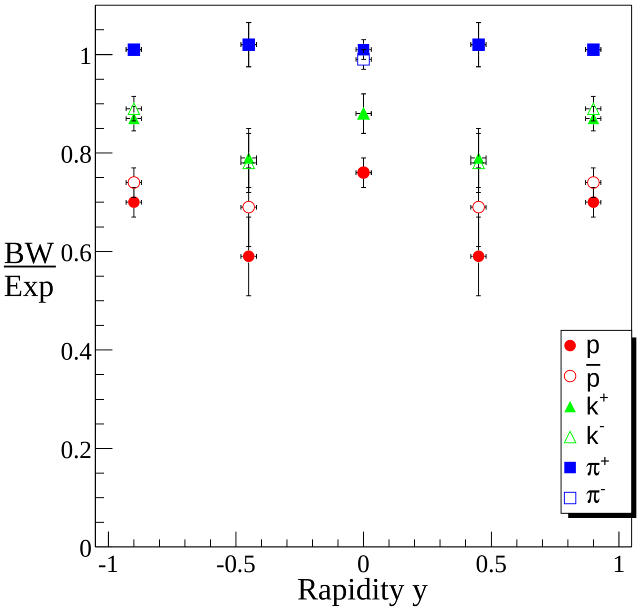

Figure 6.12: The yield ratios between the blast wave model and the exponential fits.

freeze out, this would mean that particles of high energy collides without new particles being created. This is not the case. There clearly is a particle production in the collisions, and we conclude that the exponential results are non physical.

6.3.1 Stopping in the Collisions

As mentioned in chapter 2, one way to look at the stopping or transparency of the collisions is to measure the ratio of protons to anti-protons for different rapidities. Also the net-baryon density around midrapidity gives an indication of the degree of stopping. The ratios and net-proton values are calculated from the estimated yields for the different models. The results for the ratios are presented in figure 6.14 and table 6.8 and for the net-protons in figure 6.15 and table 6.9.

From figure 6.14 it is clear that all models mentioned here agree on the anti-proton to proton ratio. Since all ratios agree, the difference in the net-proton values are proportional to the number of particles in the different models, also seen in figure 6.15. There is a clear

$\bar{p}/p$	$y = 0$	$y = 0.45$	$y = 0.9$
Exp	0.74 ± 0.03	0.62 ± 0.07	0.67 ± 0.03
Boltz	0.74 ± 0.03	0.70 ± 0.07	0.67 ± 0.03
BW	0.74 ± 0.03	0.73 ± 0.08	0.71 ± 0.03

Table 6.8: The anti-proton to proton ratios calculated from the estimated yields.

decrease in the net-proton yield compared to experiments from lower beam energies. The anti-proton to proton ratio tends toward one, indicating that pair production dominates over stopped baryons in the collision. Even if the transparency is high there is an increasing energy

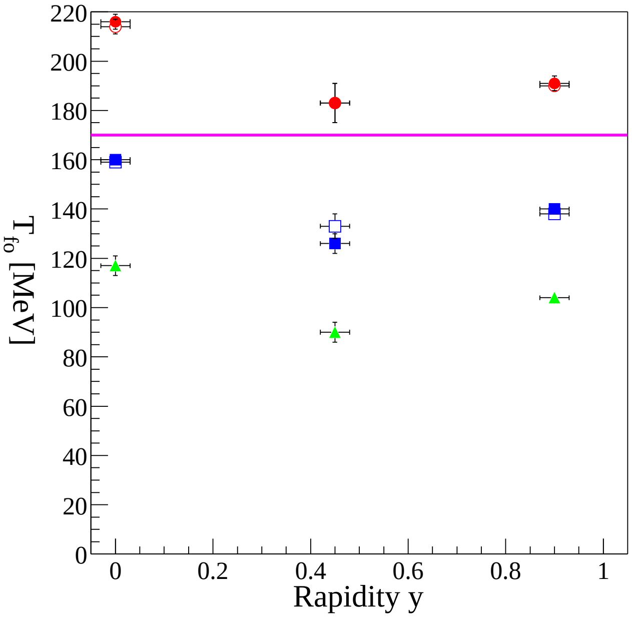

Figure 6.13: The different freeze out temperatures for the different fits, exponential (red circles), Boltzmann (blue squares) and Blast Wave (green triangles). For the Boltzmann fit T^*_{fo} is calculated from T^*. The purple line corresponds to the chemical freeze out temperature $T_{ch} = 170$ MeV, from figure 2.16.

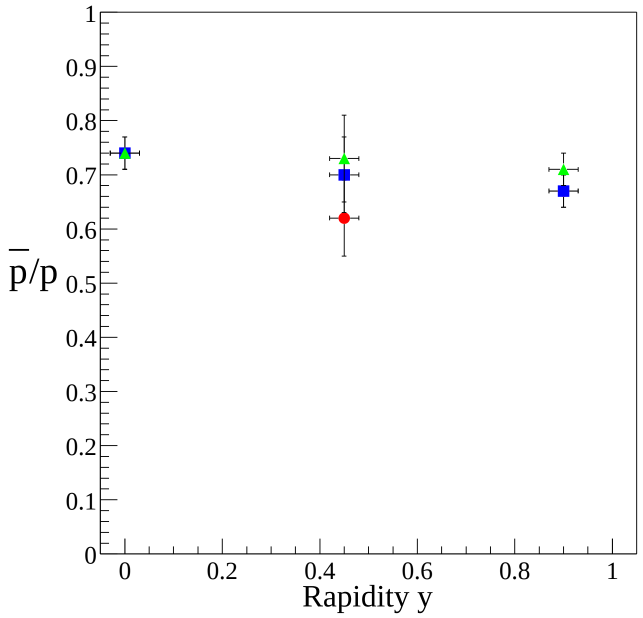

Figure 6.14: Shown are the anti-proton to proton ratios for the different models and rapidities, exponential (red circles), Boltzmann (blue squares) and blast wave (green triangles). At rapidity $y = 0$ all ratios have the same value.

deposit in the collision as the collision energies increase. This is due to the interactions of the color field, giving particle production from the breaking of color strings. It is clearly seen in figure 6.16, where net-protons and the number of produced pions are plotted.

$p - \bar{p}$	$y = 0$	$y = 0.45$	$y = 0.9$
Exp	8.8 ± 1.1	13.2 ± 3.1	9.2 ± 1.0
Boltz	8.0 ± 0.9	8.7 ± 2.3	8.7 ± 0.9
BW	6.8 ± 1.0	5.6 ± 2.0	5.7 ± 0.7

Table 6.9: The net-proton values calculated from the yields of the different models.

6.3.2 The Kaon Production

If a QGP phase transition is to occur an expected signal is strangeness enhancement, section 2.3.1. In figure 6.17, the kaon to pion ratios for the different fits are shown. Depending on the models, the ratios change with the yields, see figure 6.2. The blast wave model follows the exponential shape for the pions, but bends off for kaons, while the Boltzmann bends off for pions, but is not as strongly affected in the kaon fit. Therefore the blast wave fits give the lowest values and the Boltzmann fits the highest. In the extension this means that the chemical freeze out temperature depends on which of the models being used.

When comparing to other experiments (figure 6.18) the k^+/π^+ ratio is bigger than k^-/π^- ratio for SPS energies, explained in section 2.3.1. At RHIC energies the primary baryons are far away from the interaction point when pair production begins. Therefore it is interesting

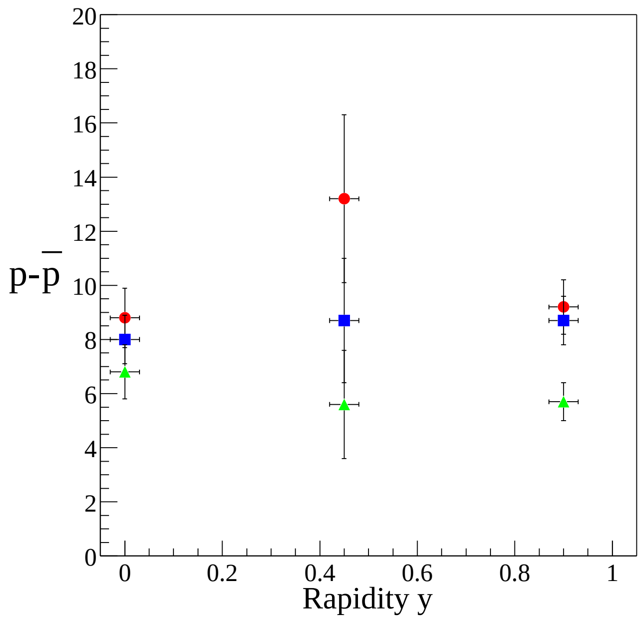

Figure 6.15: The net-proton values for the different models used, exponential (red circles), Boltzmann (blue squares) and blast wave (green triangles).

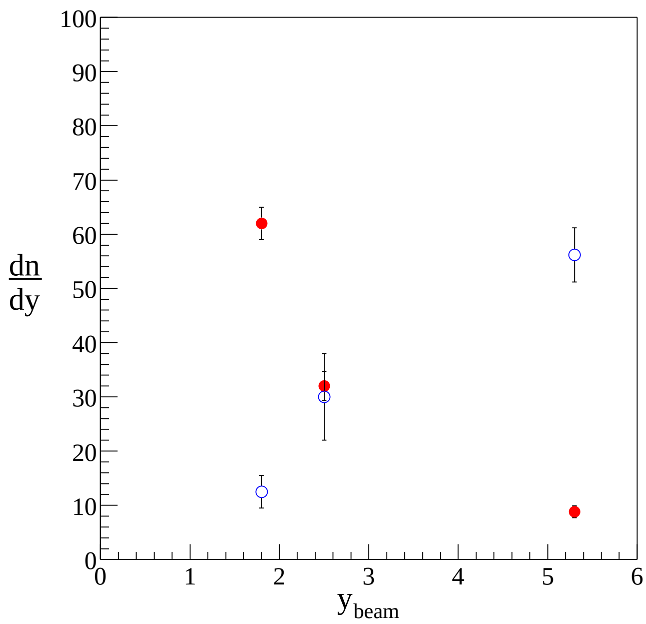

Figure 6.16: The net-proton versus beam rapidity (filled circles) and the number of produced pions in the collisions $(\pi^+ + \pi^-)/10$ (hollow circles). The pion yields, from low to high rapidity are from [10, 16] and the net-protons from [46, 16]. The final points are from table 6.1 and 6.9.

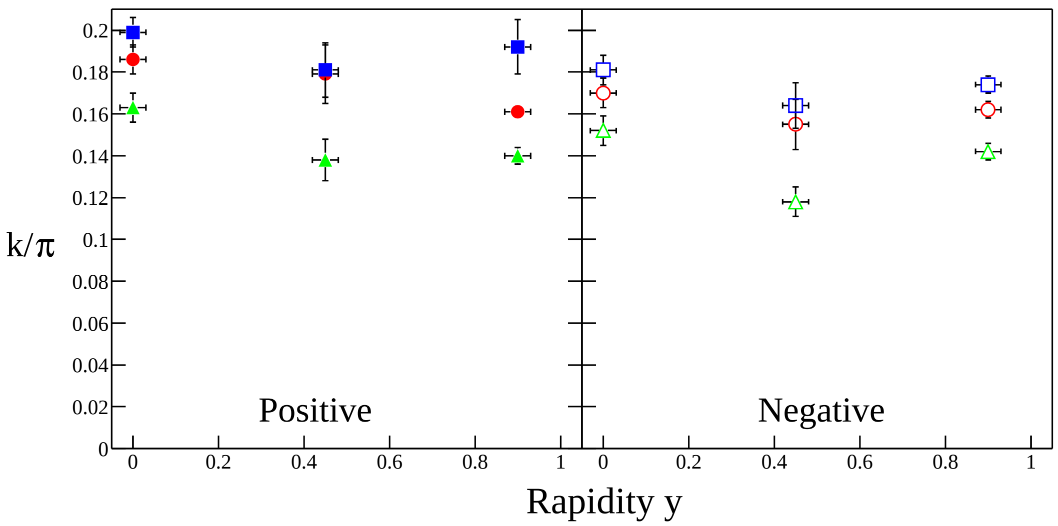

Figure 6.17: The kaon to pion ratios for the different models, exponential (red circles), Boltzmann (blue squares) and blast wave (green triangles).

k/π		$y = 0$	$y = 0.45$	$y = 0.9$
Pos	Exp	0.186 ± 0.007	0.179 ± 0.014	0.161 ± 0.003
	Boltz	0.199 ± 0.007	0.181 ± 0.013	0.192 ± 0.013
	BW	0.163 ± 0.007	0.138 ± 0.010	0.140 ± 0.004
Neg	Exp	0.170 ± 0.007	0.155 ± 0.012	0.162 ± 0.004
	Boltz	0.181 ± 0.007	0.164 ± 0.011	0.174 ± 0.004
	BW	0.152 ± 0.007	0.118 ± 0.007	0.142 ± 0.004

Table 6.10: The kaon to pion ratios for the different models.

to compare the negative ratios from SPS with the ratios found here. Furthermore, since the $\bar{p}/p$ ratio is so high the positive and negative kaon to pion ratios should be similar, which is also seen in figure 6.18. The points from $\sqrt{s_{NN}} = 130$ GeV contains systematic errors, while the points at $\sqrt{s_{NN}} = 200$ GeV only includes statistical errors.

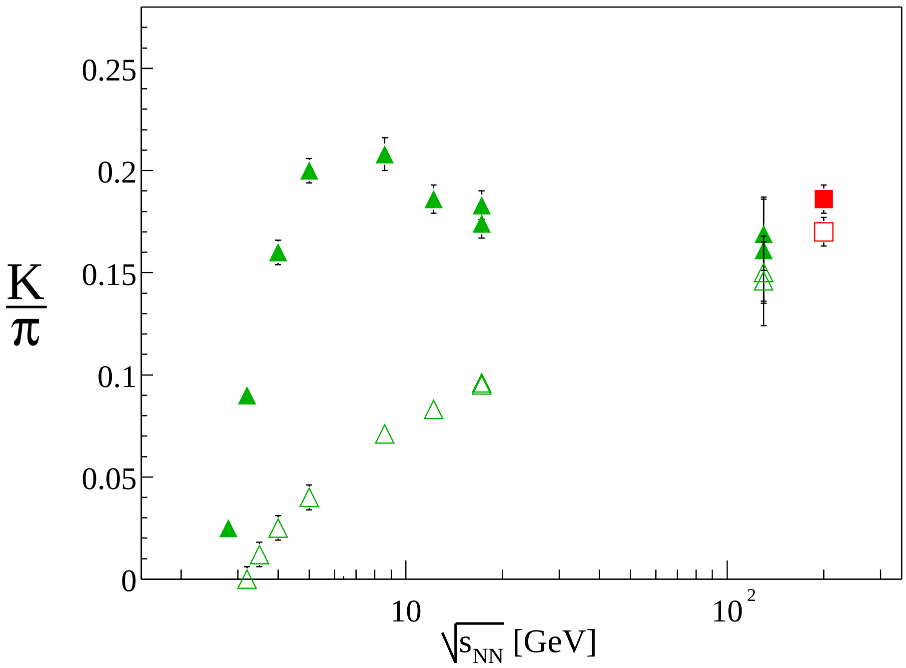

Figure 6.18: Kaon to pion ratio for different collision energies. For the negative ratios there is a constant increase with beam energy. The points from this thesis are marked as red squares. References to other experiments can be found in figure 2.11.

By applying a statistical thermal model to SPS data the chemical freeze out temperature $T_{fo} = 168 \pm 2.4$ MeV has been established [48]. Further more the freeze out temperature for $\sqrt{s_{NN}} = 130$ GeV and same model calculations is 174 ± 7 MeV [49]. This is consistent with an upper limit due to confinement. For $\sqrt{s_{NN}} = 200$ GeV it has been shown that freeze out temperatures around $170 \sim 180$ MeV fits data very well, figure 2.16. Furthermore strange chemical equilibrium has been reached at freeze out.

From [49] the negative kaon to pion ratio is 0.149 ± 0.02 at $\sqrt{s_{NN}} = 130$ GeV. In this analysis and the same fit method the ratio is 0.170 ± 0.007, statistical errors only. This means that the ratio has either increased or at least stays the same, when the collision energy is increased. Furthermore the time evolution in the collision is too short for strange chemical equilibrium to be reached by hadronic interactions [50]. It can only be reached in a QGP phase. Two gluons producing an $s\bar{s}$ only requires $2m_s \sim 300$ MeV, where as $\pi + \pi \to 2K$ requires ~ 1 GeV. Thus, the observation of strange chemical equilibrium together with a large strangeness enhancement would be a clear sign of a phase transition.

Chapter 7

Conclusion

During my period as a member of the BRAHMS collaboration, we have refined the methods to do particle identification and momentum measurements. This has resulted in the production of particle spectra. I have focused on the midrapidity region. I have tested the thermal Boltzmann and the hydrodynamical blast wave model against each other and against the exponential approximation, in the rapidity region $0 < y < 0.9$. All three fits give an estimation of the yields, and a temperature. Furthermore the different kinetic freeze out temperatures have been estimated.

When calculating the yields, all three fit models showed very little variation over one unit of rapidity in the extrapolated particle yields, consistent with the Bjorken picture. The yields differed as much as 30% between the different models, but show no significant changes with rapidity. The exception is for the exponential fits, at $y \approx 3$. At this rapidity, the yield estimations are clearly lower, indicating that the main particle production occurs around midrapidity. For particles with low mass the blast wave gave the highest yields and for heavier particles the exponential fit gave the highest yields. Due to the hydrodynamical approach of the blast wave model, the heavier particles are more affected by the collective flow and their spectra have a curvature resulting in a lower number of particles for low p_t. The Boltzmann model assumes chemical and thermal equilibrium. Therefore it does not take the low p_t pions coming from decays of heavier particles into account. It gives a poor fit to pions, but a good fit to the protons. When estimating the yields, the values for pions should be around the values given by the exponential and the blast wave fits. The protons are more likely to have a value near the Boltzmann fit. For the kaons the three fit procedures give values close to each other.

The slopes extracted for the different particle spectra have been used to calculate the freeze out temperatures and transverse flow (exponential and the Boltzmann fits). For all three fit procedures the slopes do not change within the rapidity range. This is again a clear sign of a Bjorken plateau. For the exponential fit slopes for $y \approx 3$ was also investigated. The flow velocity was clearly lower than for midrapidity and the plateau no longer obtained. In the common rapidity region the Boltzmann and the exponential fits had approximately the same flow $\beta_t \approx 0.4$.

The exponential freeze out temperature was clearly higher than the other two. Calculations by Becattini et. al. [23] fitted to BRAHMS data has given a chemical freeze out temperature of 170 MeV. The exponential fits give a thermal freeze out temperature of 200 MeV. This would mean that the inelastic scattering would stop after the elastic scattering, so particles with higher energy than the particle production threshold, would not create any new particles when colliding. The Boltzmann model gave a freeze out temperature around 160 MeV which is below the predicted chemical freeze out temperature.

An interesting feature is the blast wave values for flow and temperature. All models have strong anti-correlation between the two. Still, it gives much higher flow velocities and lower freeze out temperatures, than the other two, $T_{fo} \approx 115$ MeV and $\beta_t \approx 0.62$. Due to the flow in the blast wave model, the heavier particles are forced out from the low p_t region in the spectra. While the other two fits calculate flow and temperature directly from the slopes of the spectra. As a result the blast wave model gives lower values for the freeze out temperature and higher values for the flow.

The idea behind the Boltzmann model is a static thermal source. In the collision there are many sources, a short time interval and flow. The blast wave model assumes a purely hydrodynamical approach. The collision contains both hard processes, the primary nucleon collisions, and soft processes, particles re-scattering from each other. Therefore the correct approach to fit the spectra seems to be a combination of the two models.

The plateau behavior of flow and temperature from AGS to SPS is still present at RHIC energies. This is interesting, since there are more particles produced at RHIC energies than at lower energies. The constant temperature can be explained by freeze out conditions. The thermal freeze out temperature is dependent on the invariant cross section and density. For a big source particles in one region of the source does not depend on particles in another region in the source. So the source size does not change the freeze out conditions between SPS and RHIC. If there is a phase transition in the collision, calculations [47] suggest the main part of the transverse flow is built up in the QGP phase, before chemical and thermal freeze out. In experiment we measure hadrons after chemical and thermal freeze out. The flow values approach each other for the two collision systems, with or without phase transition. Therefore, not much can be deduced from the flow velocity.

From anti-proton to proton ratio it has been seen that pair production is the main contributor to particles in the midrapidity region. Most primary protons have left the collision zone and a high degree of transparency has been reached. Even if the transparency has increased, a clear increase in particle production is seen. So increasing the collision energy does not mean that the two projectiles "swim" through each other, without effects. Rather, particles are produced by a new mechanism, color string breaking.

One signal of QGP is the strangeness enhancement. A way to measure this signal is to calculate the kaon to pion ratio. For SPS energies there was a strong enhancement for ratios from positive particles, since there were a lot of primary protons left in the collision zone. At RHIC energies this is no longer the case, but still a high value for positive ratios is found. There is an increase in the negative ratios from SPS to RHIC energies, and the positive and negative ratios are equal. In this thesis it has been shown that the extracted kaon to pion ratio strongly depends on the model used. The ratios are highest for the thermal Boltzmann and lowest for the blast wave model. This will affect the chemical freeze out temperature, which is dependent on this ratio.

By comparing the kaon to pion ratio with the anti-proton to proton ratio for different experiments at SPS and RHIC a chemical freeze out temperature of ~ 170 MeV is found. in central collisions at RHIC energies also strange chemical equilibrium is reached [49]. The time interval of the collisions is too small for this equilibrium to be reached if not a phase transition has occurred [50]. The freeze out temperature is to low for strange equilibrium to be obtained through hadronic interactions. The pion-pion to kaon-kaon cross section is to small. So the low freeze out temperature together with strange chemical equilibrium provides evidence of pre-hadronic behavior, yet to be explored.

The conclusions of stopping and kaon to pion ratios are dependent on which model used to fit the data. For the spectra presented here, the blast wave model clearly best reproduces the data, and this model seems to be the most correct for analyzing the data. The exponential and the thermal Boltzmann model should be replaced by the more sophisticated blast wave model for future analysis.

Appendix A

Some definitions and variable transformations.

First some definitions.

$$p_x = p_t cos\phi \tag{A.1}$$

$$p_y = p_t sin\phi \tag{A.2}$$

$$p_z = m_t sinhy \tag{A.3}$$

$$m_t = \sqrt{{p_t}^2 + m^2} \tag{A.4}$$

$$E = m_t coshy \tag{A.5}$$

$$\eta = -\ln\tan(\theta/2) \tag{A.6}$$

From chapter 4 we get 4.2. The variable transformation is done by calculating the Jacobi determinant.

$$\frac{\delta(p_x, p_y, p_z)}{\delta(p_t, y, \phi)} = \begin{vmatrix} \frac{\delta p_x}{\delta p_t} & \frac{\delta p_x}{\delta y} & \frac{\delta p_x}{\delta \phi} \\ \frac{\delta p_y}{\delta p_t} & \frac{\delta p_y}{\delta y} & \frac{\delta p_x}{\delta \phi} \\ \frac{\delta p_z}{\delta p_t} & \frac{\delta p_z}{\delta y} & \frac{\delta p_x}{\delta \phi} \end{vmatrix} \tag{A.7}$$

p_z is independent of both p_t and ϕ. This means that A.7 can be simplified to

$$\frac{\delta(p_x, p_y, p_z)}{\delta(p_t, y, \phi)} = \frac{\delta p_z}{\delta p_y} \begin{vmatrix} \frac{\delta p_x}{\delta p_t} & \frac{\delta p_x}{\delta \phi} \\ \frac{\delta p_y}{\delta p_t} & \frac{\delta p_y}{\delta \phi} \end{vmatrix} \tag{A.8}$$

Derivation of the definitions gives

$$dp^3 = m_t coshy \begin{vmatrix} cos\phi & -p_t sin\phi \\ sin\phi & p_t cos\phi \end{vmatrix} dp_t dy d\phi = E(p_t cos^2\phi + p_t sin\phi) = E p_t dp_t dy d\phi \tag{A.9}$$

and by integrating over ϕ the invariant crossection becomes

$$E\frac{d^3n}{dp^3} = \frac{d^2n}{2\pi p_t dp_t dy} \tag{A.10}$$

From definition A.4 derivation $\frac{dm_t}{dp_t}$ gives

$$\frac{dm_t}{dp_t} = \frac{p_t}{\sqrt{{p_t}^2 + m^2}} = \frac{p_t}{m_t} \tag{A.11}$$

and thus

$$m_t dm_t = p_t dp_t. \tag{A.12}$$

Appendix B

Integral calculations

$$\frac{dn}{dy} = 2\pi N \int_0^\infty p_t e^{-p_t/T} dp_t \tag{B.1}$$

Integration by parts gives

$$\frac{dn}{dy} = 2\pi N \tag{B.2}$$

Boltzmann integration

From equation 4.30 we have

$$\begin{aligned}
\frac{dn}{dy} &= 2\pi N \int_m^\infty m_t^2 e^{-m_t/T} dm_t = 2\pi N \bigg(\Big[-Tm_t^2 e^{-m_t/T} \Big]_m^\infty + T \int_m^\infty 2m_t e^{-m_t/T} dm_t \bigg) \\
&= 2\pi N \bigg(Tm^2 e^{-m/T} - \Big[2T^2 m_t e^{-m_t/T} \Big]_m^\infty + 2T^2 \int_m^\infty e^{-m_t/T} dm_t \bigg) \\
&= 2\pi N \bigg(Tm^2 e^{-m/T} + 2T^2 m e^{-m/T} - \Big[2T^3 e^{-m_t/T} \Big]_m^\infty \bigg) \\
&= 2\pi N \bigg(Tm^2 e^{-m/T} + 2T^2 m e^{-m/T} + 2T^3 e^{-m/T} \bigg) \\
&= 2\pi N T e^{-m/T} \Big(m^2 + 2mT + 2T^2 \Big)
\end{aligned}$$

Bibliography

[1] J.P. Bondorf, J.J. Gaardhøje, H. Heiselberg, B. Lauritzen, I.N. Mishustin, and H. Schultz *Hot and Dense Matter*, Niels Bohr Institute, Copenhagen, 1996

[2] E. Laermann, *Recent Results from Lattice QCD Simulations* Nucl. Phys. **A610** (1996) 1c

[3] `http://www.physics.ohio-state.edu/~kilcup/Lattice_QCD/`

[4] I. G. Bearden *et al.* [BRAHMS Collaborations], *Charged particle densities from Au + Au collisions at s(NN)**(1/2) = 130-GeV* Phys. Lett. B **523** (2001) 227 [arXiv:nucl-ex/0108016].

[5] E. L. Feinberg, *Landau Hydrodynamical Model as a Basis for Treating Relativistic Heavy Ion Collisions* Lebedev Inst., 1991

[6] J. D. Bjorken, *Highly Relativistic Nucleus-Nucleus Collisions: The Central Rapidity Region,* Phys. Rev. D **27** (1983) 140.

[7] P. Christiansen [BRAHMS Collaboration], *Rapidity dependence of net-protons at S(NN)**(1/2) = 200-GeV* arXiv:nucl-ex/0212002.

[8] C. Michael, C. McNeile and D. Hepburn [UKQCD Collaboration], *The strangeness content of the nucleon* Nucl. Phys. Proc. Suppl. **106** (2002) 293 [arXiv:hep-lat/0109028].

[9] M. van Leeuwen [NA49 Collaboration], *Strangeness in high-energy nuclear collisions Prepared for International Europhysics Conference on High-Energy Physics (HEP 2001), Budapest, Hungary, 12-18 Jul 2001*

[10] L. Ahle *et al.* [E802 Collaboration], *Particle Production At High Baryon Density In Central Au + Au Reactions At 11.6-A-Gev/C* Phys. Rev. C **57** (1998) 466.

[11] L. Ahle *et al* [E802 Collboration], *Kaon production in Au+Au collisions at 11.6A GeV/c* Phys. Rev. C **58** (1998) 3523.

[12] L. Ahle *et al* [E866 Collaboration] *Excitation function of K^+ and π^+ production in Au+Au reactions at 2-10 AGeV* Phys. Lett. B **476** (2000) 1

[13] L. Ahle *et al.* [E866 Collaboration], *An excitation function of K- and K+ production in Au + Au reactions at the AGS* Phys. Lett. B **490** (2000) 53 [arXiv:nucl-ex/0008010].

[14] C. Blume *et al* [Na49 Collaboration] *New results from NA49* Nucl. Phys. A **698** (2002) 104c

[15] S. V. Afanasiev *et al.* [The NA49 Collaboration], *Energy dependence of pion and kaon production in central Pb + Pb collisions* Phys. Rev. C **66** (2002) 054902 [arXiv:nucl-ex/0205002].

[16] I. G. Bearden *et al.* [NA44 Collaboration], *Particle production in Pb + Pb collisions at the CERN-SPS* arXiv:nucl-ex/0202019.

[17] K. Adcox *et al.* [PHENIX Collaboration], *Centrality dependence of pi+-, K+-, p and anti-p production from s(NN)**(1/2) = 130-GeV Au + Au collisions at RHIC* Phys. Rev. Lett. **88** (2002) 242301 [arXiv:nucl-ex/0112006].

[18] C. Adler *et al.* [STAR Collaboration], *Kaon production and kaon to pion ratio in Au + Au collisions at s(NN)**(1/2) = 130-GeV* arXiv:nucl-ex/0206008.

[19] D. Ouerdane [BRAHMS Collaboration], *Rapidity dependence of charged particle yields for Au + Au at s(NN)**(1/2) = 200-GeV* arXiv:nucl-ex/0212001.

[20] M. C. Abreu *et al.* [NA50 Collaboration], *Recent Results On J / Psi From Experiment Na50* Nucl. Phys. A **698** (2002) 127.

[21] I. G. Bearden *et al.* [BRAHMS Collaboration], *Pseudorapidity distributions of charged particles from Au + Au collisions at the maximum* RHIC *energy* arXiv:nucl-ex/0112001.

[22] I. G. Bearden [BRAHMS Collaboration], *Rapidity dependence of charged antiparticle-to-particle ratios in Au + Au collisions at s(NN)**(1/2) = 200-GeV* arXiv:nucl-ex/0207006.

[23] F. Becattini *et al. Features of particle multiplicities and strangeness production in central heavy ion collisions between 1.7A and 158A GeV/c* Phys. Rev. C **64**, 024901 (2001)

[24] H. Boggild *et al.* [NA44 Collaboration], *Coulomb effect in single particle distributions* Phys. Lett. B **372** (1996) 339.

[25] E. Schnedermann, J. Sollfrank, U. Heinz *Thermal phenomenology of hadrons from 200A GeV S+S collisions* Phys. Rev. C **48** (1993) 5

[26] N. Xu *et al.* [NA44 Collaboration], *Hadron Distributions: Recent Results From The Cern Experiment Na44* Nucl. Phys. A **610** (1996) 175C.

[27] I. G. Bearden *et al.* [NA44 Collaboration], *Collective expansion in high energy heavy ion collisions* Phys. Rev. Lett. **78** (1997) 2080.

[28] N. Hermann, J. P. Wessels and T. Wienold *Collective Flow in Heavy-Ion Collisions*, Ann. Rev. Nucl. Part. Sci. **49** (1999) 581

[29] I. G. Bearden et al., *Antideuteron Production in 158A GeV/c Pb + Pb Collisions* Phys. Rev. Lett. **85** (2000) 2681

[30] Allan G. Hansen *Light Nuclei Production In Ultra Relativistic Heavy Ion Collisions* Ph.D. Thesis, Niels Bohr Institute (1999).

[31] M. Gyulassy, S. K. Kauffmann and L. W. Wilson, *Pion Interferometry Of Nuclear Collisions. I. Theory* Phys. Rev. C **20** (1979) 2267.

[32] U. Heinz & B. V. Jacak *Two-Particle Correlations in Relativistic Heavy-Ion Collisions* Ann. Rev. Nucl. Part. Sci **49** (1999) 245

[33] RHIC *Design Manual*, http://www.rhichome.bnl.gov/NT-share/rhicdm/index.html

[34] I. G. Bearden *et al.* [BRAHMS Collaboration], *The* BRAHMS *Experiment at* RHIC, accepted for publication in special Nucl. Inst. Meth. issue on RHIC.

[35] H. Appelshauser *et al.* [NA49 Collaboration], *Spectator Nucleons In Pb + Pb Collisions At 158-A-Gev* Eur. Phys. J. A **2** (1998) 383.

[36] S. Margetis *et al.* [NA49 Collaboration], *Transverse energy production in Pb-208 + Pb collisions at 158-GeV per nucleon* Phys. Rev. Lett. **75** (1995) 3814.

[37] William. R. Leo *Techniques for Nuclear and Particle Physics Experiments* Springer-Verlag, 1994

[38] Philip J. Siemens & John O. Rasmussen *Evidence for a Blast Wave from Compressed Nuclear Matter* Phys. Rev. Lett. **42** (1979) 880

[39] R. Hagedorn, *Multiplicities, P(T) Distributions And The Expected Hadron → Quark - Gluon Phase Transition* Riv. Nuovo Cim. **6N10** (1984) 1.

[40] M. I. Sobel, H. A. Bethe, P. J. Siemens and J. P. Bondorf, *Shock Waves In Colliding Nuclei* Nucl. Phys. A **251** (1975) 502.

[41] E. Schnedermann and U. W. Heinz, *Relativistic hydrodynamics in a global fashion* Phys. Rev. C **47** (1993) 1738.

[42] E. Schnedermann, J. Sollfrank and U. W. Heinz, *Thermal phenomenology of hadrons from 200-A/GeV S+S collisions* Phys. Rev. C **48** (1993) 2462 [arXiv:nucl-th/9307020].

[43] W. Reisdorf *et al.* [FOPI Collaboration], *Central collisions of Au on Au at 150-A-MeV, 250-A-MeV and 400-A-MeV* Nucl. Phys. A **612** (1997) 493 [arXiv:nucl-ex/9610009].

[44] B. Hong *et al.* [FOPI Collaboration], *Stopping and radial flow in central Ni-58 + Ni-58 collisions between 1-A-GeV and 2-A-GeV* Phys. Rev. C **57** (1998) 244 [Phys. Rev. C **58** (1998) 603] [arXiv:nucl-ex/9707001].

[45] M. A. Lisa *et al.* [EOS Collaboration], *Radial flow in Au + Au collisions at E = 0.25-A/GeV - 1.15-A/Gev* Phys. Rev. Lett. **75** (1995) 2662 [arXiv:nucl-ex/9502001].

[46] B. B. Back *et al.* [E917 Collaboration], *Results From Experiment E917 For Au + Au Collisions At The Ags* Nucl. Phys. A **661** (1999) 75.

[47] P. F. Kolb, J. Sollfrank and U. W. Heinz, *Anisotropic transverse flow and the quark-hadron phase transition* Phys. Rev. C **62** (2000) 054909 [arXiv:hep-ph/0006129].

[48] P. Braun-Munzinger, I. Heppe and J. Stachel, *Chemical equilibration in Pb + Pb collisions at the SPS* Phys. Lett. B **465** (1999) 15 [arXiv:nucl-th/9903010].

[49] P. Braun-Munzinger *et al Hadron production in Au-Au collisions at RHIC* Phys. Lett. B **518** (2000) 41

[50] P. Koch, B. Muller and J. Rafelski, *Strangeness In Relativistic Heavy Ion Collisions* Phys. Rept. **142** (1986) 167.